UC-414
LBL-25652
c1

Lawrence Berkeley Laboratory
UNIVERSITY OF CALIFORNIA

Physics Division

Inclusive Production of Vector Mesons in e^+e^- Annihilation at $\sqrt{s} = 29$ GeV

OCT 1988

T.K. Edberg
(Ph.D. Thesis)

August 1988

For Reference

Not to be taken from this room

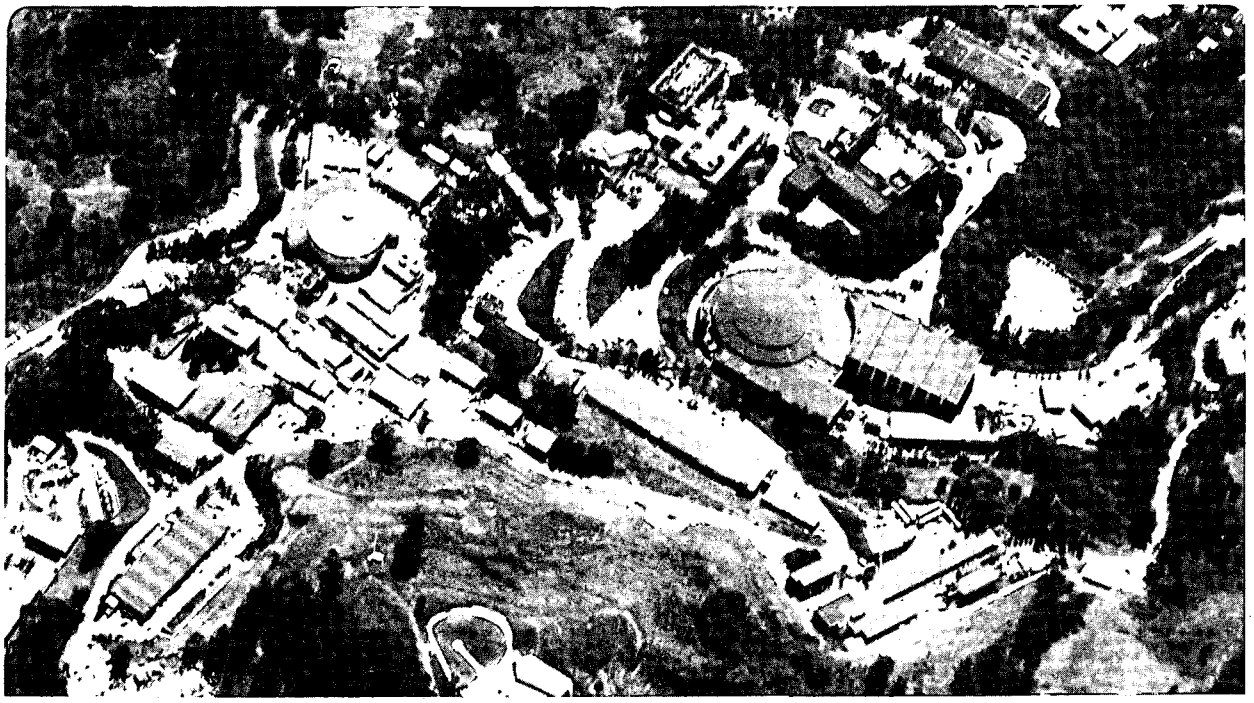

LBL-25652
c1

Prepared for the U.S. Department of Energy under Contract Number DE-AC03-76SF00098.

DISCLAIMER

This document was prepared as an account of work sponsored by the United States Government. While this document is believed to contain correct information, neither the United States Government nor any agency thereof, nor the Regents of the University of California, nor any of their employees, makes any warranty, express or implied, or assumes any legal responsibility for the accuracy, completeness, or usefulness of any information, apparatus, product, or process disclosed, or represents that its use would not infringe privately owned rights. Reference herein to any specific commercial product, process, or service by its trade name, trademark, manufacturer, or otherwise, does not necessarily constitute or imply its endorsement, recommendation, or favoring by the United States Government or any agency thereof, or the Regents of the University of California. The views and opinions of authors expressed herein do not necessarily state or reflect those of the United States Government or any agency thereof or the Regents of the University of California.

LBL-25652

Inclusive Production of Vector Mesons in e^+e^- Annihilation at $\sqrt{s} = 29$ GeV

Timothy Kent Edberg
Ph.D. Thesis

Department of Physics
University of California, Berkeley, CA 94720
and
Lawrence Berkeley Laboratory,
University of California, Berkeley, CA 94720

August 1, 1988

Abstract

This thesis describes the measurement of multiplicities and differential cross-sections of the ρ^0 , K^{*0}, and ϕ in e^+e^- annihilation at $\sqrt{s} = 29$ GeV, using data collected by the TPC/2γ Detector Facility at PEP. The number of vector mesons per event is determined to be $N(\rho^0) = 0.77 \pm 0.08 \pm 0.15$, $N(K^{*0} + \overline{K}^{*0}) = 0.58 \pm 0.05 \pm 0.11$, and $N(\phi) = 0.076 \pm 0.010 \pm 0.012$. These multiplicities are used to find that the ratio of strange quarks to up quarks produced in the hadronization process is 0.30 ± 0.07, and that the ratio of light vector mesons to all light mesons produced in the hadronization process is 0.45 ± 0.08. All results agree with previous measurements. Measurements are compared with predictions of the Lund and Webber hadronization models; neither model is particularly favored nor disfavored.

This work is supported by the United States Department of Energy under Contract DE-AC03-76SF00098

Contents

Acknowledgements iv

Dedication vi

1 Introduction 1

2 Theory of Hadron Production in e^+e^- Annihilation 10

2.1 Electroweak Production of $q\overline{q}$ 10

2.2 Hard QCD Processes 11

2.2.1 Fixed Order Perturbative QCD 12

2.2.2 Leading Logarithm Approximation 13

2.3 Hadronization Models 14

2.3.1 Independent Fragmentation 15

2.3.2 String Fragmentation 16

2.3.3 Cluster Fragmentation 22

2.3.4 UCLA Model 25

2.3.5 Experimental Status of Models 26

3 Experimental Apparatus 27

3.1 PEP 27

3.2 Detector Systems 27

3.2.1 TPC/2γ Detector Facility 27

3.2.2 TPC 34

3.2.2.1 Operation 34
3.2.2.2 Calibration 42
3.2.2.3 Resolutions 44
3.3 Trigger 47

4 Data Reduction, Event Selection, and Event Simulation 50
4.1 Data Reduction 50
4.1.1 Analysis Sequence 50
4.1.2 Particle Identification Using dE/dx 54
4.2 Event Selection 62
4.3 Detector Simulation 65

5 Measurement of the ρ^0 Differential Cross-section 68
5.1 Overview 68
5.2 Basic Method 71
5.2.1 Formation of the Mass Spectra 71
5.2.2 Extracting the Cross-section 76
5.3 Estimation of Systematic Errors 89
5.4 Results 99

6 Measurement of the ϕ Differential Cross-section 103
6.1 Overview 103
6.2 Basic Method 104
6.2.1 Formation of the Mass Spectra 104
6.2.2 Extracting the Cross-section 110
6.3 Estimation of Systematic Errors 112
6.4 Results 118

7 Measurement of the K^{*0} Differential Cross-section 122

7.1 Overview 122

7.2 Basic Method 123

7.2.1 Formation of the Mass Spectra 123

7.2.2 Extracting the Cross-section 126

7.3 Estimation of Systematic Errors 132

7.4 Results 138

8 Determination of s/u and V/(V+P) 142

8.1 Multiplicity Ratio Method 143

8.2 Lund-specific Method 157

9 Summary and Conclusions 161

Acknowledgements

The TPC/2γ Collaboration, which built the detectors and accumulated the data used in this work, is too large to thank each member individually. Without the unique contributions of each colleague, however, this thesis would be impossible, so I thank all my collaborators for making my research feasible.

Some people stand out as having an especially profound impact on this work and on my continuing education; I welcome this opportunity to publicly thank them. My advisor, Lynn Stevenson, has been my enthusiastic supporter from the very first day I visited the University of California as a prospective graduate student. Pier Oddone has also been solidly in my corner, helping me out behind the scenes more than once. I am grateful to Lynn and Pier for reviving my flagging spirits at crucial junctures. I thank my dissertation committee—Lynn, George Trilling, and John Rasmussen—for their prompt and constructive comments for improving this thesis.

Hiro Yamamoto patiently aided my analysis until I learned how to do it on my own. Werner Hofmann helped guide my work to completion. Gerry Lynch tolerantly endured my endless questioning. I owe whatever talent I have for analysis in large part to them. Garth Smith has been instrumental in teaching me hardware skills. I have also benefitted greatly, professionally and personally, from the counsel and friendship of my fellow graduate students: Rob, Glen, Dan, Kevin, Jack, Bill, Forest, Mike, Tad, Shahin, Rem, Zack, Cary, and Lisa.

Finally, I want to thank my friend and mentor, Peter Némethy, for his patient

and thorough instruction in the ways of experimental physics, and for his support and wise advice in matters within and without the world of physics.

Dedication

I dedicate this thesis to my parents, Robert and Patricia.

Chapter 1

Introduction

It is the goal of physics to understand the material universe we live in. The goal of High Energy Physics is to understand the fundamental constituents of matter and the interactions between them. The current best understanding of these fundamental constituents and forces is in terms of gauge theories describing the interactions of pointlike particles.

The most successful of these theories is Quantum Electrodynamics (QED), which can, for example, predict the magnetic moment of the electron to nine significant figures. QED has been combined with the gauge theory of weak interactions into an "electroweak" theory, also called the Standard Model of Glashow, Weinberg, and Salam. While this model cannot compete with QED for extreme numerical precision of its predictions, it has had some dazzling successes (such as the prediction of the existence and masses of the $W^{\pm}$ and Z^0 bosons), and is consistent with all current experimental results. This theory's main drawbacks are the abundance of unconstrained parameters that must be fixed by experiment, and the crucial and experimentally unverified assumption of the existence of the Higgs particle(s).

The current theory of strong interactions, Quantum Chromodynamics (QCD), is another successful gauge theory. The physical reality of the quarks, gluons, and three color charges that it postulates have been amply verified in diverse phe-

nomena. The existence of quarks, for example, is seen in hadron spectroscopy, (approximate) Bjorken scaling in deep inelastic lepton-nucleon scattering, and in the existence of jets in e^+e^- annihilation. The three color charges are necessary to explain, among other things, the rate of e^+e^- annihilation into hadrons, the π^0 lifetime, and the existence of the Δ^{++} and Ω^-. The role of gluons as the quanta of QCD is demonstrated in the existence of three-jet events in e^+e^- annihilation, in large p_T jets in hadron-hadron collisions, and in the observations from deep inelastic lepton-nucleon scattering of scaling violations, broad p_T distributions, and the presence of electrically neutral hadronic constituents.

QCD suffers, however, from the relatively large value of its coupling constant, α_s. This means that perturbation theory calculations are less accurate to a given order than electroweak calculations. What is worse, α_s is a fairly strong function of Q^2, the four-momentum transfer of the interaction. This running coupling constant is given by

$$\alpha_s(Q^2) = \frac{12\pi}{(33 - 2n_f)\ln\left(Q^2/\Lambda^2_{QCD}\right)} \tag{1.1}$$

where n_f is the number of quark flavors (presumably six) and where $\Lambda_{QCD} \sim$0.1–0.5 GeV is a parameter to be determined by experiment. This means that for quark-gluon interactions on the scale of 30 GeV, say, $\alpha_s \sim$ 0.15–0.2 and perturbation expansions are useful; but that for interactions on the scale of the 1 GeV typical of hadronic masses, $\alpha_s \gtrsim 1$ and perturbation expansions are useless. In a way, this is good news, for it explains the phenomena of confinement and asymptotic freedom: confinement refers to the fact that isolated quarks are never observed directly in the lab, but rather are always confined within hadrons; asymptotic freedom refers to the fact that quarks inside hadrons behave as if they were non-interacting when probed by large Q^2 processes. The running coupling constant enforces confinement by making the long-range — hence low Q^2 — restoring force on a quark heading out of a hadron so strong that it either re-

mains bound or it becomes energetically favorable for $q\bar{q}$ pairs to materialize from the strong field energy to "dress" the escaping quark; either way, a quark can never depart the company of other quarks bound to it in a hadron. The running coupling constant allows asymptotic freedom because high Q^2, short-range probes interact with quarks inside hadrons in a Q^2 regime where they are largely decoupled from one another due to the small magnitude of α_s.

While the nature of the running coupling constant helps explain the prominent QCD phenomena of confinement and asymptotic freedom, it makes it impossible to understand the detailed nature of confinement forces from a perturbative QCD approach. Moreover, it makes uncalculable the transition from the initial $q\bar{q}$ state created in e^+e^- annihilation to the final observed hadrons, a transition which of necessity involves low Q^2 gluons and quarks on the road to hadrons whose masses are $O(1\text{ GeV})$. The lack of an analytic theory to predict this transition to final state hadrons, a process called "hadronization" or "fragmentation," necessitates recourse to empirical models to describe the transition. These models typically are motivated by some underlying physical principle, but resort to modeling the uncalculable processes in terms of Monte Carlo computer programs which use random number generators to simulate the stochastic processes involved.

An e^+e^- annihilation into hadrons separates into four basic stages, illustrated in Figure 1.1. First is the electroweak creation of a $q\bar{q}$ pair from the virtual γ or Z^0 arising from the e^+e^- annihilation. The second stage of the event consists of the hard QCD processes accessible to analytic calculation. The third stage consists of the soft QCD hadronization process. Finally, in the fourth stage, hadrons produced in the third stage that are unstable decay into the particles ultimately detected experimentally. As depicted in Figure 1.1, the initial q and $\bar{q}$ evolve into the final state hadrons through QCD gluon emission and $q\bar{q}$ pair creation in a

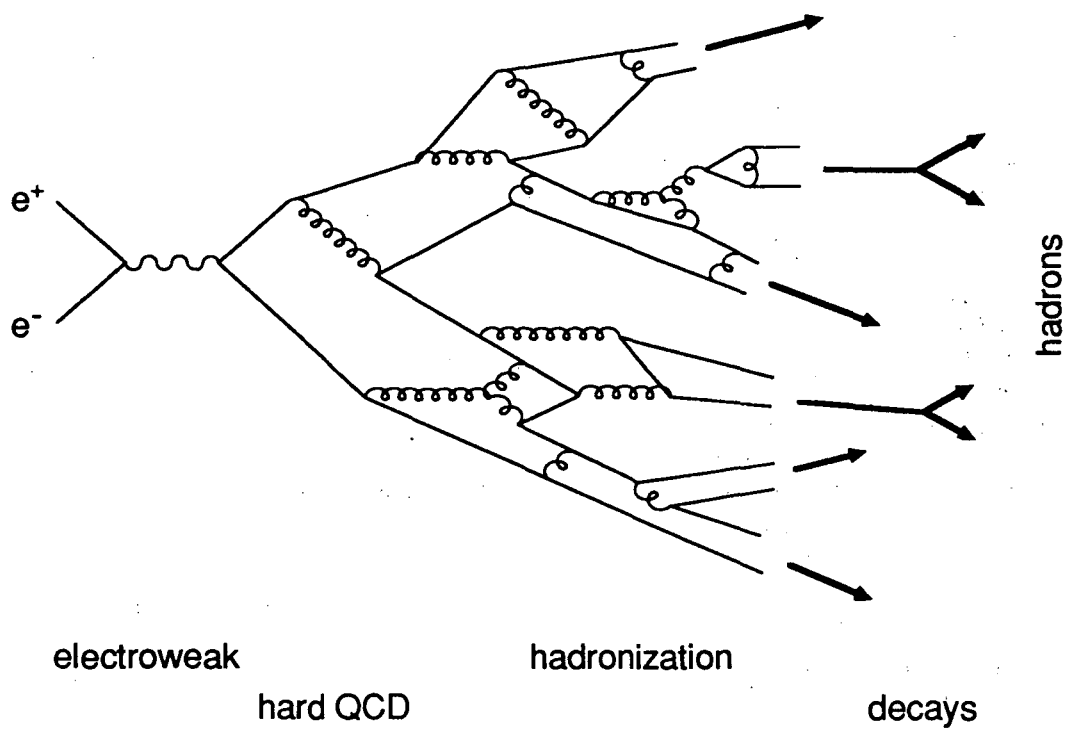

Figure 1.1: Schematic evolution of an e^+e^- annihilation into hadrons. The arrows represent the detected particles.

continuous fashion; the boundaries between the second, third, and fourth stages are arbitrary and set by limitations of the calculational tools brought to bear in each case. Roughly speaking, the hard QCD phase gives way to hadronization when Q^2 is on the order of a few GeV^2 (i.e. when α_s approaches 1), and resonance decays take over when $Q^2 \lesssim 1\ \mathrm{GeV}^2$.

The least understood of these four stages is the hadronization process. Several different models have been proposed to describe hadronization; I discuss some of these in the next chapter. It is the goal of experimentalists studying hadronization to bring as many experimental tests of the various models to bear as possible. This serves to fine-tune the models for better agreement with experiment, to identify strengths and weaknesses of the models, and to provide

input for future model-builders to revise current models or to construct new ones. Achieving agreement between models and data is worthwhile at the least because the event structure produced by fragmentation can be a background for other measurements of interest, and because fragmentation is the filter through which the hard QCD processes must be studied. But more importantly, the hope is that by ferreting out the strengths and weaknesses of various models, insight will be gained into the actual physics of hadronization itself. The analogy has been made that by describing the hadronization process ever more accurately and completely, the door could be opened to a true physical theory, much as Kepler's precise kinematical description of elliptical planetary orbits enabled Newton's dynamical theory of gravitation.

In this dissertation, I add new experimental measurements to the body of knowledge describing hadronization. Using data from e^+e^- annihilation into hadrons at $\sqrt{s} = 29$ GeV, collected by the TPC/2γ Detector Facility at PEP, I measure the differential cross-sections $\frac{1}{\beta\sigma_H}\frac{d\sigma}{dx}$ for three vector mesons: the ρ^0, the K^{*0}, and the ϕ. These cross-sections are functions of $x = E_{meson}/E_{beam} = 2E_{meson}/\sqrt{s}$; they are normalized to the total hadronic cross-section σ_H. (The β in the denominator compensates for phase-space suppression at low x which would otherwise mask the expected scaling behavior.) In addition, I integrate the differential cross-sections to establish measured multiplicities for the three vector mesons. These multiplicities are in practice often more useful than the detailed shape information of the differential cross-sections for the purpose of evaluating the performance of a model.

One of the characteristic features of fragmentation is that hadrons are not produced in simple proportion to the number of available spin states. Since u, d, and s quarks are so much lighter than the 29 GeV of available energy at PEP, one might naïvely predict from SU(6) (flavor) x (spin) symmetry that equal fragmen-

tation production rates should hold for particles that differ only by the substitution of an s for a u or d quark, and that vector mesons should be produced three times as often as their pseudoscalar partners. What is observed, however, is that strange particles appear in hadronization about a third as often as particles that differ by the substitution of a u or d quark for an s quark; and that light vector mesons (those not containing a c or b quark) appear in hadronization with rates comparable to their pseudoscalar partners. (The production rates from fragmentation are not the same as the rates observed, for decays of higher mass states contribute to the observed rates. Such decay, or "feed-down," contributions must be subtracted from observed rates before comparison of fragmentation rates can be made.)

The observed suppression of strange and vector states must be reproduced in any successful model of hadronization. In this thesis, I use my measured vector meson multiplicities to quantify the strange suppression in terms of the "s/u" ratio (the relative production rates of mesons differing by the substitution of an s for a u or d quark), and to quantify the light vector meson suppression in terms of the "V/(V+P)" ratio (the fraction of light mesons of a given quark content that are vectors instead of pseudoscalars).

The ρ^0, K^{*0}, and ϕ are useful particles to consider for a number of reasons. Vector mesons as a class are produced at rates exceeded only by pseudoscalar mesons, so these three particles appear at reasonable rates. Of all SU(3) vector mesons, only these three decay copiously to two charged particles, enabling efficient reconstruction of the parent using the particle identification ability of the TPC central tracking chamber. Vector mesons are a better probe of hadronization than are pseudoscalars, for they are less diluted by feed-down decays and hence provide a more direct window on fragmentation. (Another way of saying this is that the systematic error from feed-down subtraction is smaller for vector

than for pseudoscalar mesons. For example, the Lund Monte Carlo predicts that almost 90% of observed $\pi^{\pm}$ stem from decays of more massive states, whereas less than 20% of $\rho^{\pm}$ originate in particle decay.) Comparisons of ρ^0 and K^{*0} rates with π^0 and K^0 rates yield two measurements of V/(V+P); and the ρ^0, K^{*0}, and ϕ contain zero, one, and two strange quarks, respectively, allowing for a redundant measure of the s/u ratio.

Measuring the continuous function $\frac{1}{\beta\sigma_H}\frac{d\sigma}{dx}$ for a given meson amounts to making independent measurements of the meson production in each of several discrete x bins. One forms invariant mass spectra of meson decay product candidates from the data for each x bin; determining the area under the resonance peak establishes the number of mesons observed in the data. Normalization to the total hadronic cross-section is accomplished simply by dividing by the number of events represented in the mass plot. An acceptance correction is applied to account for inefficiencies in detecting the meson; this correction is determined by performing the identical analysis on Monte Carlo simulated events passed through a detector simulation.

A complication arises from the fact that the incoming e^+ or e^- can emit a photon before annihilating. The effect of this initial state radiation is to lower the $\sqrt{s}$ available in the annihilation, which raises the hadronic cross-section. If unaccounted for, this would increase the reported $\frac{1}{\beta\sigma_H}\frac{d\sigma}{dx}$. So that cross-sections and multiplicities can be compared unambiguously to models and other experiments, a correction to account for initial state radiation must always be made before reporting results; corrected results correspond to an unambiguous $\sqrt{s}$, easily compared to calculations or *Gedanken* experiments performed with no initial state radiation.

In practice, then, measuring $\frac{1}{\beta\sigma_H}\frac{d\sigma}{dx}$ boils down to this approximation:

$$\frac{1}{\beta\sigma_H}\frac{d\sigma}{dx} = \frac{1}{\beta}\,\frac{1}{\Delta x}\,\frac{N_D}{N_{MC}}\,N_{gen} \tag{1.2}$$

where

$x = E_{meson}/E_{beam} = 2E_{meson}/\sqrt{s}$,

β is some suitably defined average meson speed over the x-bin,

Δx is the width of the bin,

N_D is the number of particles observed in the given x bin per accepted event in the data sample,

N_{MC} is the number of particles observed in the given x bin per accepted event in the Monte Carlo sample (generated with initial state radiation, processed through a detector simulation, and analyzed in the same manner as the data), and

N_{gen} is the number of particles generated in the given x bin per event in the Monte Carlo physics generator when run with no initial state radiation.

To understand Equation 1.2, one may view it as $\left(\frac{1}{\beta}\frac{1}{\Delta x}\right)\frac{N_D}{A}$ where $A = N_{MC}/N_{gen}$ is the acceptance term that simultaneously corrects the observed rate N_D for detector acceptance and initial state radiation. Alternatively, one can think of Equation 1.2 as $\left(\frac{1}{\beta}\frac{1}{\Delta x}\right) rN_{gen}$, where $r = N_D/N_{MC}$ is the ratio of mesons detected in the data (per event) to those in the detector-simulated Monte Carlo (per event); this amounts to scaling the Monte Carlo generator cross-section by how much the data exceeds or falls short of the corresponding Monte Carlo measurement.

In this chapter I have outlined the reasons for interest in understanding hadronization, and the measurements I make to probe it. In Chapter 2 I explain in more detail the physics of e^+e^- annihilation and models used to describe hadronization. I describe the TPC/2γ Detector Facility in Chapter 3, and the manner in which raw data is processed in Chapter 4. Chapters 5, 6, and 7 present

my analyses for the ρ^0, ϕ, and K^{*0}, respectively; I determine s/u and V/(V+P) ratios in Chapter 8. I summarize my results and conclusions in Chapter 9.

Chapter 2

Theory of Hadron Production in e^+e^- Annihilation

2.1 Electroweak Production of $q\bar{q}$

The annihilation of e^+e^- into hadrons begins with the electroweak production of a $q\bar{q}$ pair through a virtual γ or Z^0. The QED production of a spin-$\frac{1}{2}$ fermion pair $f\bar{f}$ through a virtual γ has the cross-section in the center-of-mass frame

$$\frac{d\sigma}{d\Omega}(e^+e^- \to f\bar{f}) = e_f^2 \cdot \frac{\alpha^2}{4s}(1 + \cos^2\theta),$$

where s is the square of the center-of-mass energy, α is the fine-structure constant, θ is the angle between the f and the e^-, and e_f is the charge of f in units of the electron charge. This expression is valid in the extreme relativistic limit. Integrating over angles gives

$$\sigma(e^+e^- \to f\bar{f}) = \frac{4\pi\alpha^2}{3s} \cdot e_f^2.$$

This works out to $105e_f^2$ pb (neglecting radiative corrections) for the $\sqrt{s} = 29$ GeV available at PEP. Including the Z^0 channel in a full electroweak treatment makes only a small correction to this cross-section.

The total cross-section for production of all possible $q\bar{q}$ pairs is thus

$$\begin{aligned} \sigma(e^+e^- \to all\ q\bar{q}) &= \left(\frac{4\pi\alpha^2}{3s}\right) \cdot 3\sum_q e_q^2 \\ &= \sigma(e^+e^- \to \mu^+\mu^-) \cdot 3\sum_q e_q^2 \end{aligned} \tag{2.1}$$

where e_q is the charge of quark q (in units of the electron charge), the factor of three is from the three color states available for each quark flavor, and the sum runs over all quarks light enough to be produced. This is not quite the same as the total cross-section for production of hadrons, since the quarks can radiate gluons, thus providing more channels to hadronic final states. Adding a first order QCD correction to account for this yields the total $O(\alpha_s)$ hadronic cross-section $\sigma_H = \sigma(e^+e^- \to hadrons)$:

$$\sigma_H = \sigma(e^+e^- \to \mu^+\mu^-) \cdot 3 \sum_q e_q^2 \left(1 + \frac{\alpha_s}{\pi}\right). \tag{2.2}$$

This hadronic cross-section is often expressed through the ratio R, defined by

$$R = \frac{\sigma(e^+e^- \to hadrons)}{\sigma(e^+e^- \to \mu^+\mu^-)}.$$

2.2 Hard QCD Processes

The $q\bar{q}$ pair created in the electroweak e^+e^- annihilation will evolve to the observed hadrons through a complicated cascade of gluon emission and quark pair creation such as that pictured in Figure 1.1. Some of this process — the hard QCD stage — is calculable in analytic approximation schemes. There are two such schemes currently available: fixed order perturbative QCD (sometimes called the matrix element (ME) scheme), and the leading logarithm approximation (LLA). The ME method consists of performing a perturbative expansion in powers of α_s, keeping all Feynman diagrams up to a given order and neglecting everything beyond. The LLA method uses the renormalization group technique to sum the most divergent term from every order of α_s, neglecting all less severely divergent terms. (Each leading term is logarithmically divergent, hence the name.)

Since every gluon vertex contributes one power of α_s to the cross-section, an nth order ME calculation can only provide cross-sections for states contain-

ing no more than n partons beyond the original $q\overline{q}$ pair. By contrast, the LLA method can in principle be used to compute cross-sections for states containing any number of gluons. Both the ME and LLA methods are often lumped under the appellation "perturbative QCD" to indicate that they are QCD approximation methods analytically calculable by virtue of the small value of α_s at high Q^2.

2.2.1 Fixed Order Perturbative QCD

Single gluon emission from the original q or $\overline{q}$, pictured in Figure 2.1, contributes to the $O(\alpha_s)$ QCD cross-section. The single gluon emission cross-section can be expressed as

$$\frac{d^2\sigma}{dx_1 dx_2} = \sigma(e^+e^- \rightarrow all\ q\overline{q}) \cdot \frac{2\alpha_s}{3\pi} \frac{x_1^2 + x_2^2}{(1-x_1)(1-x_2)} \tag{2.3}$$

where $x_1 = 2E_q/\sqrt{s}$, $x_2 = 2E_{\overline{q}}/\sqrt{s}$, and $\sigma(e^+e^- \rightarrow all\ q\overline{q})$ is the zeroth order cross-section from Equation 2.1. The gluon emission cross-section diverges if $x_1 \rightarrow 1$ or $x_2 \rightarrow 1$, which corresponds to the gluon being either collinear with the q or $\overline{q}$ or being arbitrarily soft. This divergence is not necessarily a problem with the theory, for naked quarks accompanied by sufficiently soft or collinear gluons will be indistinguishable from the dressed quarks that result from fragmentation. The divergences in the integrated gluon emission cross-section are cancelled by divergences in the $O(\alpha_s)$ vertex and propagator corrections to the zeroth order cross-section, so that the total $O(\alpha_s)$ cross-section is finite. (It is this resulting total $O(\alpha_s)$ cross-section that appears in Equation 2.2.) In Monte Carlo programming, the divergence in Equation 2.3 is handled by imposing arbitrary cutoffs to x_1 and x_2.

QCD cross-sections to $O(\alpha_s^2)$ have been computed, although the results depend somewhat on the regularization scheme used to cancel divergences. The $O(\alpha_s^2)$ terms represent the addition of two partons to the original $q\overline{q}$ state. Terms

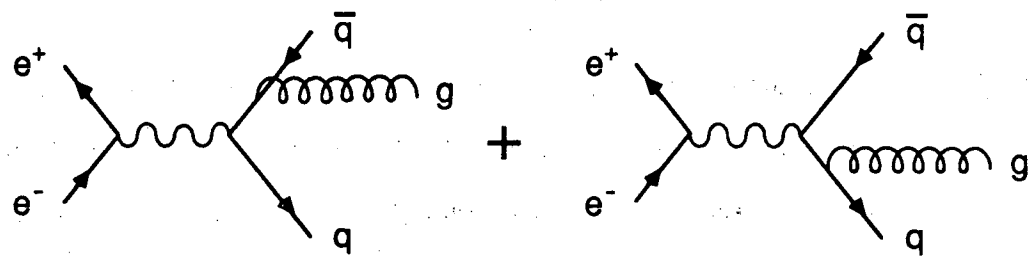

Figure 2.1: Feynman diagrams for single gluon emission from the $q\bar{q}$ state produced in e^+e^- annihilation.

of $O(\alpha_s^3)$ are difficult to calculate and are not used in ME Monte Carlos.

2.2.2 Leading Logarithm Approximation

The most divergent part of Equation 2.3 and higher order terms comes from the emission of gluons nearly collinear with their parent parton. The LLA approach sums these divergent contributions into a finite cross-section, thus describing processes involving any number of gluons. The radiated gluons can themselves emit gluons or split into $q\bar{q}$ pairs; the resulting "parton shower" of gluons and quarks splitting into more gluons and quarks can be computed in the LLA scheme. A typical parton shower is depicted in Figure 2.4a.

The evolution of the shower is governed by the differential probability $dP_{a\to bc}$ for a given parton a to split into two partons b and c, given by

$$dP_{a\to bc} = \frac{\alpha_s(Q^2)}{2\pi}\frac{d(m_a^2)}{m_a^2}\mathcal{P}_{a\to bc}(z)dz \tag{2.4}$$

where m_a is the mass of parton a, z is the fraction of parton a's momentum given to parton b, and $\mathcal{P}_{a\to bc}(z)$ is the Altarelli-Parisi splitting kernel [1,2]. These splitting kernels depend on the type of vertex:

$$\mathcal{P}_{a\to bc} = \quad \tfrac{4}{3}\tfrac{1+z^2}{1-z} \qquad \text{for } q \to qg,$$

$$\mathcal{P}_{a\to bc} = \frac{6(1-z(1-z))^2}{z(1-z)} \quad \text{for g} \to \text{gg},$$
$$\mathcal{P}_{a\to bc} = \tfrac{1}{2}(z^2 + (1-z)^2) \quad \text{for g} \to \text{q}\overline{\text{q}}.$$

Soft gluon terms are included in Equation 2.4 in an incoherent manner, i.e. neglecting their interference. The effect of soft gluon interference has been shown to restrict the phase space regime allowed for the shower [3]. This forbidden phase space can be avoided if successive splittings are ordered in decreasing magnitude of a variable ξ defined by

$$\xi = \frac{q_b \cdot q_c}{E_b E_c}.$$

where q_b and q_c are the four-momenta of partons b and c. For small values of q_b^2 and q_c^2, $\xi \sim (1 - \cos\theta)$ where θ is the angle between the produced partons, hence the name "angular ordering" applied to this prescription.

In Monte Carlo implementation, partons are emitted in the shower under the control of Equation 2.4, subject to the angular ordering restriction. The emitted partons become less and less virtual as the shower progresses until some minimum cutoff is reached, at which point showering is terminated.

2.3 Hadronization Models

The analytical tools of the last section can only go so far in describing the transition from initial $\text{q}\overline{\text{q}}$ to observed hadrons; they fail once α_s approaches unity. Hadronization models take over where the analytical methods leave off. They offer computer programmed prescriptions for stochastically evolving partonic configurations (generated by Monte Carlos that used analytical methods) through to final state hadrons. These prescriptions are motivated by some guiding physical principles; the successes or failures of a given model should give some insight into the role of the corresponding physical principle in fragmentation. In this section I discuss four models: independent fragmentation, string fragmentation, cluster

fragmentation, and the UCLA model.

2.3.1 Independent Fragmentation

The independent fragmentation (IF) model was first proposed by Field and Feynman [4] as a way to conveniently describe hadronic jets. In the Field-Feynman formulation, each initial quark evolves into hadrons independently. The evolution is an iterative process: q and $\overline{q}$ "sea quarks" materialize from the vacuum, one of which binds with the quark left over from the previous iteration to form a meson, the other sea quark being left over for the next iteration. The flavor of the sea quark pair is selected randomly in the ratio 2:2:1 for u:d:s to account for strange quark suppression. The transverse momenta (with respect to the jet) of the sea quarks sum to zero; their relative transverse momentum is chosen from a gaussian distribution. The longitudinal momentum of the newly created meson is determined by a probability function $f(z)$, which represents the probability that the meson carries off a fraction z of the remaining momentum of the jet. The inclusive momentum spectrum $D(z)$ of (primary) hadrons is then determined by $f(z)$ through

$$D(z) = f(z) + \int_z^1 \frac{d\eta}{\eta} f(1-\eta) D(z/\eta),$$

where the first term comes from the first meson produced and the second term accounts for mesons produced at later iterations. The spin of the new meson is chosen to be one or zero with equal probability to account for the observed V/(V+P) ratio. The iteration halts once the remaining energy in the jet is below some threshold.

The IF approach has flaws as a model of hadronization: energy and momentum conservation are not implicit in the model and must be imposed in an *ad hoc* fashion, flavor is not conserved and there are always leftover quarks to be disposed of somehow, the model is not manifestly Lorentz covariant, and no

correlations exist between opposing jets. Despite these flaws, it does well in reproducing broad characteristics of fragmentation phenomenology, which is all Field and Feynman ever intended it to do.

Extensions to the model were made by Hoyer [5] to add gluon jets; by Ali [6] to add b and c quark decay as well as a more elaborate treatment of gluons; and by Meyer [7] to add a mechanism for baryon production.

2.3.2 String Fragmentation

The central concept of string fragmentation (SF) is that of a color singlet QCD flux tube, or string, connecting partons. The strong interaction lines of force from colored partons are assumed to collapse into an essentially one-dimensional tube due to the mutual interactions of the gluon flux quanta inherent in the non-Abelian nature of the QCD Lagrangian; strong interactions between partons occur only through the force applied by the string. Such a string connecting the original $q\bar{q}$ of an e^+e^- annihilation is depicted in Figure 2.2a. This one-dimensional flux tube is assumed to carry a constant linear energy density of about 1 GeV/fm. It is treated as a classical, massless, relativistic, one-dimensional string with no transverse excitations.

Fragmentation of the initial quark-string-antiquark system is understood as follows. As the original $q\bar{q}$ pair separates in the center-of-mass frame, energy is deposited into the elongation of the string. It becomes energetically favorable for a $q\bar{q}$ pair to materialize from the vacuum in such a manner as to screen the color charge flux in between them, thereby reducing the potential energy contained in the field. That is, the string severs into two pieces, each of which now ends on one of the new quarks as illustrated in Figure 2.2b. Each piece of string can sever again by the same argument. This process continues until the individual quark-string-antiquark segments are no longer energetically favored to

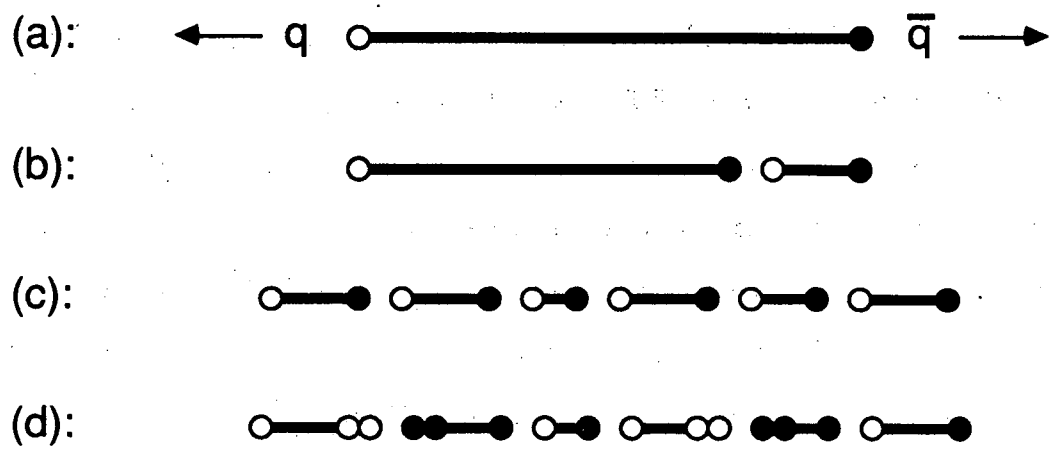

Figure 2.2: String fragmentation into hadrons. (a) The string connecting the original $q\bar{q}$ pair. (b) A break in the string by creation of a $q\bar{q}$ pair from the vacuum. (c) The string hadronized into mesons. (d) The string hadronized into mesons and baryons.

break: this occurs when confinement forces take over to make the quark-string-antiquark segments bound states — mesons — that would absorb rather than release energy upon cleaving. Put another way, the fragmentation process stops when the energy debt in creating new mesons exceeds the profit of removing energy from the field. The end result of the string fragmentation is a collection of quark-string-antiquark objects which are mesons, as pictured in Figure 2.2c.

The picture so far does not accommodate baryon production. Baryons can be incorporated by assuming that diquark-antidiquark pairs instead of quark-antiquark pairs are occasionally produced from the vacuum. These diquarks are not taken to be new fundamental particles, but simply to be two ordinary $q\bar{q}$ creations sufficiently close in phase space that the color field effectively acts on the qq and the $\bar{q}\bar{q}$ as units. Inclusion of this mechanism of baryon production results in the picture of string fragmentation shown in Figure 2.2d.

There are several heuristic arguments for exploring the string concept as a ba-

sis for hadronization. The 1+1 dimensional QED model of Schwinger [8] predicts stringlike fragmentation characteristics. QCD lattice gauge theory calculations predict linear QCD binding potentials [9]. Charm spectroscopy can be understood in terms of linear binding potentials [10]. Regge trajectories (which show hadron masses m_h appearing on loci given by $m_h^2 \propto J + constant$) can be interpreted by considering rotational modes of a relativistic string [11]. Whatever the motivations for the approach, however, its success must be judged in comparisons with data, which I discuss briefly in Section 2.3.5.

The most successful implementation of the SF approach is made by the Lund model [12,13,14]. To implement the string fragmentation picture, the Lund Monte Carlo uses an iterative procedure: the remaining string from the previous stage is fragmented into a hadron plus a leftover piece of string that then serves as input for the following stage. The hadron carries off one of the quarks that terminated the string at the start of the current iteration plus one of the vacuum (di)quarks; the other vacuum (di)quark terminates the leftover string.

The formation of a hadron in the model occurs through several steps, first at the quark level, then at the hadron level. The first steps are to select the flavor and p_T (with respect to the string direction) of the quark pair or diquark pair materializing from the vacuum. (Diquarks appear in the process at a rate governed by the Lund qq/q parameter. Since the steps are substantially the same if quarks materialize instead of diquarks, for ease of explanation I will discuss the chain of events only for quark production from the vacuum.) Combined with the known flavor and p_T of the quark terminating the string that will also enter the hadron, this specifies the total flavor content and p_T of the hadron.

Field theoretically, the vacuum $q\bar{q}$ must be produced at a point. This violates energy conservation, however, for energy is put into quark masses and p_T but not removed from the string. The Lund model assumes the materialization of $q\bar{q}$

pairs can be described by creation at a point followed by quantum mechanical tunneling to the classically allowed locations, where the energy in the eliminated portion of string balances the mass and p_T of the new $q\bar{q}$. A WKB calculation using constituent quark masses predicts that the probability of $u\bar{u} : d\bar{d} : s\bar{s} : c\bar{c}$ tunneling to the allowed region is roughly in the ratio $1 : 1 : 0.3 : 10^{-11}$. This mechanism accounts for strange quark suppression, and dictates that c and b quarks are not produced at all in hadronization. Moreover, the WKB calculation predicts a gaussian spread in p_T that is decoupled from the flavor assignment, a natural way to explain the observed gaussian spread of p_T in jets. While predicting the general quantitative behavior of strange quark suppression and p_T distribution, the Lund model does not use the WKB calculation to constrain these quantities; rather, it leaves them as free parameters of the model, to be adjusted for best agreement with data. Thus, the flavor of the $q\bar{q}$ pair is chosen randomly in the ratio $1 : 1 : (s/u)$ for $u\bar{u} : d\bar{d} : s\bar{s}$, and the p_T is chosen independently from a gaussian of width σ_q (and randomized in azimuth). Since the string has no transverse excitations, the p_T of vacuum quark and antiquark sum to zero.

After the flavor content of the hadron is specified, its identity is unique once the angular momentum assignment is made. Since the string carries no transverse excitations, it contributes no orbital angular momentum, and the total angular momentum of the hadron is determined by the total spin. (Thus only vector and pseudoscalar mesons, and octet and decuplet baryons, are accommodated by the model.) For mesons, the spin is chosen to be one or zero in accordance with a V/(V+P) weighting factor that is left as a free parameter of the model.

At this point the identity of the hadron is known (as is its p_T); its mass m_h is chosen from the appropriate resonance line shape (which is a δ-function for stable particles). A quantity called "transverse mass" is defined by $m_T^2 = m_h^2 + p_T^2$. This is used in determining the only remaining piece of information necessary to

completely describe the kinematics of the hadron, its longitudinal (with respect to the string) momentum.

This longitudinal momentum, p_l, is drawn from a probability function (called the "fragmentation function") similar in purpose to $f(z)$ in the IF model. In the Lund model the fragmentation function $f(z)$ is given by

$$f(z) \propto \frac{(1-z)^a}{z} \exp\left(-\frac{bm_T^2}{z}\right) \tag{2.5}$$

where z is the fraction of the light cone variable $(E + p_l)$ available in the string that is carried off by the hadron. Called the Lund symmetric fragmentation function (LSFF), this has been shown to be the only possible form for a Lorentz covariant fragmentation function under certain general assumptions about the shape of the central rapidity distribution, and under the requirement that the resulting event should not depend (on average) on which end of the string the fragmentation begins at [15]. (The most general form of the LSFF is actually a little more encompassing in that a may depend on flavor, but Equation 2.5 is the implementation of the LSFF in the Lund package used in this thesis.) The formation of hadrons continues until the $(E + p_l)$ remaining in the string falls below a cutoff, at which point the remaining string decays into two hadrons according to two-body phase space.

So far in this description no provision has been made for gluons. Gluons are incorporated as kinks in the string as pictured in Figure 2.3; two pieces of string may contact a gluon by virtue of its two color indices. (In contrast, strings must always terminate on quarks, which carry only one color index.) The SF method can thus be mated with any hard QCD approximation scheme: whatever the partonic configuration presented by the hard QCD event generator, one connects the partons by a string (appropriately kinked at the gluons) and turns loose the SF algorithm.

The Lund model does well in reproducing experimental results. Its main

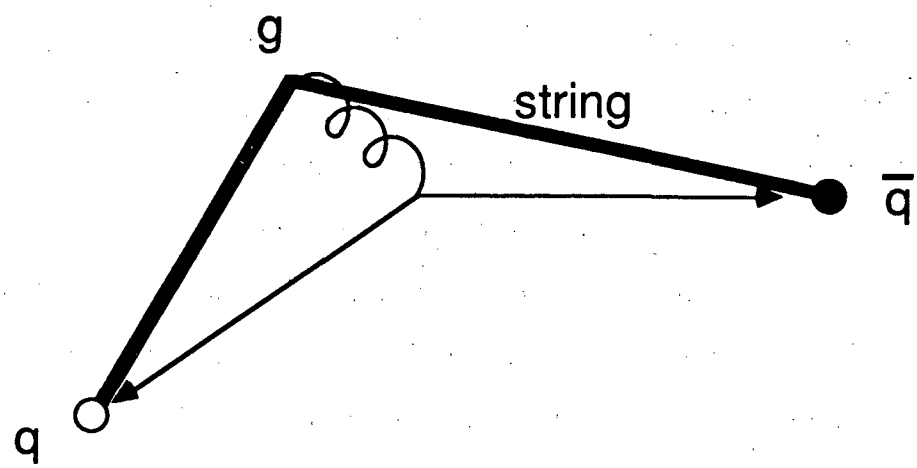

Figure 2.3: Incorporating gluons into the Lund model by introducing a kink in the string.

α_s	a	σ_q	b	s/u	$\left(\frac{V}{V+P}\right)_{u,d}$	$\left(\frac{V}{V+P}\right)_{s}$	$\left(\frac{V}{V+P}\right)_{c,b}$
0.183	0.955	0.350 GeV/c	0.6	0.30	0.5	0.6	0.75

Table 2.1: Values of Lund v5.3 parameters used in this thesis.

drawback as a model is its plethora of free parameters: what is gained in flexibility and accuracy is lost in lack of physical insight and decreased universality.

I use the Lund Monte Carlo extensively in this thesis. I always use Lund v5.3 with the $O(\alpha_s^2)$ ME scheme for the hard QCD phase. The parameters have been left at default, except for three — α_s, σ_q, a — which have been tuned to reach agreement with several experimental measures of momentum flow at PEP [16]. The values of these parameters, as well as some relevant default values, are listed in Table 2.1. (The only time different parameters are used is in Chapter 8, where I perform a different tune of parameters taking the values of Table 2.1 as a starting point.)

2.3.3 Cluster Fragmentation

The central concept of cluster fragmentation (CF) models is that of preconfinement. Preconfinement is a phenomenon resulting from the fact that in LLA events, color flow lines tend not to cross. The partons arising in the LLA scheme can therefore be grouped into localized color singlet objects, called clusters [17]. Figure 2.4b shows the color flow and resulting clusters for the LLA event of Figure 2.4a. Being a color singlet, a cluster is capable of decaying directly to color singlet hadrons; it is also at least partly screened from the internal color charges of its neighboring cluster and hence approximately free to decay to hadrons independently of other clusters. These clusters appear at the mass scale where α_s approaches unity, regardless of the original Q^2 available in the primary interaction. The clusters' universal mass scale, their existence as color singlets, and their independent decay to hadrons gives clusters some hadron-like properties, hence the term preconfinement (in analogy to confinement of hadrons).

A CF model, then, combines the assumption of clusters with an *Ansatz* for their decay to hadrons. (Note that CF only works in conjunction with the LLA approach to hard QCD processes.) A fruitful *Ansatz* for cluster decay, proposed by Wolfram [18], is that $q\bar{q}$ clusters decay (through auxiliary creation of a sea (di)quark pair) isotropically into two hadrons whose identity is determined — consistent with the cluster flavor content — entirely according to probabilities proportional to available phase space. That is, all sea quark pairs are assumed to be equally likely; all possible hadron pairs are considered as cluster decay products, each weighted solely by their available phase space. Thus the suppression of strange hadrons and vector mesons is understood to be due only to their generally higher mass. The p_T distribution falls out naturally in this algorithm, too, without recourse to a separate parameterization.

This cluster decay *Ansatz* was taken by Webber as the basis for his CF model

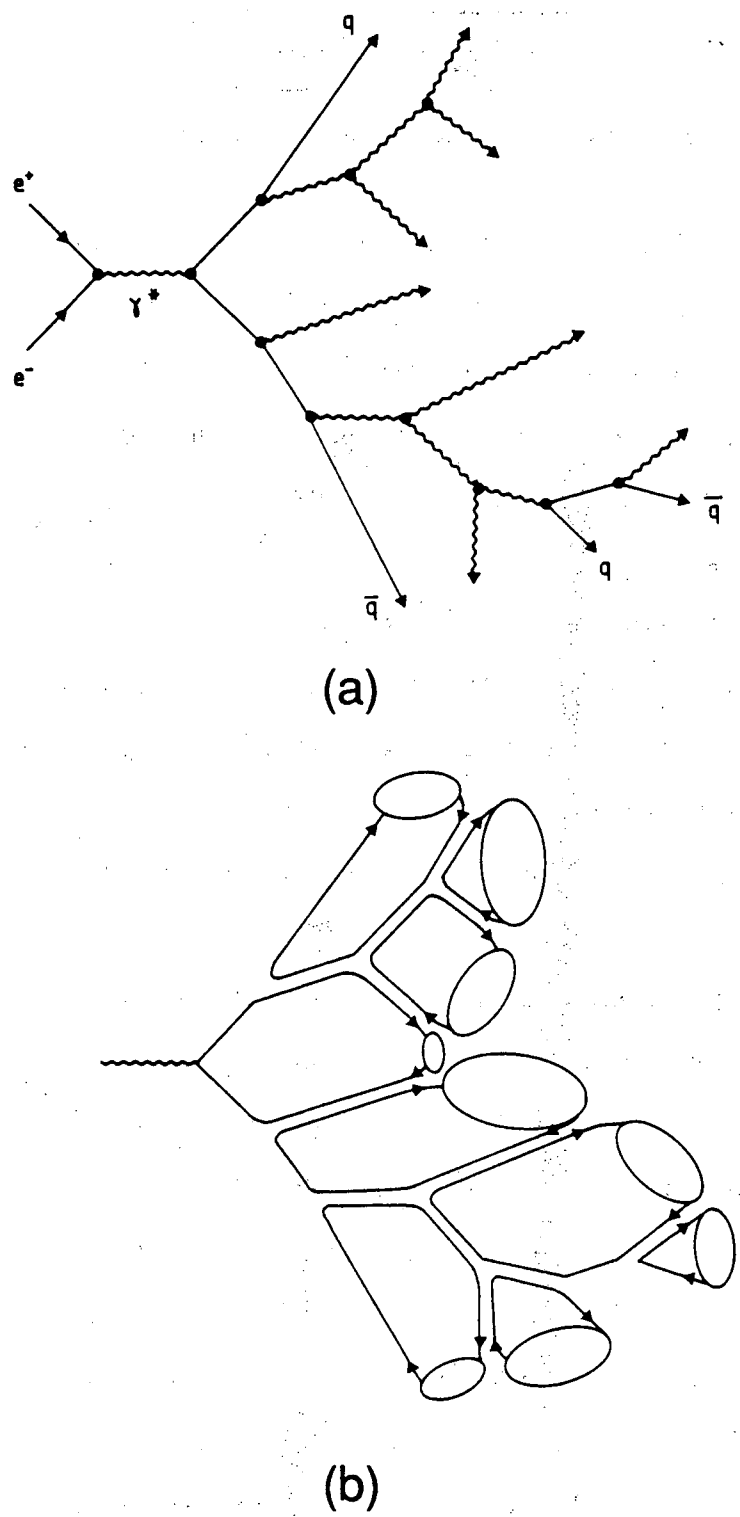

Figure 2.4: (a) A typical LLA parton shower. (b) The color flow of the same event, after gluons split into $q\overline{q}$ pairs; the blobs represent preconfinement into color singlet clusters. (Diagrams from Webber [3].)

Λ_{QCD}	Q_0	M_f
0.25 GeV	0.6 GeV	3.5 GeV

Table 2.2: Parameter values used in Webber v3.0 Monte Carlo.

[3]; I use the Webber v3.0 Monte Carlo extensively in this thesis with all parameters taken at default. Following Wolfram's lead, Webber requires all gluons remaining at the end of LLA evolution to split into $q\bar{q}$ pairs before the formation of clusters, so that all clusters consist of $q+\bar{q}$ with no gluons. This $g \rightarrow q\bar{q}$ splitting was imposed on the event of Figure 2.4a before the color flow in Figure 2.4b was established.

The only parameters of the Webber model are Λ_{QCD} and the virtuality cutoff of the parton shower Q_0, and the maximum allowed cluster mass M_f. (Clusters more massive than M_f fission into two clusters before application of the isotropic cluster decay algorithm.) Quark masses are set to $m_b = 5.3$ GeV, $m_c = 1.9$ GeV, $m_s = 0.5$ GeV, and $m_u = m_d = 0.3$ GeV. The default values for the model's parameters are listed in Table 2.2.

To weight all possible decay products by their available phase space, one must have an assumed table of allowed decay products. Webber v3.0 uses as allowed decay products all 0^-, 1^+, 1^-, and 2^+ SU(3) mesons, all $\frac{1}{2}^+$ and $\frac{3}{2}^+$ octet and decuplet baryons, and well-established charmed hadrons. Bottom quarks are decayed weakly before cluster formation, so that the only quarks remaining to form clusters are u, d, s, and c.

The Webber Monte Carlo has the beauty of using a minimum of free parameters to define an algorithm that works to reproduce a wide range of observed phenomena. When the model has been demonstrated to have shortcomings, Webber has patched it in various ways to better agree with experiment; the improved agreement comes at the cost of introducing extra parameters and as-

sumptions. Some of the changes in versions subsequent to v3.0 are mentioned in Section 2.3.5.

2.3.4 UCLA Model

A recent modification of the Lund scheme has been advanced by Buchanan and Chun at UCLA [19]. In this UCLA model, the LSFF of Equation 2.5 is reinterpreted as a simultaneous probability density in m_h, p_T, and $z = (E+p_l)_{hadron}/(E+p_l)_{jet}$. That is, the hadron's identity and momentum are selected simultaneously at the hadron level, with no quark level parameters such as s/u or qq/q. The scheme is iterative, so that each potential hadron is weighted by its Clebsch-Gordan coupling to potential sea quarks (which automatically accounts for spin counting) as well as weighted by the LSFF. Because selection of $s\bar{s}$ sea quarks (instead of $u\bar{u}$ or $d\bar{d}$) produces *two* heavier hadrons, the overall probability of a given decay chain will be suppressed by more than is apparent from the *single* heavier hadron appearing at one stage of the iteration. To account for this, all possible decay chains from two future iterations are also weighted into the hadron selection.

Since the selection of produced hadrons depends only on the final state hadrons themselves, and because the global decay sequence is weighted by coupling successive fragmentation iterations, this method is in the spirit of reproducing an overall global quantum mechanical transition from initial state to final state. All s/u and V/(V+P) suppression is accounted for by suppression of higher mass hadrons in a highly constrained manner: the only free parameters of the model are a and b in the LSFF. The automatic suppressions and few free parameters are advantages of this model in common with CF models.

2.3.5 Experimental Status of Models

Of the SF, CF, and UCLA models just described, none stands out from the others as clearly better or worse; each has regimes where it performs well and where it performs poorly. I will touch on some of the major experimental arenas where the models are tested.

Each predicts the pseudoscalar and vector meson and octet and decuplet baryon multiplicities reasonably correctly [20,19]. Each fails to predict inclusive π, K and p differential cross-sections and fractions correctly over some significant momentum interval [21]. The IF model suffers because only it fails to reproduce the "string effect" in three jet events (the phenomenon that the region between two quark jets is less populated than that between quark and gluon jets) [22,23].

The Webber model predicts too few hadrons at high x, an artifact of the two-body decay of the cluster which guarantees that no single hadron gets all the available energy [24,21]. (This has been cured in Webber versions subsequent to v3.0 by allowing some clusters to "decay" to a single hadron.) Webber v3.0 also fails to reproduce the observed peaking of $p\overline{p}$ production in the jet direction; this is an artifact of isotropic cluster decay [25]. (Subsequent versions allow some $g \rightarrow qq\overline{q}\overline{q}$ splittings which creates three-quark clusters to alleviate this discrepancy. The baryon decay products of these clusters tend to follow the clusters' boost, which is in the direction of the jet.)

Both the Lund and Webber models as used in this thesis fail to predict rapidity distributions correctly for events with sphericity intermediate between two and three jet events [26]. (Lund v6.3, which implements a parton shower to generate the hard QCD parton configuration, does much better.) The LLA-based Lund v6.3 and Webber Monte Carlos yield a momentum spectrum for the gluon jet in three jet events softer than quark jets, in agreement with data; Lund using the ME scheme predicts a gluon jet spectrum that is too hard [27,20].

Chapter 3

Experimental Apparatus

3.1 PEP

The data used in this dissertation were collected by the TPC/2γ detector facility. This facility is operated at Interaction Region 2 of the PEP e^+e^- storage ring, located at the Stanford Linear Accelerator Center. This storage ring contains counter-rotating beams of electrons and positrons, each beam consisting of three discrete bunches which meet at six interaction regions. The beam energy is 14.5 GeV for a total center-of-mass energy of 29 GeV. Beam crossings occur every 2.44 μsec; a typical operating luminosity is $\sim$ 1–2 x 10^{31} $cm^{-2}sec^{-1}$. With a cross-section of 0.4 nb for e^+e^- annihilation into a $q\bar{q}$ pair at 29 GeV, this means annihilation-channel hadronic events occur once every $\sim$ 2–4 minutes.

3.2 Detector Systems

3.2.1 TPC/2γ Detector Facility

The TPC/2γ detector facility is an assembly of several detector and support subsystems. It has been described in detail elsewhere [28]. It is a so-called "general purpose" detector, designed to detect and record as much information about interesting events as possible, for later offline analysis. The overall geometry is an azimuthally symmetric "barrel" structure of components concentric about the

beamline, plus fore and aft "endcap" components.

The TPC/2γ facility is shown in a longitudinal section in Figure 3.1, with the central elements isolated in Figure 3.2 and Figure 3.3. The detector closest to the interaction point is the Inner Drift Chamber (IDC), a wire chamber used for triggering. The next detector outside of this in the barrel portion of the facility is the Time Projection Chamber (TPC), a proportional wire chamber that provides the main charged particle tracking and particle identification. Surrounding this is a superconducting magnet creating a 13.25 kG solenoidal field in the TPC to enable momentum measurement of the recorded tracks; specially shaped pole-tips in the endcap ensure uniformity of the field. Outside the magnet is the Outer Drift Chamber (ODC), a wire chamber used for triggering and tagging of photons that convert in the magnet. External to this is the Electromagnetic Hexagonal Calorimeter (HEX), a wire chamber sampling shower counter operated in limited Geiger mode. The outermost system in the barrel geometry is the muon detection system, consisting of shielding iron to absorb particles other than muons (and to provide a return magnetic flux path) and wire proportional chambers. The endcap detector closest to the interaction point is the Pole-Tip Calorimeter (PTC), a wire chamber sampling shower counter operated in proportional mode. Outside of the PTC are more muon system layers of absorber iron and wire chambers. Further out, and providing coverage at angles closer to the beamline, are assemblies of detectors known collectively as the Forward Detectors, which are used primarily in the detection of two-photon events. The IDC, TPC, and PTC are inside the same 8.5 atm pressure volume, delimited by an inner radius pressure wall, the magnet cryostat, and the magnet pole-tips; the other gas chambers operate at 1 atm.

The analysis in this thesis overtly uses only the charged particle tracking and particle identification information from the TPC, the other subsystems being

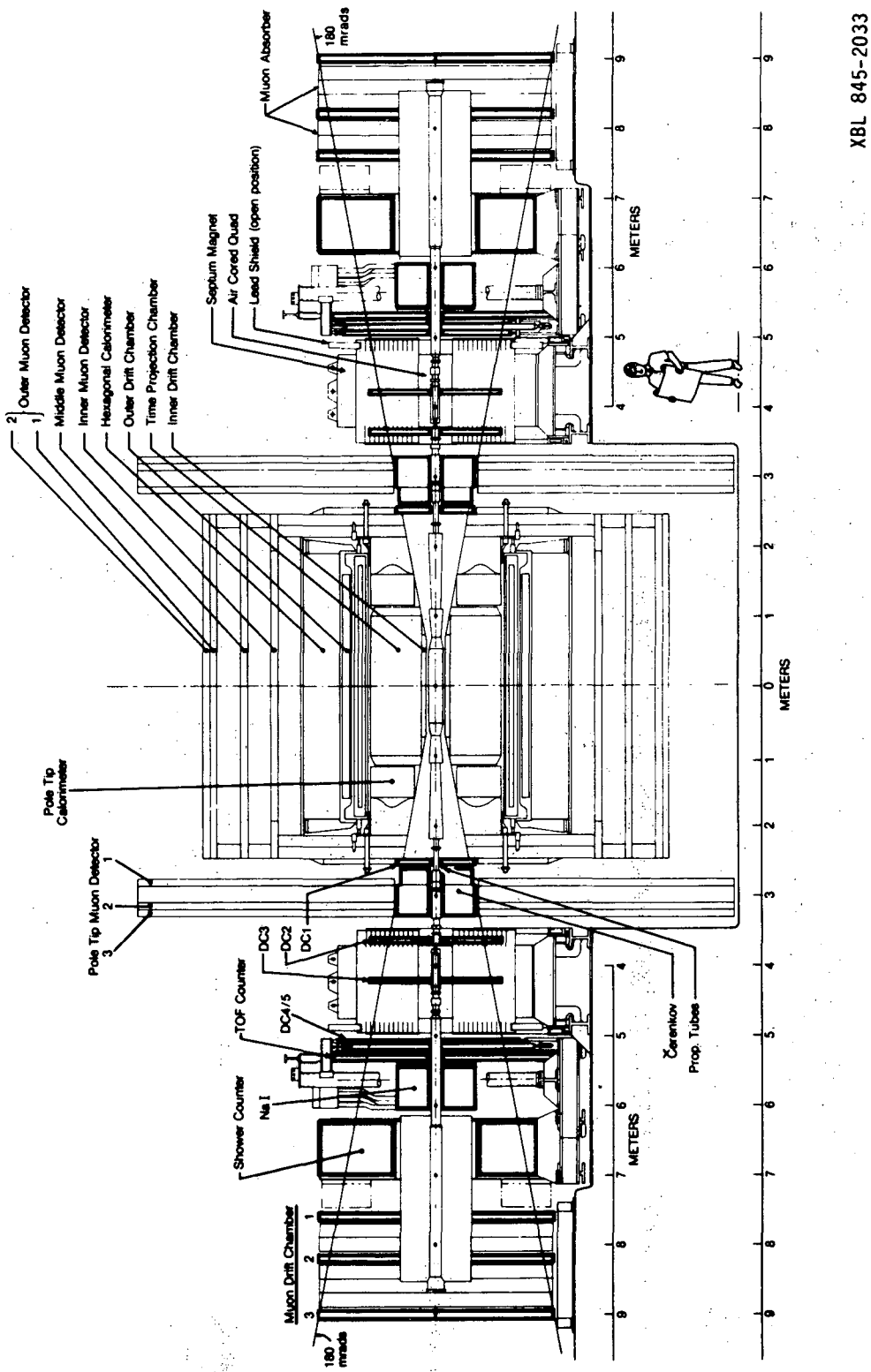

Figure 3.1: Longitudinal section of the TPC/2γ detector facility.

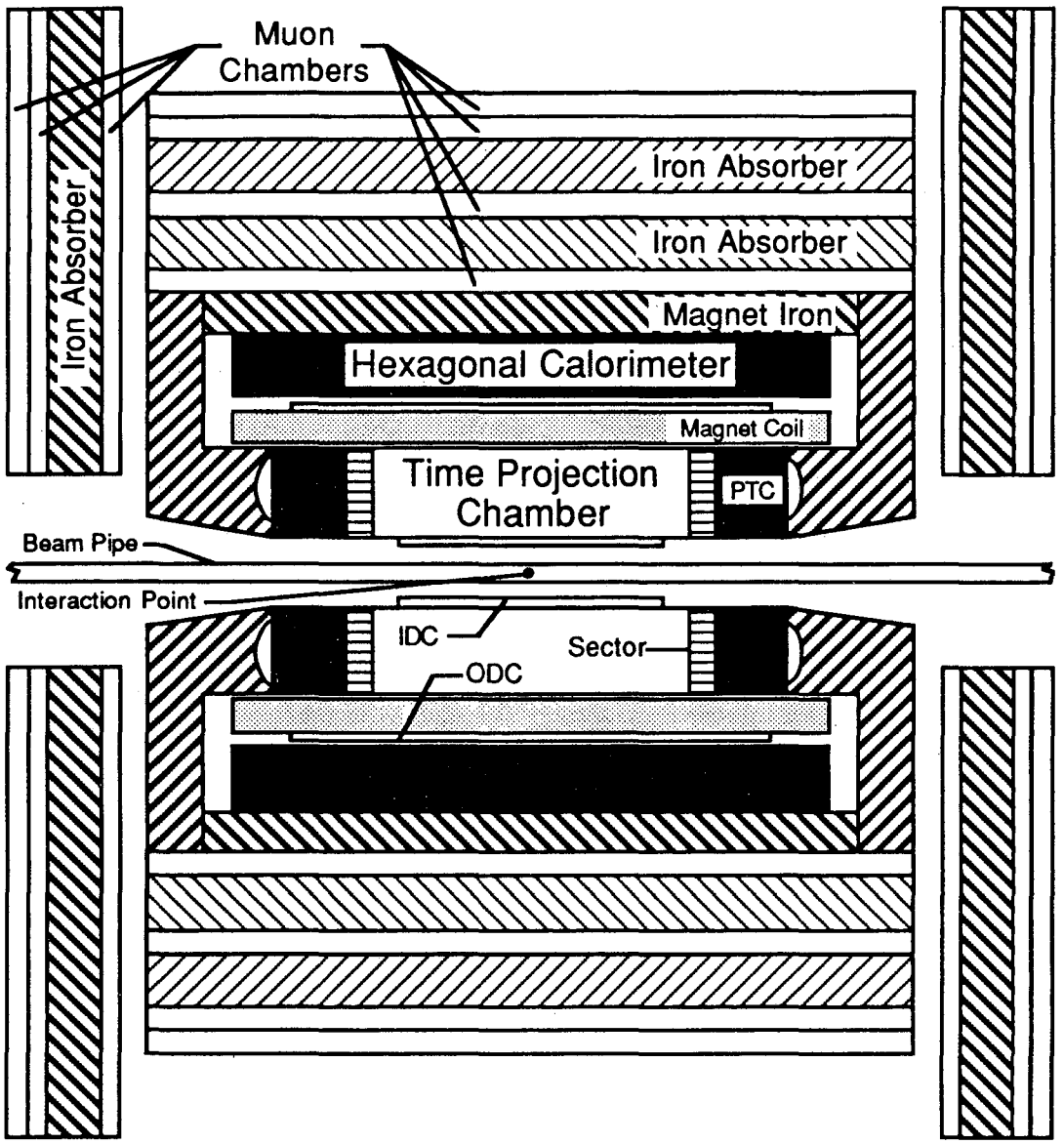

Figure 3.2: Longitudinal section of the TPC/2γ detector facility, omitting the Forward Detectors.

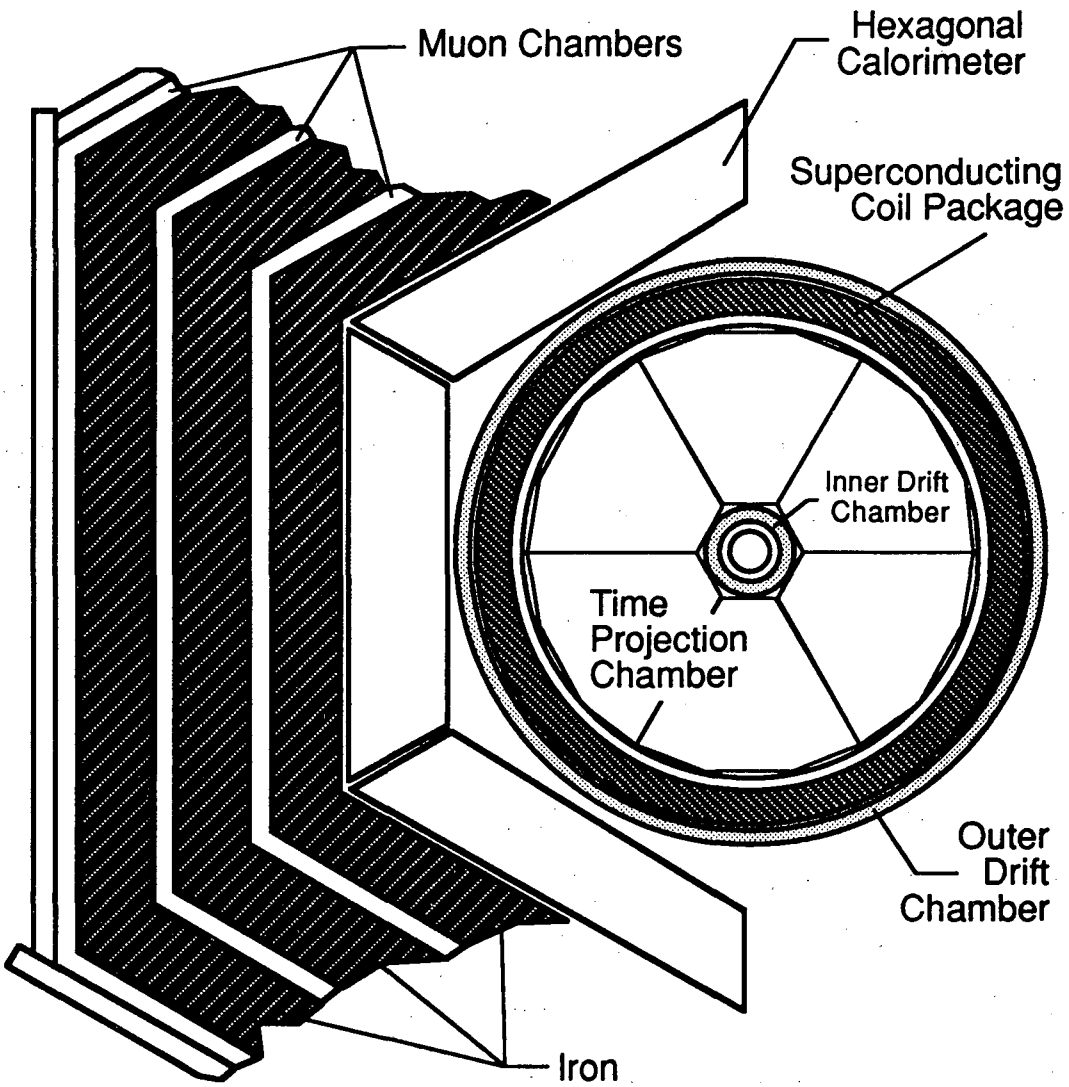

Figure 3.3: Partial cross-section perpendicular to the beam direction of the barrel components of the TPC/2γ detector facility.

relevant only through their role in triggering. I will therefore describe the other systems only briefly, but the TPC in some detail.

IDC

The IDC [29,30] is 1.2 m long, extending in radius from about 13 cm to 19 cm. This covers 95% of 4π solid angle. It contains four cylindrical layers of 60 axial sense wires each; the wires in a layer are spaced evenly in azimuth, with 1.2 cm radially between layers. The volume is divided electrostatically into cells about each sense wire by field-shaping wires. Each layer is offset azimuthally from its neighbors by a one-half cell rotation. The wires operate in proportional mode in an 8.5 atm argon (80%)-methane (20%) gas mixture. This detector provides fast azimuthal information for triggering, but no longitudinal information.

ODC

The ODC [30] is 3 m long, extending in radius from 1.19 m to 1.24 m. This covers 77% of 4π solid angle. It contains three cylindrical layers of 216 axial sense wires each; the wires in a layer are spaced evenly in azimuth, with 2 cm radially between layers. The middle layer is offset azimuthally from the inner layer by a one-half cell rotation; the outer layer is offset by an additional quarter cell rotation. The wires operate in proportional mode in a 1 atm argon (80%)-methane (20%) gas mixture. Like the IDC, this detector offers only azimuthal track information.

HEX

The HEX calorimeter [31,32,33] consists of six modules, each 4.2 m long and trapezoidal in a cross-section taken perpendicular to the beam. Assembled into a hexagonal geometry surrounding the ODC, this covers 75% of 4π solid angle.

Each module is 10.4 radiation lengths thick, consisting of a 40 layer sandwich of 0.14 cm thick lead plates and 0.6 cm gas gaps containing sense wires. The lead provides a medium for electromagnetic showers which are sampled for magnitude and location by the wire chambers. Inside each gas gap parallel sense wires are strung axially, 0.5 cm apart. The wires are operated in Geiger mode in a 1 atm argon (92.3%)-methylal (5.5%)-nitrous oxide (2.2%) gas mixture. Nylon filaments strung perpendicular to and touching the sense wires limit the Geiger discharges to cells 1.0 cm long. Cathode strips are mounted on the cell walls to capacitively sense the Geiger discharges. These strips run at $\pm 60°$ with respect to the wires on facing walls of a gas gap, so that wire and cathode readout together provide three stereo views of the shower in each layer.

Muon System

The muon system [34] consists of interleaved layers of iron absorber and proportional wire cells operating in 1 atm of argon (80%)-methane (20%). Structurally, these cells are aluminum tubes triangular in cross-section, 8.26 cm high. The barrel portion of the system lies outside the HEX with the same hexagonal geometry. It contains four layers of wire cells, the inner three running parallel to the beam direction, the outermost oriented at 90° to the beam. Between the innermost layer of cells and the HEX is 30 cm of iron, which serves as the magnet return yoke as well as absorber. Between the inner two chamber layers lies an additional 35 cm of iron, with a final 30 cm iron layer lying between the middle two chamber layers. The endcap detectors only contain three chamber layers, the middle one oriented horizontally, the others running vertically; 20 cm of iron sits between the inner layer and the outer two layers. The muon system provides coverage over 98% of 4π solid angle, but with performance varying with the angle of a track, due to the varying thickness (4–11 interaction lengths) of absorber

traversed by the track.

PTC

The PTC [35] consists of two endcap detectors, together covering 18% of 4π solid angle. Each detector is 13.5 radiation lengths thick, consisting of a 51 layer sandwich of lead plates and 0.41 cm gas gaps containing parallel sense wires. The lead thickness and wire spacing is a function of depth into the detector. The direction of the wires in successive layers is rotated azimuthally by 60°, so that three consecutive layers provide three stereo views of a shower. The wires operate in proportional mode in an 8.5 atm argon (80%)-methane (20%) gas mixture.

Forward Detectors

The Forward Detectors provide particle tracking, identification, and calorimetry capabilities at angles close to the beamline, subtending the polar angles 22–180 mrad. A set of five drift chambers perform charged particle tracking. Particle identification is done by threshold Čerenkov counters, time-of-flight counters, and muon chambers behind iron absorbers. Calorimetry duties are split between a NaI array (22–90 mrad) and a lead-scintillator sandwich shower counter (100–180 mrad).

3.2.2 TPC

3.2.2.1 Operation

The TPC is a cylindrical drift chamber 2 m in diameter and 2 m long, operating in an 8.5 atm argon (80%)-methane (20%) gas mixture [36,37]. The chamber is immersed in a 13.25 kG axial magnetic field. Midway down its length a wire mesh at negative high voltage bisects the cylinder to establish an axial electric field pointing from the ground potential endcaps. Metallic equipotential rings in the

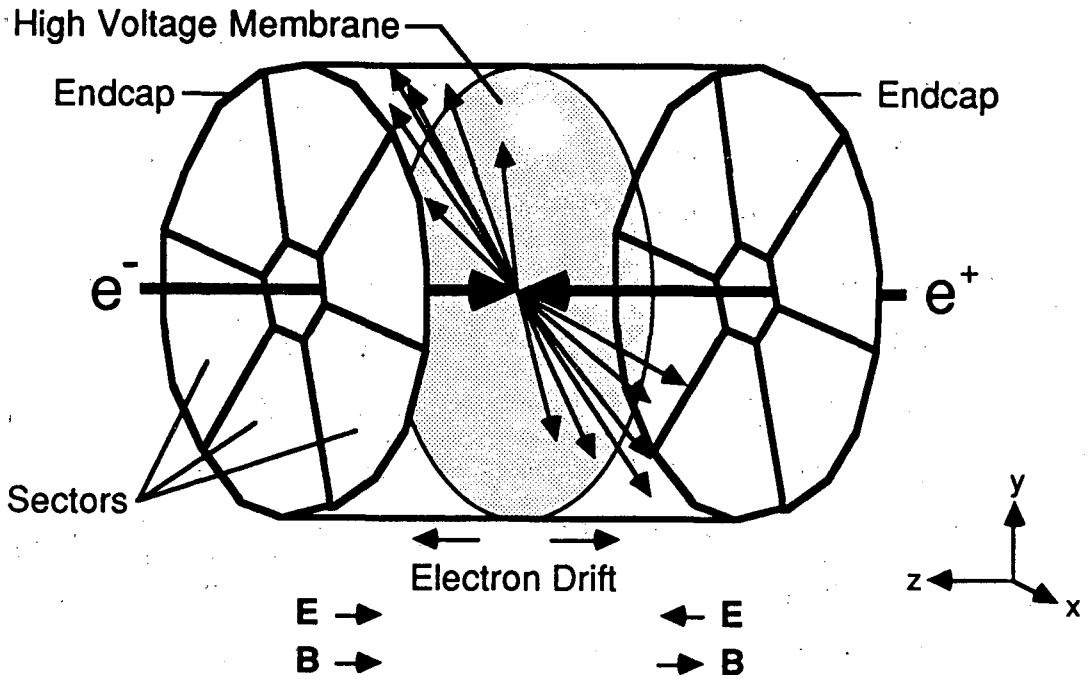

Figure 3.4: Schematic view of the TPC geometry, showing E field, B field, and electron drift directions, and sectors in the endcaps. For simplicity, tracks from the interaction are not shown curving in the magnetic field.

G-10 walls of the TPC enforce uniformity of the electric field. Charged particles traversing the TPC leave ionization trails in the gas; the liberated electrons in this track drift under the influence of the electric field to the endcaps where they are detected by proportional wire arrays. The midplane mesh was initially held at -50 kV for the data used in this thesis, imposing a drift speed of about 3.3 cm/μsec; the voltage was increased to -55 kV partway through the running cycle. Figure 3.4 shows schematically the geometry of the TPC and the electron drift. The right-handed detector coordinate system has x horizontal and pointing outward (roughly east) from the center of PEP, y vertical, and z parallel to the beam (pointing roughly south).

The endcaps, which contain the proportional wire arrays, are each composed

of six identical kite-shaped modules, called sectors. A local right-handed coordinate system is defined for each sector: η points left to right in the plane of the sector face (roughly the azimuthal direction when installed in the TPC), ξ points radially outward along the sector midline in the plane of the sector face, and z points perpendicular to the sector face into the TPC volume. Each sector has 183 parallel sense wires, running in the η direction. The wires are spaced 0.4 cm apart and 0.4 cm above the grounded cathode plane. The cathode plane is subdivided in places into electrically isolated rectangles, called pads, which are virtually grounded through amplifiers in order to sense the capacitively induced signals from avalanches on overhead wires. These pads are 0.75 cm high by 0.70 cm wide, arranged into 15 rows running parallel to the sense wires, with 0.05 cm between pads in a row. Each pad row is centered under a sense wire, receiving effectively their entire induced signal from the five closest wires. The centers of the pad rows are located at the following ξ distances (in cm) from the interaction point: 23.6, 28.4, 33.6, 38.8, 44.0, 49.2, 54.4, 59.6, 64.8, 70.0, 75.2, 80.4, 85.2, 90.0, and 94.8. The arrangement of pad rows and sense wires in a sector is shown schematically in Figure 3.5; the configuration of sectors in the endcaps is shown schematically in Figure 3.4.

The arrangement of wire grids above the cathode plane is shown in Figure 3.6. The sense wires are interleaved with field wires which help shape the electrostatic configuration near the sense wires. A grounded grid of wires, called the shielding grid, is located 0.4 cm above the sense and field wires. The shielding grid defines the ground plane seen by the TPC midplane high-voltage mesh, and separates the proportional cells from the electron drift region. Above the shielding grid by an additional 0.8 cm is a grid of wires called the gating grid.

The gating grid acts as a normally closed "electronic shutter." In its open (transparent) mode, the wires of this grid are set to V_{GG}, a negative voltage such

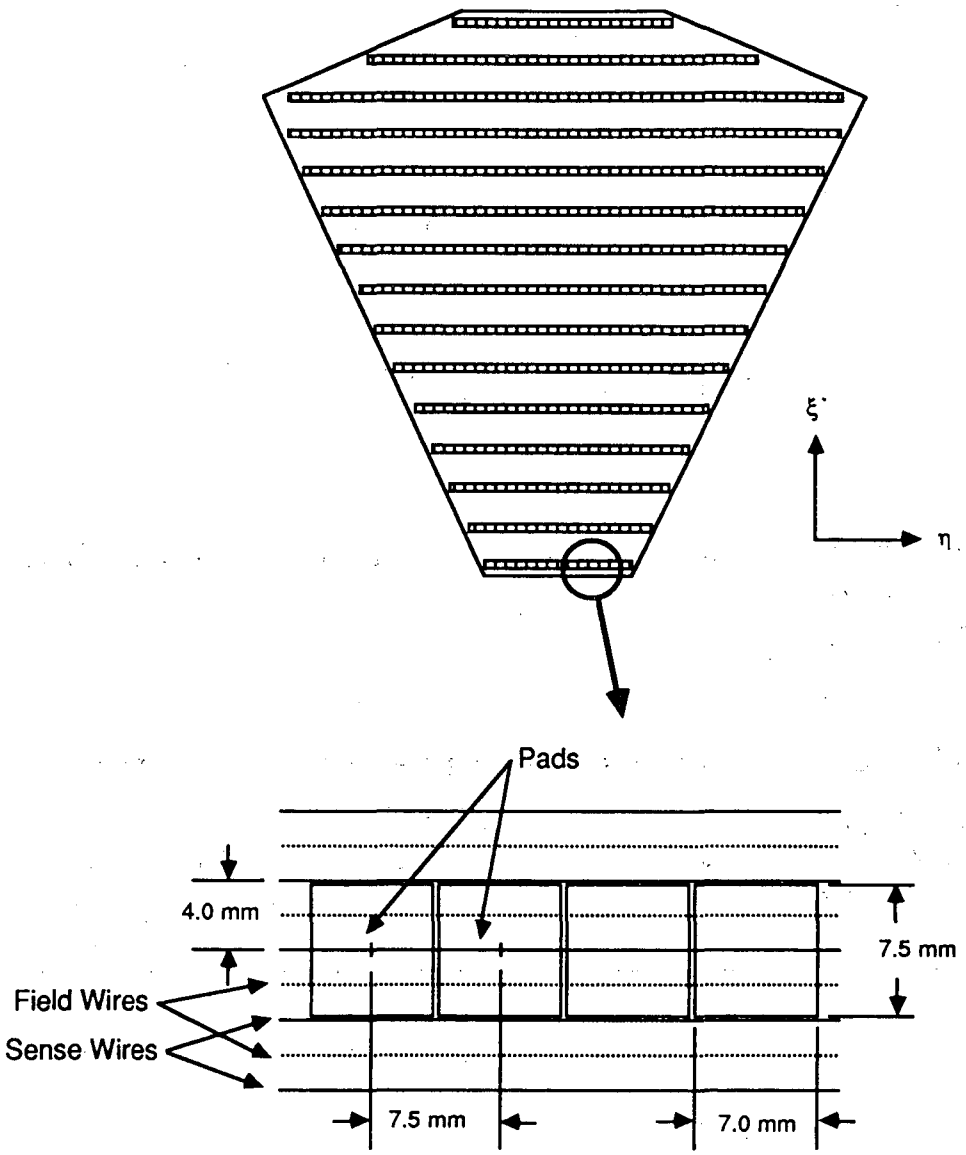

Figure 3.5: Schematic view of a sector, with a close-up of part of a pad row.

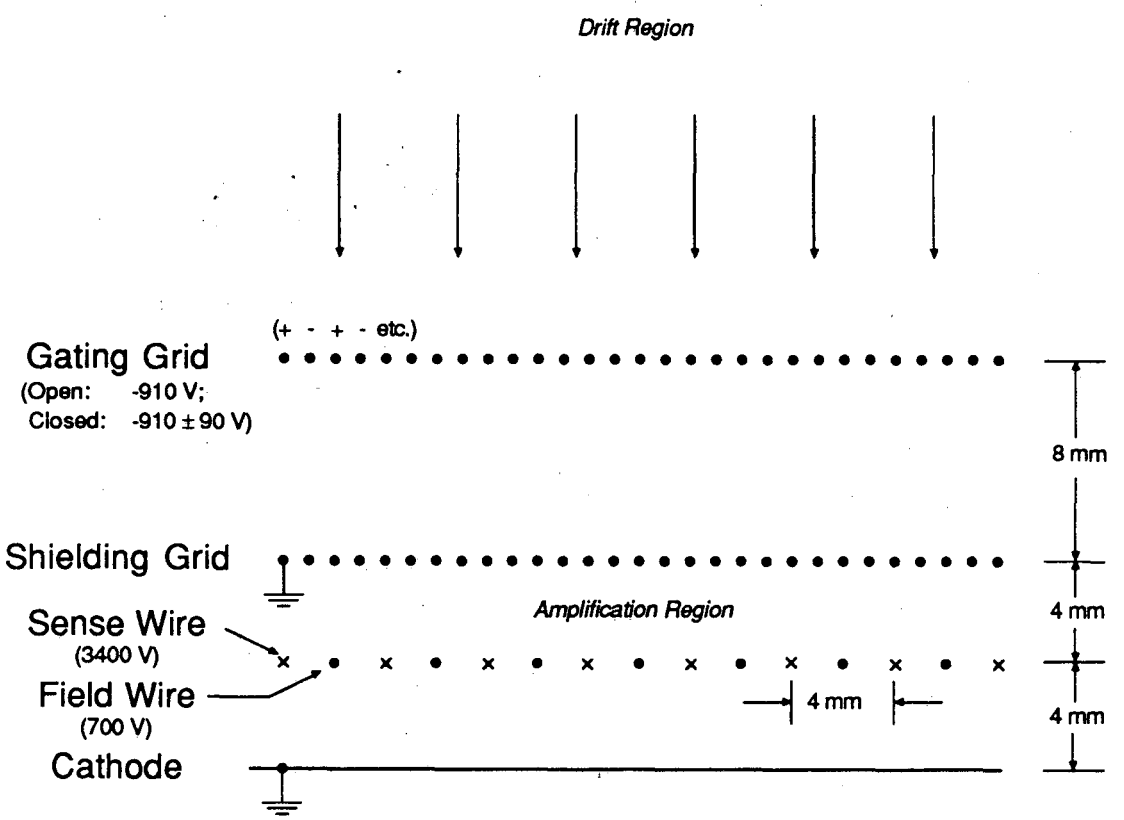

Figure 3.6: Configuration of wire planes above the cathode plane of a sector.

that field lines running from the drift region to the sense wires are uninterrupted: drifting electrons can reach the sense wires. (In practice, V_{GG} roughly doubles the field between the gating grid and the shielding grid relative to the drift field in the main volume of the TPC.) In its closed (opaque) mode, offset voltages $+\Delta V_{GG}$ and $-\Delta V_{GG}$ are added to V_{GG} on alternate wires, which has the effect of deflecting the drift and sense wire field lines to end on the gating grid: both drifting electrons and avalanche-produced positive ions discharge at the gating grid. This grid when closed thereby prevents positive ions from entering the drift region where they would distort the uniform electric field by their space charge, and hence distort the apparent trajectories of reconstructed tracks. In use, the gating grid is left closed until a pre-pretrigger decision (described in Section 3.3) switches it open just long enough for the ionization trails of interest to drift to the sense wires; it closes again before the slowly-moving positive ions can escape into the drift region.

The ionization trails from charged particle tracks drift to the sectors, where amplitude and arrival time are measured for the resulting pulses on wires and pads. Because the drift field is uniform, the ionization lands on the endcaps as a direct axial projection of the original ionization trail. The locations of the hit pads give two-dimensional (x-y) information about the location in space of the original ionization trail; the arrival time, coupled with knowledge of the electron drift speed, gives the axial third coordinate (z). The pad signals therefore give three-dimensional space points along a track, from which the track can be reconstructed. The curvature of the track in the axial magnetic field is proportional to its (transverse) momentum and its electric charge, so reconstructing the helical trajectory of a particle enables the measurement of these quantities. The wire signals only give two-dimensional spatial information, which can be used to refine the spatial information of the pads. More importantly, the amplitudes of the

wire signals constitute a large number of independent samples of the particle's ionization energy loss per unit track length, dE/dx. This ionization energy loss is a function only of the speed of the particle, so measuring dE/dx measures speed; coupled with the simultaneous measurement of momentum, this amounts to a mass — i.e. particle identity — measurement. This ability to identify charged particles is the greatest strength of the TPC/2γ detector facility. I discuss particle identification in more detail in Section 4.1.2.

Tracks need to cross at least three pad rows to define the helical orbit. The angular coverage of tracks in the TPC that cross at least three pad rows is about 95% of 4π solid angle.

To detect pulses on wires and pads, the signals are coupled to preamplifiers mounted on the backs of the sectors. These preamplifiers integrate charge to form a step output with a long decay. These output steps are amplified and shaped to pulses having a rise time of $\sim$ 250 nsec (with comparable decay time) by shaper amplifiers located outside the detector's radiation shielding. These shaped pulses are sampled every 100 nsec by a "bucket brigade" linear CCD shift register, each sample being passed to the next bucket at every CCD clock. The CCDs are 455 buckets long, and so can hold a total time history of 45.5 μsec of shaper amp output at the normal 10 MHz clock rate. If a trigger decision (Section 3.3) is made to read out the event, the clock rate is slowed to 20 kHz so that (relatively slow) 9-bit ADCs can digitize the CCD samples. Zero-suppression is performed by comparing the ADC counts to software-controlled thresholds; counts exceeding threshold are read along with their bucket number (i.e. time) into the online data acquisition VAX 11/782 computer.

A minimum ionizing track typically has 5–7 ADC buckets above threshold for each wire or pad signal, with a maximum wire signal of $\sim$ 70 ADC counts above pedestal. A parabola is fit to the three largest ADC counts to define the

magnitude and arrival time for that pulse. A track typically induces signals on 2–3 adjacent pads in a pad row, so hits on adjacent pads arriving at nearly the same time are grouped to determine a space point for a track by simply averaging (weighted by pulse heights) the pad positions and arrival times.

These rudimentary space points allow pattern recognition programs to identify tracks and associate the corresponding wire hits with them. Once this is done, the track direction and wire information is used to refine the space points. The location of a space point in η is determined by a gaussian fit to the amplitudes of the grouped pads; if less than three pads are above threshold then the width of the gaussian is fixed by a parameterization as a function of drift distance and track angle α, where α is the angle of the track with respect to the pad row in the x-y plane. A small correction,

$$\Delta\eta = \left[\sum_{i=-2}^{2} i w_i H_i / \sum_{i=-2}^{2} w_i H_i \right] D \tan\alpha,$$

is applied to account for ionization fluctuations in the five wires closest to the pads, where

w_i is the wire-to-pad coupling weight for wire i,

H_i is the pulse amplitude on wire i,

D is the spacing between wires, and

$i = 0$ labels the wire centered on the pad row.

The location of a space point in ξ is taken to be the pad row center, plus a correction

$$\Delta\xi = \left[\sum_{i=-2}^{2} i w_i H_i / \sum_{i=-2}^{2} w_i H_i \right] D.$$

The location of a space point in z is simply the average of the pad z values weighted by the pad amplitudes. These refined space points are used for subsequent, more accurate, track fitting.

3.2.2.2 Calibration

Calibration of the electronics (i.e. amplifiers, CCDs, and digitizers) is done in two steps. First, the pedestal (the output with no input signal) is measured for each channel. This is a baseline that must be subtracted from the raw ADC counts to arrive at the true signal in a given channel. The pedestal is typically $\sim$ 30 ADC counts (out of a maximum of 511), with a slope of one or two counts per 100 CCD buckets (due to CCD leakage currents). Second, the relative gain curve for each electronics channel is determined by pulsing the shielding grid with precision pulses of several amplitudes to induce signals on the wires and pads. The absolute normalization of this gain curve is not determined. The complete electronics calibration is performed on the order of once a month, with daily monitoring calibrations. The electronics calibration translates the ADC counts to avalanche size at the wires and pads (up to an overall normalization).

Calibration of the gas gain is done in two steps. First, a permanent gain map of each sector was made before installation into the TPC by irradiating the sector (operating in a test vessel) with ^{55}Fe sources in a precise pattern. Gain variations are primarily due to non-uniformities in wire diameters and wire-to-cathode spacing. Second, periodic *in situ* corrections to this gain map are made from the results of irradiating the wires with ^{55}Fe sources located within the sectors. These ^{55}Fe data acquisition runs were made on the order of once a month. Gain variations from pressure, temperature, and sense voltage changes are accounted for by monitoring these variables for every event and correcting the data accordingly. These calibrations translate the wire signal sizes to the amount of initial ionization incident on the wires (up to an overall normalization constant).

In addition to these hardware calibrations, several corrections must be applied to the data that are determined from the data themselves. This requires the data

analysis to be done in several stages in an iterative fashion, using the results from previous analysis stages to refine the various corrections for subsequent, more accurate, analysis stages. This iterative procedure is outlined in the next chapter.

Data collection is divided into runs that typically consist of a few thousand events acquired under a stable configuration of PEP and the detector over a period on the order of an hour. By averaging over many events in a run, values can be determined for slowly time-varying characteristics of the TPC operation. Electron drift speed, precise knowledge of which is needed for z position measurement, is determined by matching the two parts of tracks that cross the TPC midplane, and also by defining drift over the entire TPC length to correspond to the time endpoint of signals in an endcap. Electron diffusion and absorbtion, which both attenuate pulse height as a function of drift distance, are measured by dividing tracks in half and comparing the ionization from the half nearest the endcap to that from the half farthest away. The absolute gain normalization is set by defining the average dE/dx of minimum ionizing pions (a well-identified set of tracks) to be 12.1 keV/cm. The beam interaction point is measured by fitting a common vertex to tracks in an event, then averaging over events.

Additional corrections to the data must also be made on a track-to-track basis. An example of this has already been seen in the track angle dependent corrections to the pad space points. Another instance is that the dE/dx measurement for a track must be adjusted as a function of polar angle, to account for the increased track length integrated by each sense wire when a track is not parallel to the sector.

3.2.2.3 Resolutions

Position Resolution

The position resolutions in both x-y and z are expected to be limited by diffusion of the drifting electrons, electronics noise and miscalibration, and ionization fluctuations at the wires. The position resolution in z is also degraded by uncertainties in the pulse arrival times. The ionization fluctuation contributions should be angle dependent: fluctuations for tracks perpendicular to the pad rows will not affect the x-y measurements, fluctuations for tracks parallel to the endcaps will not affect the z measurement; but for angles other than these, fluctuations can smear the measurements.

Empirical measurements of the position resolutions confirm this angle dependence. Cosmic ray tracks are reconstructed with one pad row excluded from the fit; gaussian fits to the residuals of the excluded space points measure the resolution. The measured resolution in the x-y plane is 120–200 μm, depending on the track angle α; the z resolution is 160–250 μm, depending on polar angle.

Momentum Resolution

The (transverse) momentum of a track is related to its radius of curvature in a magnetic field through the expression

$$R = 3335\frac{p_\perp}{B}$$

where R is the radius of curvature (in cm) of the track, $p_\perp$ is the component of track momentum in the x-y plane (in GeV/c), B is the axial magnetic field strength (in kG), and where the particle's charge magnitude is assumed to be that of the electron. Measuring the curvature of a track thus measures $p_\perp$, which amounts to knowledge of total momentum p if the polar angle of the track is known. In short, measuring momentum boils down to measuring the track.

Component	Inner Radius (cm)	Radiation Length (%)	Cumulative Rad. Length (%)
Beampipe	8.50	2.3	2.3
Cooling Tubes	8.70	0.3	2.6
Pressure Wall	10.95	7.1	9.7
Gas Gap	11.59	0.1	9.8
IDC	13.18	2.6	12.4
Insulator + Field Cage	20.00	3.2	15.6
TPC Volume	22.25	4.9	20.5

Table 3.1: Thickness of material between the TPC and the interaction point.

In the TPC, the final track measurements are performed in the programs TRAGIC and VERTEX. These are run after a preliminary identity assignment has been made for the track based on dE/dx information, so that mass-dependent energy losses in traversing material before entering the TPC and in the TPC gas can be taken into account. The thicknesses of components between the TPC and the interaction point are listed in Table 3.1.

TRAGIC fits tracks using the measurement errors of the space points. The effect of Coulomb multiple scattering is incorporated by adjusting the errors of the fit track parameters. VERTEX finds an event vertex by constraining all tracks to pass through a single point, subject to consistency of that point with the run-averaged beam position; this is done iteratively, discarding tracks inconsistent with the common origin before refitting. The vertex constraint effectively adds an extra space point with a large lever arm to tracks consistent with the common origin, thereby improving the momentum resolution. More on TPC track fitting may be found in reference [38].

The momentum resolution has two *a priori* contributions: measurement error and Coulomb multiple scattering error. The measured quantity is actually $C \equiv 1/p_\perp$, the curvature of the track in units of $(\mathrm{GeV/c})^{-1}$. This measured quantity

is assumed to have gaussian errors of the form

$$(\sigma_C)^2 = A^2/p_\perp^2 + B^2$$

where the first term corresponds to Coulomb scattering (neglecting the dependence on β) and the second term corresponds to measurement error. Since $\sigma_C/C = \sigma_{p_\perp}/p_\perp = \sigma_p/p$, this can be rewritten as

$$\left(\frac{\sigma_p}{p}\right)^2 = A^2 + B^2 p^2.$$

The multiple scattering term A is calculated from formulae in Gluckstern [39], and represents an average over tracks of different polar angles. The measurement error term B is measured using stiff tracks for which the multiple scattering term is negligible. This was done by comparing the curvature in different sectors of cosmic ray tracks and by measuring the width of the curvature distributions for 14.5 GeV tracks in $e^+e^- \to e^+e^-$ and $e^+e^- \to \mu^+\mu^-$ events. Like A, B represents an average over tracks of different lengths and polar angles. The momentum resolution thus determined is

$$\left(\frac{\sigma_p}{p}\right)^2 = (0.015)^2 + (0.007)^2 p^2$$

for tracks satisfying the vertex constraint. For tracks that fail the vertex constraint, the measurement error contribution worsens from $(0.007)^2 p^2$ to $(0.011)^2 p^2$.

dE/dx Resolution

The dE/dx resolution is determined from a sample of minimum ionizing pions. It can be parameterized as a function of the number of wires used to determine dE/dx and of the polar angle of the track, and is found to be gaussian to three standard deviations. The dE/dx resolution averaged over tracks with at least 120 wire samples is 3.4%. The dE/dx measurement from a single pad is more reliable than that from a single wire because it integrates over several wires; pads

are used instead of wires to determine dE/dx if the number of usable wires is less than 2.5 times the number of usable pads.

3.3 Trigger

Beam crossings occur once every 2.44 μsec, but events of physics interest occur some 5–6 orders of magnitude less often. Since it takes about 30 μsec to drift out the entire TPC volume, and about 80–100 msec to completely digitize and store an event, it is clear that the detector cannot be read out at every beam crossing. It is the rôle of the trigger — a network of fast digital electronics — to identify events of potential interest for readout, otherwise leaving the detector live for subsequent beam crossings.

The trigger decision is made in three steps. Each step has progressively more information available to it, so can apply tighter criteria to the decision of whether to advance to the next (more time-consuming) step or to abort the current event and reset the detector. The first step is the pre-pretrigger. This makes the fast (< 2 μsec) decision of whether to open the gating grid to activate the TPC, or to reset the detector in time for the next beam crossing. The second step is the pretrigger. This uses information from the first few μsec of drift in the TPC and calorimeter readout to decide whether to allow sufficient time for all TPC tracks to drift to the endcaps, or to close the gating grid and reset the detector. It makes this decision within 7.5 μsec after the pre-pretrigger. The third step is the trigger itself. It uses TPC and calorimeter information to decide whether to digitize and read out the event, or whether to ignore the event and reset the detector. The trigger makes its decision about 35 μsec after the pre-pretriggering beam crossing.

The Forward Detectors can also generate pre-pretriggers, pretriggers, and triggers. Since these are triggers for two-photon events, I do not discuss them in

the following descriptions. These descriptions are simplifications of complicated logic; see, for example, references [40,16,41] for greater detail.

Pre-pretrigger

The pre-pretrigger uses information from the IDC, ODC, TPC (from tracks piercing the endcap), and ganged signals in the HEX and the PTC. The charged pre-pretrigger requires at least two hits in the IDC separated by 60° or more, and either any ODC hit or two TPC wire hits azimuthally coincident with the IDC hits. At a luminosity of 2 x 10^{31} $cm^{-2}sec^{-1}$, the pre-pretrigger rate is $\sim$ 1.5 kHz.

Pretrigger

TPC information drifted from the few centimeters nearest the endcaps, and larger calorimeter ganged signals are new information available during the pretrigger window. The charged pretrigger requires two IDC hits azimuthally consistent with ODC hits, or one such IDC-ODC coincidence plus an IDC hit azimuthally consistent with signals on several TPC wires, or two such IDC-TPC coincidences. At a luminosity of 2 x 10^{31} $cm^{-2}sec^{-1}$, the pretrigger rate is $\sim$ 500 Hz.

Trigger

There are four charged triggers, two neutral triggers, and one charged-plus-neutral trigger defined. The variety of triggers allows for triggering on events of different classes (hence different topologies) and redundancy of the trigger decision. Most important of these triggers is the charged "ripple trigger." Latches ganging sets of eight adjacent TPC wires are enabled if at least four wires are hit within a time window; the latch is set if the latch corresponding to the next larger radius is set within an earlier time window. A track emanating from the interaction point at the midplane of the detector will have its ionization near the beampipe arrive at the sectors last, with ionization from larger radii arriving

correspondingly earlier, depending on the polar angle of the track. It should thus set off the domino-like cascade of latches, called a ripple. The ripple trigger is satisfied if two ripples occur in two different sectors.

At a luminosity of 2 x 10^{31} $cm^{-2}sec^{-1}$, the trigger rate is $\sim$ 2 Hz. Due to the large energy and multiplicity of $q\bar{q}$ events, several triggers are usually easily satisfied for each event; the trigger efficiency for $q\bar{q}$ events is thus over 99%.

Chapter 4

Data Reduction, Event Selection, and Event Simulation

4.1 Data Reduction

4.1.1 Analysis Sequence

As mentioned earlier, analysis of TPC data must be done in an iterative fashion. A first pass through the data is done using the best available information (nominal values or averages of preceding runs) for run-dependent constants. The results of this first pass are used to refine these constants, which are then used in a second, more accurate, pass through the data. Later passes use corrections from the analyzed data (averaged over hundreds of runs) for yet more detailed refinements of analyzed data.

Interspersed with the analysis programs are filter programs which decide which events to pass on to the next stage of analysis. Separate analysis streams exist to distill selected events into condensed Data Summary Tapes (DSTs) for two-photon, $\tau\overline{\tau}$, or $q\overline{q}$ events. The DSTs contain summary information for each track and event, but no raw data. I will describe the analysis stream leading to the $q\overline{q}$ DSTs [42]. A schematic flow chart of this sequence is pictured in Figure 4.1.

In order for the raw data to be written to tape, it must first pass the PRE-

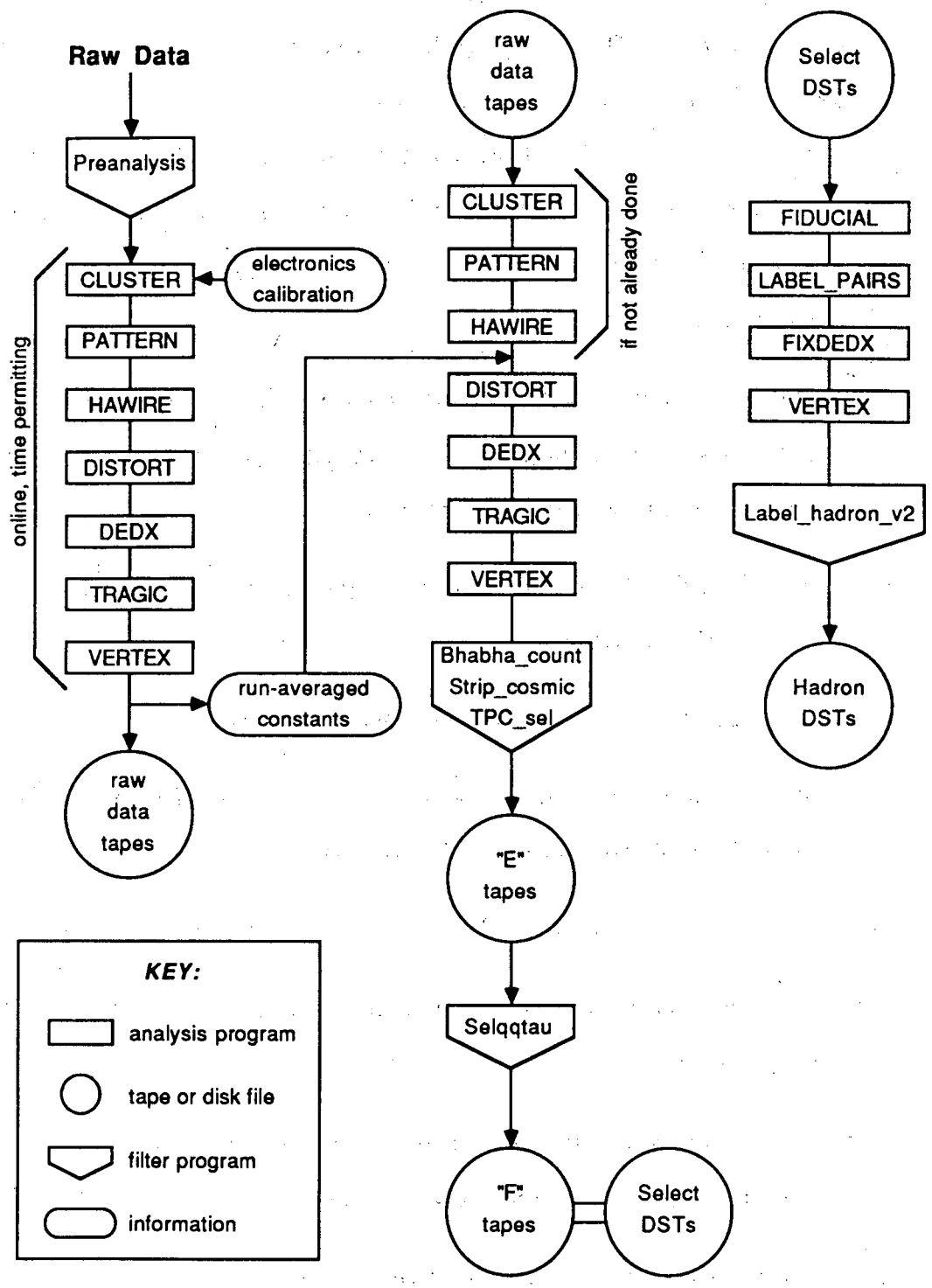

Figure 4.1: Analysis sequence leading to DSTs for annihilation $q\bar{q}$ events. Only the flow for TPC information is depicted. The filters are actually interspersed with analysis code, and are shown grouped only for pictorial convenience. Final distortion and dE/dx corrections described in the text are not pictured.

ANALYSIS filter. This is essentially a software online verification of the hardware trigger; it passes $\sim$ 65% of triggered events. About 1500 raw data tapes were written during the 1984–86 running cycles.

The basic sequence of analysis programs is then executed online, if time permits between triggers; the results of the analyses are written to the raw data tapes along with the data themselves. This analysis sequence consists of the following programs:

CLUSTER identifies pad and wire hits from the ADC counts, applies the electronics calibration to establish pulse heights and arrival times; and associates neighboring pad hits into space points;

PATTERN identifies tracks from the set of space points and performs a first momentum fit to the tracks;

HAWIRE associates wire hits with the identified tracks;

DISTORT refines space points using wire information, applies corrections for electrostatic track distortions, and refits tracks;

DEDX computes the dE/dx for the tracks and makes identity assignments;

TRAGIC performs a final track fit to a helix, taking into account mass-dependent energy losses;

VERTEX constrains fitted tracks to a common origin for improved momentum resolution and event vertex determination.

This program sequence is carried to completion online between triggers for all $q\bar{q}$ events and at least through DISTORT for most other events. Enough events are analyzed to determine run-dependent constants (vertex position, drift speed, gas gain, electron absorbtion and diffusion) immediately upon completion of a run.

In the next analysis pass (this one offline), CLUSTER, PATTERN, and HAWIRE are executed as needed for events that had insufficient time for their execution online. Then DISTORT, DEDX, TRAGIC, and VERTEX are run again on all events using the run-averaged constants determined online. To be written to the next set of tapes ("E" tapes), events must satisfy the filters BHABHA_COUNT, STRIP_COSMIC, and TPC_SEL. STRIP_COSMIC and TPC_SEL delete cosmic rays using muon chamber and TPC information, respectively; BHABHA_COUNT counts low-angle Bhabha events for luminosity monitoring and keeps every tenth. About 65% of the raw data tape events pass these filters and are written to the E tapes. Roughly 1000 E tapes were made for the 1984–86 data.

In the same processing run E tape events are passed to the filter SELQQTAU. This filter makes loose topology cuts to select $q\bar{q}$ events and most $\tau\bar{\tau}$ events while rejecting other processes. About 17% of E tape events pass this filter and are written to "F" tapes; 193 F tapes were written for the 1984–86 data. DST records are created for the F tape events; these records are included on the F tapes and are extracted (without further selection) onto "Select DST" tapes.

The Select DSTs are processed by the analysis programs FIDUCIAL, LABEL_PAIRS, FIXDEDX, and VERTEX, which compute information relevant to the final $q\bar{q}$ selection, identify electrons from photon conversions, refine dE/dx information, and identify secondary decay vertices, respectively. A filter LABEL_HADRON_V2 passes $\sim$ 25% of the Select DST events onto the final "Hadron DSTs" (which are actually disk files). This filter makes cuts similar to, but looser than, the final TPC/2γ hadronic event selection described in Section 4.2; about 65% of the events in the Hadron DSTs are TPC/2γ good hadronic events.

Two final corrections to the data are not shown in Figure 4.1. (These corrections are made long after the creation of the original Hadron DSTs.) Final electrostatic distortion corrections are determined from two-prong events selected

from E tapes. These corrections are applied to the F tape events (starting with DISTORT and proceeding through the analysis chain as usual) to produce new F tapes, Select DSTs, and Hadron DSTs. Final dE/dx corrections are determined from the Hadron DSTs. (As of this writing, new DSTs have not yet been made using this final dE/dx correction; instead, the corrections are applied by the program FIXDEDX whenever a DST is analyzed.)

4.1.2 Particle Identification Using dE/dx

Theory of dE/dx

The ionization by a charged particle traversing the TPC gas is a function only of the speed v of the particle. (This makes the assumption that the particle's charge is plus or minus the electron charge.) Measuring the ionization thus measures the speed of the particle; combined with the measured track momentum, this establishes the particle's mass m through the relation $p = \beta\gamma m$, where $\beta = v/c$ and $\gamma = 1/\sqrt{1-\beta^2}$. The viability of this technique to establish the particle's identity depends on the ability of the TPC to characterize the ionization sufficiently accurately. (The energy loss per unit track length dE/dx is assumed to be proportional to the total ionization produced per unit track length, so that "ionization" and "energy loss" are often used equivalently.)

The primary ionization along a track comes from two physical sources, depending on the scale of the energy transfer involved. The ionization cross-section is strongly peaked at energy transfers corresponding to the binding energies of electrons in the TPC gas, so for energy transfers comparable to atomic energy levels this resonant ionization dominates. For energy transfers large compared to the atomic binding energies, the electrons in the gas are essentially free and the process is well-described by Rutherford scattering. The Rutherford scattering is "hard," resulting in energetic ionization electrons, but rare compared to the

softer resonantly produced ionization electrons.

A sense wire in the TPC collects ionization from a 4 mm thick slice of gas, corresponding to 5 mm or so of track length for a typical track. On the order of 100 primary electrons are liberated on average along each 5 mm of a typical track. This primary ionization obeys Poisson statistics, so the mean primary ionization could be determined to $\sim$ 10% per wire (neglecting avalanche fluctuations), or 1% for a track crossing the entire TPC, if only the TPC were to detect just the primary ionization. Unfortunately, the hard electrons from the Rutherford scattering (and the resonantly produced electrons from deep levels) are energetic enough to ionize the gas themselves, resulting in secondary ionization. This secondary ionization contributes greatly toward the total ionization detected, but arises from just a few hard scatters, so the statistical fluctuations ("Landau fluctuations") in the total detected ionization are large.

Simply taking the total detected ionization for a track is therefore a poor way to characterize the ionization. The TPC was designed to sample the track's ionization many times so that shape information of the resulting dE/dx distribution could be used to account for the effect of the few hard scatters. (This is why the sectors contain so many sense wires, more than are necessary for tracking.)

A detailed calculation [21] predicts the distribution of dE/dx samples from a track, which is found to be in good agreement with the data. This calculation takes into account six energy levels of methane and argon, making suitable approximations for resonant and Rutherford cross-sections; the resulting shape is a function of β and the sampled track length δx. I show both the predicted curve and the data in Figure 4.2; the salient feature is the long high energy tail ("Landau tail") resulting from the hard Rutherford scatters. It is primarily dE/dx samples drawn from this tail that cause large fluctuations in the mean dE/dx.

In principle, one could measure the dE/dx distribution for each track, then

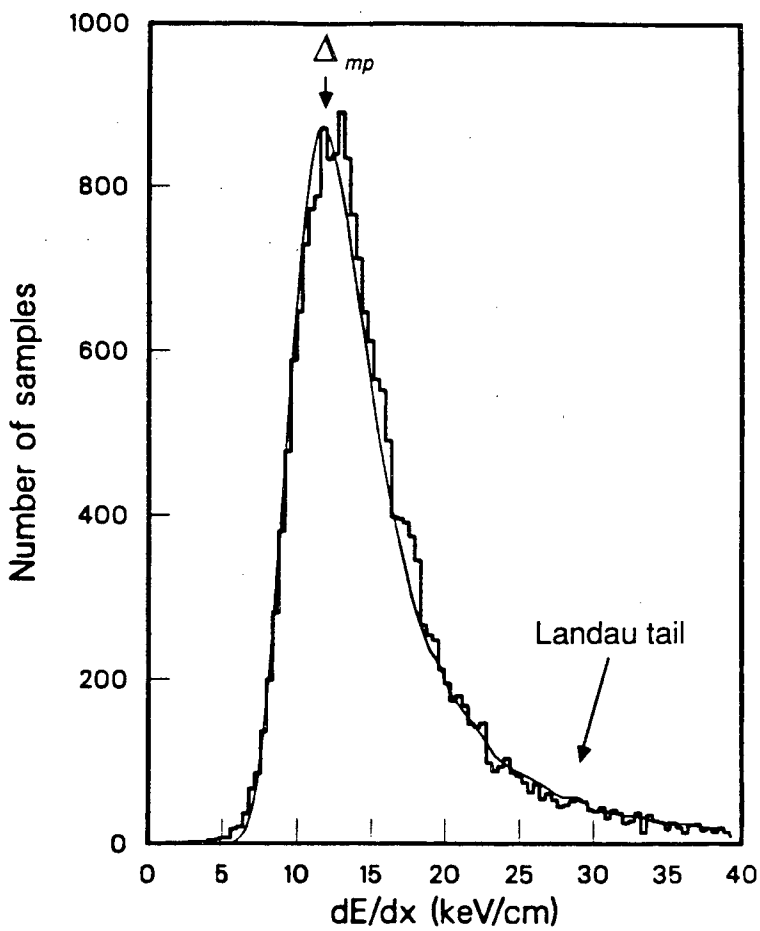

Figure 4.2: Distribution of dE/dx energy loss for 4 mm track samples for data (histogram) and as predicted by the detailed calculation (curve).

fit the predicted shape (with δx as a parameter) to establish β for each track. This would use the full dE/dx shape information, but would be very difficult to calibrate. In practice, a single, simple estimator is constructed (using dE/dx shape information in a rudimentary fashion) for each track to characterize the ionization: called the "truncated mean," it consists of the mean of the lowest 65% usable dE/dx samples. The truncated mean is what is meant in TPC parlance by *the* dE/dx value for a track. By simply throwing away the Landau tail, the truncated mean isolates and removes much of the fluctuations from the hard scatters. (It turns out that most of the particle identity information resides in the resonant ionization, so that discarding the bulk of the Rutherford information is benign.) The truncated mean is assumed to be proportional to the most probable energy loss Δ_{mp}, an assumption born out by Monte Carlo studies. The same formalism that predicted the dE/dx distribution is used to derive Δ_{mp} as a function of β, so that the dE/dx value of a track is known as a function of β. The dE/dx resolution is typically 3.4% for a track crossing the entire TPC; this yields a sufficiently accurate characterization of the ionization for the TPC to perform particle identification by simultaneous measurement of dE/dx and momentum.

The results of the calculation for Δ_{mp} are:

$$\Delta_{mp} = (\Delta_{mp})_{Rutherford} + (\Delta_{mp})_{resonance}, \tag{4.1}$$

$$(\Delta_{mp})_{Rutherford} = \sum_j \xi_j \left[\ln\left(\frac{\xi_j}{E'_j}\right) + 0.198 \right], \tag{4.2}$$

$$(\Delta_{mp})_{resonance} = \sum_{ij} \left[\delta x \left\langle \frac{dN}{dx} \right\rangle_{ij} - \frac{1}{2} \right] E'_{ij}, \tag{4.3}$$

where the sums are over energy level i of gas j, and

$$\xi_j = \frac{2\pi e^4 (\delta x) n_j}{m_e c^2 \beta^2},$$

$$n_j = \text{electron number density of gas j},$$

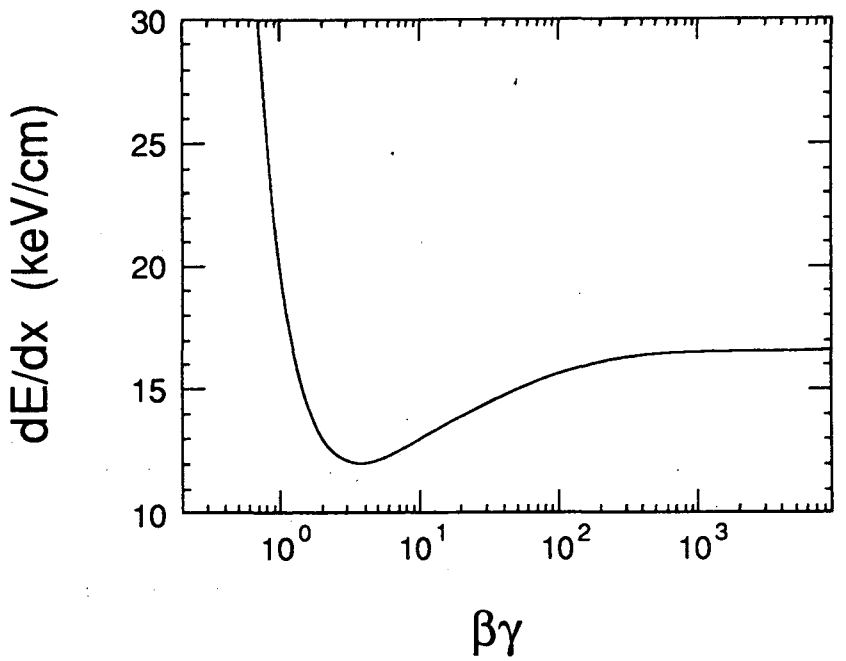

Figure 4.3: Predicted truncated mean energy loss as a function of $\beta\gamma$.

$$
\begin{aligned}
\delta x &= \text{sampled track length,} \\
E'_j &= \text{mean ionization potential for gas j,} \\
\left\langle \frac{dN}{dx} \right\rangle_{ij} &= \frac{2\pi e^4 n_j}{m_e c^2 \beta^2} \frac{w_{ij}(s_{ij}-1)}{E_{ij} s_{ij}} \\
&\quad \cdot \left[\ln\left(\frac{2 m_e c^2 \beta^2 \gamma^2}{E'_{ij} |1 + \beta^2\gamma^2(1-\epsilon(E'_{ij}))|} \right) + 1 - \beta^2 Re(\epsilon(E'_{ij})) \right], \\
E_{ij} &= \text{ionization threshold for level i of gas j,} \\
E'_{ij} &= \text{mean ionization potential for level i of gas j,} \\
\epsilon &= (\epsilon_1 + i\epsilon_2) = \text{the dielectric constant of TPC gas,}
\end{aligned}
$$

and where w_{ij} and s_{ij} are numbers parameterizing the oscillator strength of level i of gas j. This curve for dE/dx (which is equivalent to $\Delta_{mp}/\delta x$) as a function of $\beta\gamma$ is plotted in Figure 4.3.

This curve divides into four broadly defined regimes. For slow particles, dE/dx $\sim 1/\beta^2$ and the curve drops sharply with increasing $\beta\gamma$; this is the "$1/\beta^2$"

region. Around $\beta\gamma \sim 3$ the curve reaches a minimum; this is the "minimum ionizing" region. The curve rises slowly with $\beta\gamma$ up to around $\beta\gamma \sim 10^3$; this is the "relativistic rise" region. Above $\beta\gamma \sim 10^3$ the curve flattens to the "Fermi plateau." The physical interpretation of these regimes is straightforward. Ionization is heavy in the $1/\beta^2$ region because the slowly moving particle spends a lot of time near each atom, thus increasing the probability of an ionization. The relativistic rise is due to the Lorentz enhancement of the particle's transverse field, and hence its ionizing power. The Fermi plateau is the result of polarization of the medium cutting off any further relativistic rise. The minimum ionizing region is simply the cusp between two regions of heavier ionization.

Some relevant properties of $(\Delta_{mp})_{Rutherford}$ and $(\Delta_{mp})_{resonance}$ can be inspected from Equations 4.2 and 4.3. The Rutherford term has a logarithmic dependence on δx, an effect accounted for in the software before determining a track's dE/dx value. This term also saturates to a constant value above the minimum ionizing region. Both Rutherford and resonance terms exhibit the behavior of the $1/\beta^2$ region; but only the resonance term contains the behavior of the relativistic rise and the Fermi plateau. (Both the relativistic rise and the Fermi plateau are implicit in the logarithmic term of $\left\langle \frac{dN}{dx} \right\rangle_{ij}$: the argument of the logarithm increases as $\beta^2\gamma^2$ until the $\beta^2\gamma^2(1 - \epsilon(E'_{ij}))$ in the denominator dominates the 1 to cancel the $\beta\gamma$ dependence.)

Since $p = \beta\gamma m$, the dE/dx curves for particles of different mass are established by simple lateral translation in $\ln(p)$ space. This means any two curves are guaranteed to cross at one point, called a "crossover"; particle identity assignments are problematic in the vicinity of crossovers. It is worth noting that the ability of the TPC to perform particle identification above minimum ionizing regions rests in the relativistic rise inherent in the resonant ionization term.

The curve predicted by Equations 4.1, 4.2, and 4.3 is fine-tuned by a fit

to samples of unambiguously identified tracks ($1/\beta^2$ protons, minimum ionizing and relativistic rise pions, cosmic ray muons, conversion electrons, and Bhabha electrons). The resulting agreement between the theoretical curve and data is excellent; the systematic error on the theoretical curve is estimated to be 0.2%. Plotted in Figure 4.4 are data and the curves for e, μ, π, K, and p; the separation of the five species on the plot and the agreement with theory graphically demonstrate the ability of the TPC to perform particle identification.

Particle Identity χ^2

Each dE/dx curve represents an allowed locus in dE/dx vs. momentum space for particles of a given mass. Each track has its dE/dx and momentum measured, so a χ^2 can be formed to quantify consistency with a given mass hypothesis:

$$\chi_i^2 = \frac{((dE/dx)_i - (dE/dx)_{meas})^2}{\sigma_{dE/dx}^2} + \frac{(p_i - p_{meas})^2}{\sigma_p^2}. \tag{4.4}$$

In this expression, i stands for any of the five stable species e, μ, π, K, p. Pairs of $(dE/dx)_i$ and p_i are taken on the dE/dx curve for species i, stepping along the curve until χ_i^2 is minimized; this minimum value is the χ_i^2 for that measured track and that species hypothesis i. The dE/dx resolution $\sigma_{dE/dx}$ is parameterized as a function of polar angle and number of dE/dx samples; the momentum resolution σ_p is the quoted error from the TRAGIC fit.

Particle Identity Probability

The χ_i^2 information can stand on its own, or it can be supplemented by prior knowledge to arrive at probability assignments. The prior information used in TPC hadronic analysis is the knowledge of particle fractions in the hadronic event sample as a function of momentum. Thus for example, a particle observed at the K/π crossover will be identified as a π, since pions outnumber kaons by

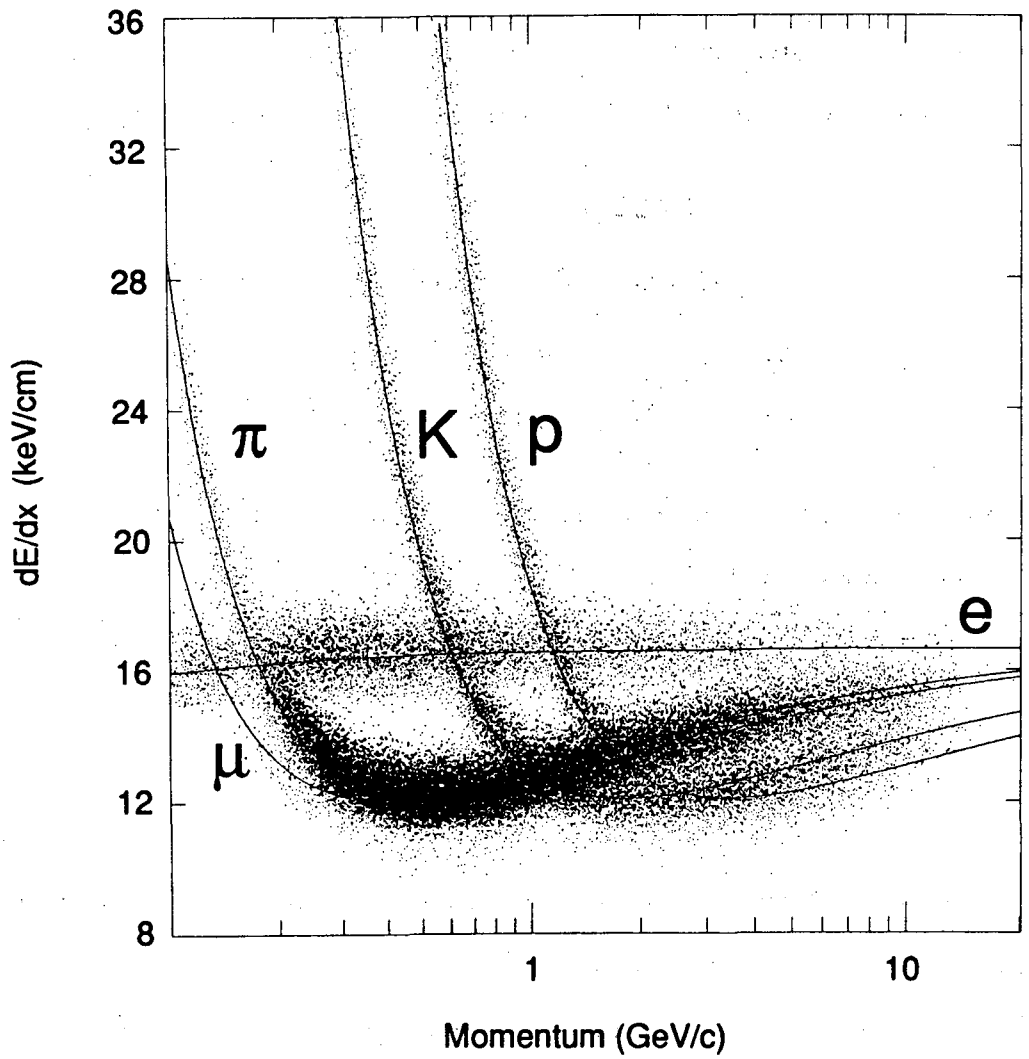

Figure 4.4: Measured dE/dx of tracks with at least 80 dE/dx samples, as a function of momentum. Also shown are the predicted curves for e, μ, π, K, and p.

about 8 to 1 at that momentum. Using the particle fractions, the probability P_i of a track being species i is given by

$$P_i = \frac{f_i(p)\exp^{-\chi_i^2/2}}{\sum_{j=1}^{4} P_j} \tag{4.5}$$

where $f_i(p)$ is the fraction of tracks of momentum p that are species i. The denominator simply normalizes the sum of probabilities to unity. The particle fractions measured by the TPC/2γ Collaboration are parameterized by

$$\begin{aligned} f_e &= (0.2/p)^2 \\ f_\pi &= max(0.8494 - 0.1350\ln(p), 0) \\ f_K &= max(0.1093 + 0.0916\ln(p), 0) \\ f_p &= max(0.0413 + 0.0434\ln(p), 0) \end{aligned}$$

where the momentum p is measured in GeV/c. Since muons are a small component of hadronic events they are not included in this procedure.

4.2 Event Selection

Annihilation events $e^+e^- \rightarrow q\bar{q}$ are characterized by large multiplicities, large detected energy, and low Lorentz boost with respect to the laboratory frame. The standard TPC/2γ selection for these events capitalizes on these features, using charged tracks detected in the TPC to make the selection.

To be used in making the selection, a track must satisfy these conditions:

1. the polar angle with respect to the beam direction must be $> 30°$;

2. either the curvature error dC must be < 0.30 GeV^{-1} or the fractional curvature error dC/C must be < 0.30;

3. the momentum of the track in the TPC volume must be > 100 MeV/c;

4. the momentum of the track extrapolated to the vertex (correcting for energy loss) must be > 120 MeV/c; and

5. the track must extrapolate to within 6 cm of the nominal vertex in the x-y plane and within 10 cm in z.

Criterion (1) ensures that the track is well within the fiducial volume of the TPC; criterion (2) rejects tracks with poorly measured momenta; criteria (3) and (4) reject tracks too soft to have made it into the TPC from the interaction point, and criterion (5) requires the track to be consistent with originating at the interaction point, thereby rejecting many cosmic rays and tracks originating in nuclear interactions in the beampipe and beam-gas collisions. A track satisfying these conditions is called a "good track."

To be considered a good hadronic annihilation event, an event must satisfy these conditions:

1. there must be at least five good non-electron tracks, where electron identification is done either by dE/dx or by geometric reconstruction of photon conversions;

2. the total energy of the charged good tracks, E_{ch}, must be > 7.25 GeV;

3. the longitudinal momentum balance of good tracks must satisfy $|\Sigma p_z| < 0.4E_{ch}$;

4. at least half the tracks of the event must be good tracks;

5. the reconstructed vertex of the event must be within 2 cm of the nominal vertex in the x-y plane and within 3.5 cm in z; and

6. at least one event hemisphere (defined by the sphericity axis of the event) must contain either at least four charged non-electron good tracks or an invariant mass of at least 2 GeV.

Criterion (1) eliminates low multiplicity events and Bhabha events where one of the particles showered heading into the TPC; criteria (2) and (3) discriminate against two-photon and beam-gas events; criterion (3) also discriminates against $q\bar{q}$ events with energetic initial state radiation; criterion (4) eliminates problematic cases; criterion (5) suppresses beam-gas events; and criterion (6) discriminates against $\tau\bar{\tau}$ events. Monte Carlo studies estimate the contamination of these good hadronic annihilation events (taking into account the relative cross-sections) to be $(0.4 \pm 0.1)\%$ from $\tau\bar{\tau}$ events, $(0.5 \pm 0.1)\%$ from two-photon events, and $< 0.1\%$ from beam-gas and Bhabha events. About 78% [67%] of generated Monte Carlo hadronic annihilation events satisfy the hadronic event selection when generated without [with] initial state radiation. (Direct interpretation of the acceptance for events generated with initial state radiation is difficult, for it depends on the details of the initial state radiation high energy cutoff. This does not affect the analysis, for events with energetic initial state radiation do not pass the hadronic selection anyway; data and Monte Carlo need not agree in this regime.)

In addition to the standard TPC/2γ hadronic event selection, I require an event to satisfy two more requirements:

- the sphericity axis of the event must lie $> 45°$ away from the beam direction, and
- the sphericity value must be < 0.5.

These criteria ensure that the bulk of the event is contained within the TPC fiducial volume and that the orientation of the sphericity axis is meaningful when used in my subsequent analysis.

The data used in this dissertation were collected during the 1984–86 running cycles of the detector. Data corresponding to an integrated luminosity of

$\sim$ 68 pb^{-1} [43] were collected, resulting in 25782 events passing the standard TPC/2γ hadronic event selection, of which 20089 pass my additional sphericity cuts. These 20089 events form the data set on which I perform the measurements of this dissertation.

4.3 Detector Simulation

The operation of a modern High Energy Physics detector is sufficiently complicated that the only way to understand its performance in detail is through a detector simulation Monte Carlo program. Such a program propagates an event through the elements of a detector using a random number generator to reproduce the relevant stochastic physical processes experienced by the real events in the detection process. This produces simulated data useful for estimating detector acceptances, estimating backgrounds, honing one's analysis techniques, and studying systematic errors.

The TPC/2γ collaboration has two detector simulation Monte Carlos available: the Global Monte Carlo (GMC) and the Fast Monte Carlo (FMC). The GMC generates simulated raw data which is then passed through the complete data analysis chain for detailed investigation of detector performance. It is too slow, however, to provide the high statistics simulated data usually necessary in an analysis. The FMC trades exactitude for speed, essentially picking up the analysis chain partway through, generating derived quantities such as the dE/dx for a track from a distribution instead of generating the individual wire hits. For many purposes, the FMC is accurate enough. The portion of the FMC that simulates the TPC is called TPCLUND; it is the only relevant detector simulation for my analysis so I sketch its operation here. It takes $\sim$ 1.5 sec of VAX 8650 CPU time for TPCLUND to simulate an hadronic annihilation event (compared to $\sim$ 30 msec for the physics generator to produce the interaction itself).

TPCLUND takes as input the buffer of particle species and momenta generated by a physics generator; initial state radiation is simulated using the program of Berends and Kleiss [44]. The TPC and material between it and the interaction point are modelled as concentric layers, each characterized by a location, an interaction length, and a radiation length. The beampipe, pressure wall, IDC, inner field cage, and each TPC pad row constitute layers. Particles interact with each layer in turn, the results of these interactions being propagated to the next layer. Neutral particles can decay and undergo nuclear interactions; photons can convert. Charged particles can decay, undergo nuclear interactions, emit bremsstrahlung, undergo Coulomb multiple scattering, and experience dE/dx energy loss.

The event vertex is smeared about its nominal value by the beam spot size. TPC space points are generated where each charged track crosses a pad row, then smeared by resolutions parameterized according to track angle and other variables. The resulting space points are assigned to tracks; points can be lost from tracks due to geometric losses and ambiguous track assignments, but are never assigned to the wrong track. A track with three or more associated points is considered found, otherwise the track is lost. A fit is then performed to the space points to establish the measured track momentum; this fit is not the same as the TRAGIC fit used for real data, but is sufficiently similar for most purposes.

The number of usable dE/dx samples is chosen, which along with the polar angle of the track defines the dE/dx resolution expected for that track. The dE/dx value for the particle species and momentum is smeared by this resolution to arrive at the simulated dE/dx measurement.

A true vertex constrained fit is not performed in TPCLUND. Instead, χ^2s for vertex consistency are selected for tracks in a quick fashion to roughly reproduce the results of VERTEX.

Sets of tapes of simulated data DSTs are produced using the FMC. A given set has $\sim$ 80,000 good hadronic events, or about four times the data set. Statistical errors when using Monte Carlo tapes are therefore small compared to the data set.

The performance of TPCLUND has been checked by comparing a variety of experimental distributions (such as track curvature error, number of dE/dx samples per track, vertex impact parameter, etc.) with the predictions of the detector simulation. These comparisons have been made in the course of several analysis projects, including this one. TPCLUND generally does quite well. (One exception is that the χ^2 for vertex consistency is untrustworthy, so I avoid using it.) At the points where an analysis in this thesis depends on TPCLUND, I estimate the reliability of the detector simulation and the corresponding systematic errors incurred by its role in the analysis.

Chapter 5

Measurement of the ρ^0 Differential Cross-section

5.1 Overview

The ρ^0 is a broad resonance ($\Gamma = 153$ MeV, M $= 770$ MeV) which decays almost exclusively to $\pi^+\pi^-$ ($\simeq 100\%$ branching fraction). These seemingly innocent facts conspire to make the ρ^0 a surprisingly hard particle to measure. The exclusive decay mode means the only accessible signature of a ρ^0 in this experiment is as a feature in the $\pi^+\pi^-$ invariant mass spectrum; the fact that pions are by far the most copiously produced particles in the hadronization process and ensuing decays means that this $\pi^+\pi^-$ mass spectrum has a large background in and near the ρ^0 mass region. The sizable width of the ρ^0 means that the measured area of the spectrum belonging to the ρ^0 peak is subject to a large systematic error from uncertainty of the background underlying the ρ^0.

The nature of the background in the mass spectrum is complicated by the fact that there are two contributions to it. The largest contribution to the background is from the many mass pairings possible from the large number of candidate tracks; this combinatoric background is large but smooth. Also entering into the mass plot are particle pairings that stem from the decay of a particle other than the ρ^0; these pairings are fewer in number but give structure to the spectrum.

The analysis technique I use to measure the ρ^0 cross-section is suggested in part by the foregoing considerations. Also relevant to my final choice of analysis technique is the observation that neither the Lund nor Webber Monte Carlo packages (including detector simulation) adequately reproduce the observed dipion mass spectrum. This effect can be seen in Figure 5.1, where I present the unlike-sign and like-sign dipion spectra ($M(\pi^+\pi^-)$ and $M(\pi^\pm\pi^\pm)$) for $x < .10$ and for $x > .10$, along with the Lund prediction (normalized to the same number of analyzed events). (These spectra are prepared as described in the next section.) I also present the result of subtracting the like-sign spectra from the unlike-sign spectra. I investigated the source of the disagreement between data and Monte Carlo extensively but without success. As I explain in the next section, the Monte Carlos play a central role in this analysis; since I am unable to understand or eliminate this mass discrepancy, my analysis must minimize its effect. Noting that this discrepancy appears roughly equally in the like-sign and unlike-sign mass spectra and therefore largely cancels when subtracting the former from the latter, I employ a spectrum subtraction technique in part to cancel remaining discrepancies between Monte Carlo and data. The remaining discrepancy after this subtraction is a strong function of x. The effect is that at low x the data shows an excess in the subtracted spectra in the mass region between the ρ^0 and the K_s, an excess that diminishes rapidly with increasing x (see Figure 5.1). Because of this discrepancy, I choose not to attempt measurements for $x < .10$ since the background is not well understood; for $x > .10$ I consider the discrepancy when assigning systematic errors.

As a final consideration in selecting an analysis technique, having no compelling reason for trusting one generator and rejecting the other, I adopt the philosophy that both Lund and Webber give equally reliable predictions of the underlying physical truth. That is, when measuring the ρ^0 cross-section I in-

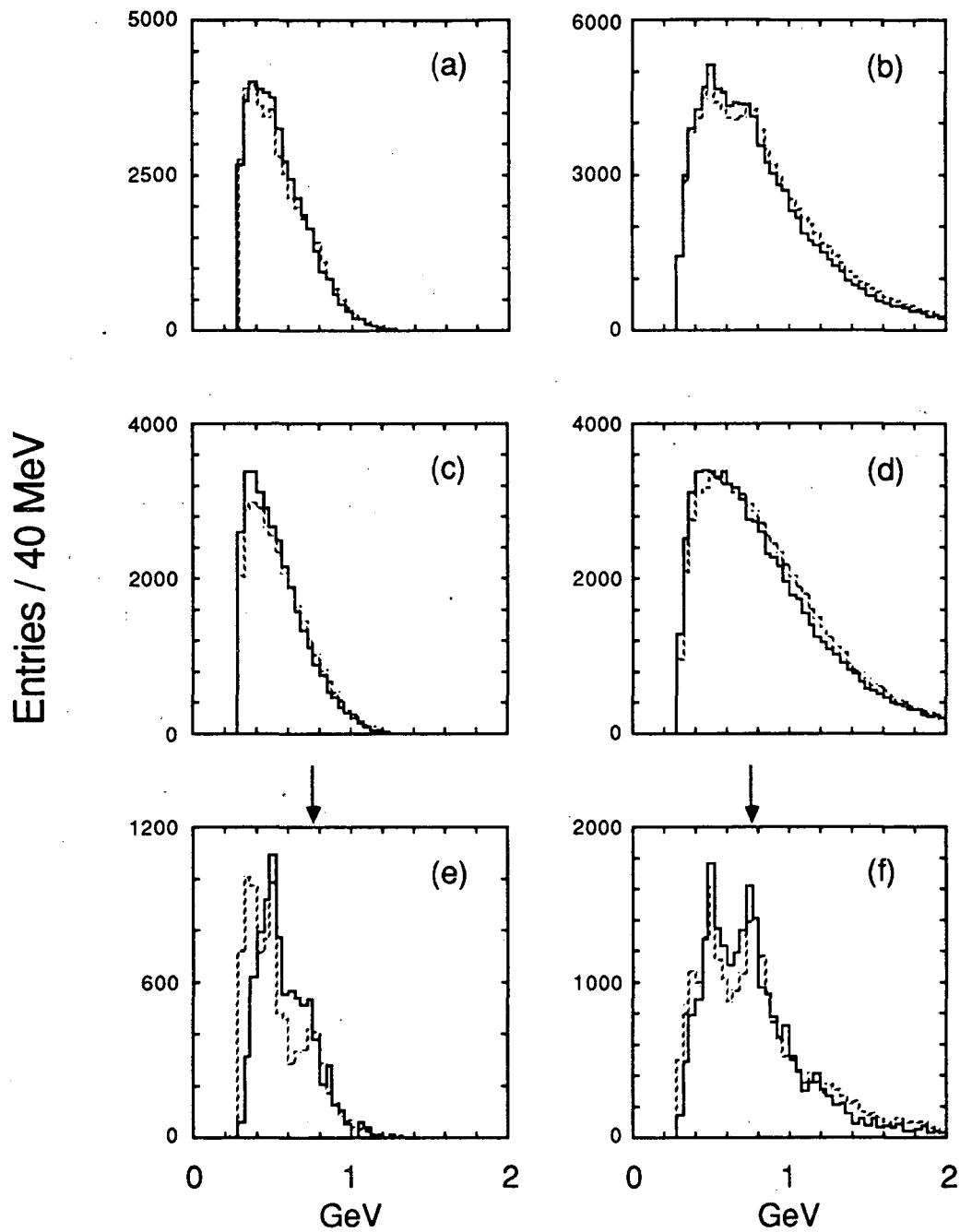

Figure 5.1: Dipion mass spectra for data (solid lines) and the predictions of the Lund Monte Carlo (dashed lines). These spectra are prepared in the manner described in Section 5.2. The Monte Carlo spectra are normalized to the same number of analyzed events as in the data. (a) Unlike-sign spectrum M($\pi^+\pi^-$) for $x < .10$. (b) Unlike-sign spectrum for $x > .10$. (c) Like-sign spectrum M($\pi^\pm\pi^\pm$) for $x < .10$. (d) Like-sign spectrum for $x > .10$. (e) Subtracted spectrum M($\pi^+\pi^-$) - M($\pi^\pm\pi^\pm$) for $x < .10$. (f) Subtracted spectrum for $x > .10$. The arrows in (e) and (f) indicate the central ρ^0 mass.

dependently use both Monte Carlos in turn and average the results; when appropriate in estimating systematic errors, I assume disagreements between the two Monte Carlos are representative of the disagreements between either Monte Carlo and physical reality.

I have presented the general context of the ρ^0 analysis in this section. In Section 5.2, I explain the method I've chosen for this analysis and present the results (with statistical errors only) for the cross-section. I estimate the systematic errors of my analysis in Section 5.3. I present final results and errors in Section 5.4, as well as comparisons with the predictions of the generators and the measurements from other experiments.

5.2 Basic Method

In order to measure $\frac{1}{\beta\sigma_H}\frac{d\sigma}{dx}$ (as described in Chapter 1), I divide the data and Monte Carlo mass spectra into six x bins for $x > .10$, and measure the area in the ρ^0 peak independently in each bin. The x bins are chosen to be wide compared to the x resolution of the detector, to have comparable statistical significance of the ρ^0 in each bin, and to give the finest granularity at low x where the background shape changes rapidly as a function of x. The specific x bins I use are given in Table 5.3.

5.2.1 Formation of the Mass Spectra

To be used in this analysis, an event must first pass the multihadronic event selection and sphericity requirements described in Section 4.2. An event passing these cuts is called a "good event."

For a track to be used in forming the mass spectra, it must pass a set of cuts tighter than that used in choosing good events. Tracks that pass these cuts are called "good tracks." For a track to be considered good, it must

1. have a measured dE/dx and have been fit to a helix by the program TRAGIC,

2. satisfy $dp_\perp/p_\perp < .05$ (if $p_\perp < 1$ GeV/c) or $dp_\perp/p_\perp^2 < .05$ (if $p_\perp > 1$ GeV/c), where $p_\perp$ is the momentum transverse to the beam axis and $dp_\perp$ is its error,

3. have momentum (extrapolated to the event vertex) > 150 MeV/c,

4. have momentum (extrapolated to the event vertex) < 14.5 GeV/c,

5. point in a direction more than 30° away from the beam axis,

6. extrapolate to within 1 cm of the measured event vertex in both the bending plane and in the beam direction,

7. have at least 30 wires used in measuring dE/dx,

8. have a particle-id χ^2 for the pion hypothesis < 9, and

9. have a probability for being a pion (measured using the algorithm explained at the end of Section 4.1.2) > 0.5.

Cuts (1) and (4) reject meaningless tracks. Cut (2) rejects tracks with poorly measured momenta. Cut (3) eliminates tracks in a momentum region of large energy loss and uncertain acceptance. Cut (5) rejects tracks at grazing angles to the material in front of the TPC, which are subject to large multiple scattering and uncertain acceptance. Cut (6) helps eliminate tracks that originate in processes other than the primary interaction and ensuing strong decays: these processes are beam-gas interactions, cosmic ray coincidences, nuclear interactions in the material in front of the TPC, photons converting to electrons (should the electrons be misidentified as pions), and weak decays (most notably $K_s \rightarrow \pi^+\pi^-$ decay). Cut (7) requires the track to have a well-measured dE/dx for purposes

cut number	% of remaining tracks cut at each stage	
	(+) charge	(-) charge
(1)	14	12
(2)	3	2
(3)	4	4
(4)	<1	<1
(5)	2	2
(6)	25	22
(7)	14	14
(8)	15	15
(9)	5	5
Total	59	56

Table 5.1: Percent of tracks in the data cut by single-track selection.

of pion identification; cuts (8) and (9) are the pion identification cuts. The percentages rejected at each stage of tracks surviving the previous cut are given in Table 5.1; the cuts are illustrated in Figure 5.2. (Hadronic interactions in the TPC material preferentially introduce extra positive tracks into the event that are screened out by these cuts; this is why slightly more positive tracks are eliminated than negative tracks.) Overall, these cuts reduce the number of admissible unlike-sign (like-sign) pairings in the data (relative to all detected pairs) by 81.3% (82.9%). The pion purity and acceptance of the good track sample as estimated from the Monte Carlo are plotted in Figure 5.3. The purity is the fraction of the good tracks that are actually pions; the acceptance is the fraction of pions generated in good events that are called good tracks. Integrated over all momentum, the purity is 93% and the acceptance is 59%.

For a pair of tracks to have its mass entered into the mass spectrum, each track must be a good track. In addition, the following track-pair requirements

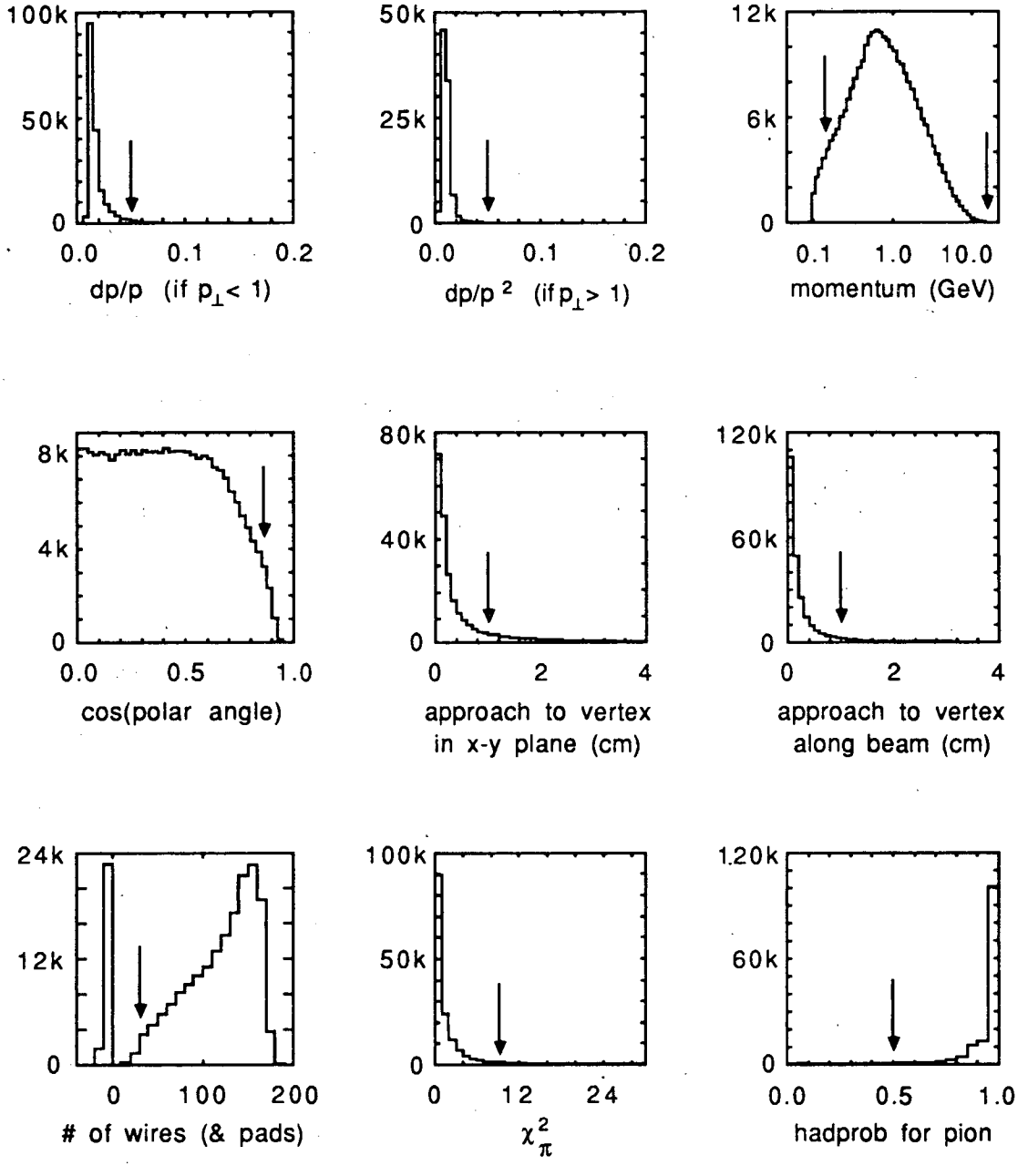

Figure 5.2: Selection of good tracks. The arrows indicate the cuts used in this analysis. Only those tracks surviving all previous cuts enter the plot for the indicated quantity. The "k" in the vertical scales stands for units of 1000. The number of pads used for dE/dx by tracks not using wire information are displayed, shifted by 20 to the left, on the "# of wires" plot.

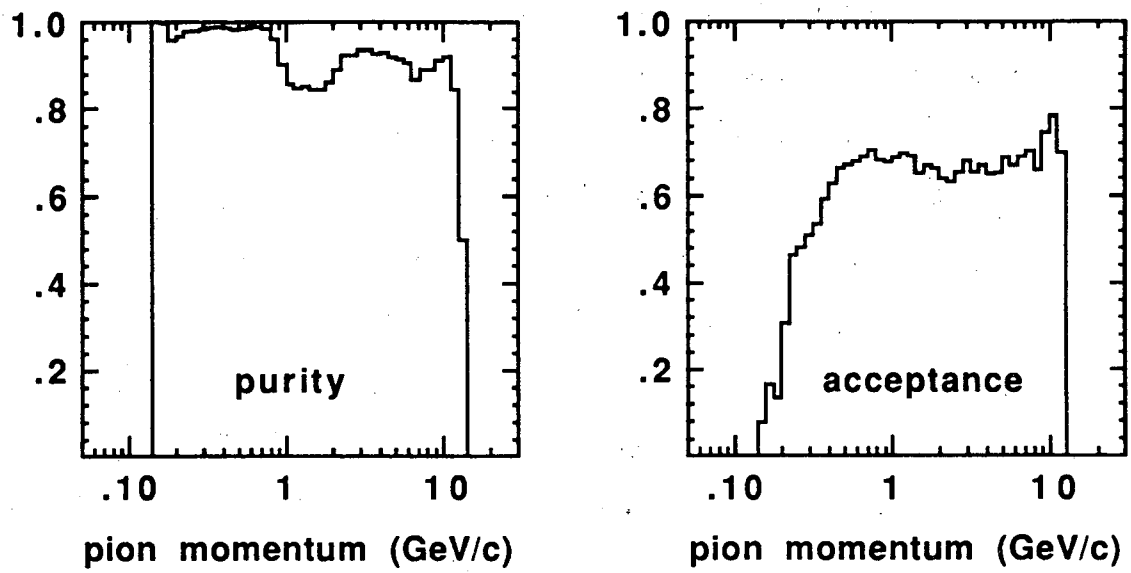

Figure 5.3: Purity and acceptance of pions in the set of good tracks. The dip in purity around 1 GeV/c is due to the K/π crossover.

are imposed:

- both tracks must lie on the same side of the event midplane, defined to be the plane passing through the event vertex perpendicular to the sphericity axis;
- the vector sum of the momenta of the two tracks must point in a direction more than 30° away from the beam axis.

The first requirement is to reduce the combinatoric background underlying the ρ^0. It is only relevant for $x \lesssim .15$; for higher x, any pair lying on opposite sides of the event midplane has an invariant mass well above the ρ^0 mass region. This cut eliminates 47.3% (52.3%) of the remaining unlike-sign (like-sign) pairs. The second cut is to prevent distortion of the ρ^0 line shape: pairs, formed of tracks lying outside a 30° half-angle cone about the beampipe, whose resultant momentum lie within this cone have masses biased high because small opening angles are excluded. In conjunction with the first track-pair cut and the event

selection requiring the sphericity axis to point > 45° away from the beampipe, this second track-pair cut turns out to eliminate only 1% of the remaining pairs.

The invariant masses of track pairs surviving all the above selection passes form the mass spectra from which I will extract the ρ^0 signal. These spectra from the data, divided into x bins, are histogrammed in 40 MeV bins in Figure 5.4. Both unlike-sign (M($\pi^+\pi^-$)) and like-sign (M($\pi^\pm\pi^\pm$)) spectra are presented. The lack of a feature at the ρ^0 mass in the like-sign combinations, and the presence of a feature at the ρ^0 mass consistent with the ρ^0 width in the unlike-sign spectra, is evidence that I truly am observing the ρ^0 signal. The acceptance of ρ^0s into these spectra as estimated from the Monte Carlo is plotted in Figure 5.5; acceptance is the fraction of ρ^0s generated in good events which have daughter pions passing all cuts. The overall ρ^0 acceptance for $x > .10$ is 45.9%.

5.2.2 Extracting the Cross-section

To extract the ρ^0 signal from the data mass spectrum in a given x bin, I employ two distinct but similar methods. In the first method, I subtract the like-sign spectrum from the unlike-sign spectrum. This reduces the combinatoric contribution and cancels or reduces some resonant contributions to the background under the ρ^0 without diluting the ρ^0 itself. The discrepancy in the mass spectra between the data and the Monte Carlo prediction, occurring as it does in both like-sign and unlike-sign combinations, is also largely cancelled. These subtracted spectra are shown for the data in 40 MeV bins in Figure 5.6.

To estimate the residual background under the ρ^0 after subtraction, I use the identically prepared like-sign-subtracted-from-unlike-sign spectra from the Monte Carlo, after first removing pairings from the same ρ^0 and from the same K^{*0}. (That is, I remove the ρ^0 and the K^{*0} peaks from the Monte Carlo spectra. The K^{*0} peak stems from the $K^{*0}\rightarrow K^+\pi^-$ (+ c.c.) decay, with the K^+ misidentified

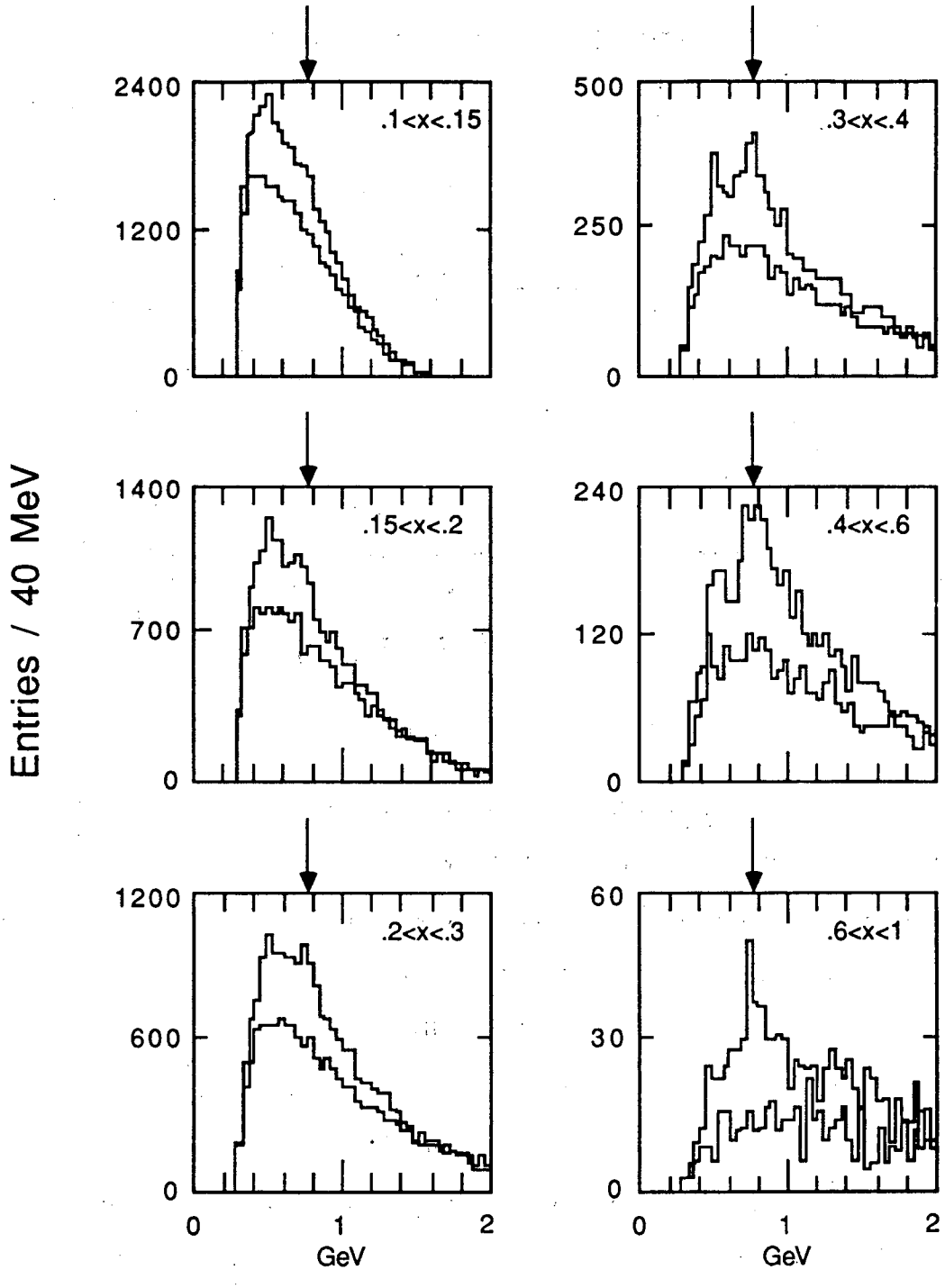

Figure 5.4: Unlike-sign and like-sign dipion mass spectra in the data, divided into x bins. The arrows indicate the central ρ^0 mass. The like-sign spectra have fewer entries than the unlike-sign spectra in each case.

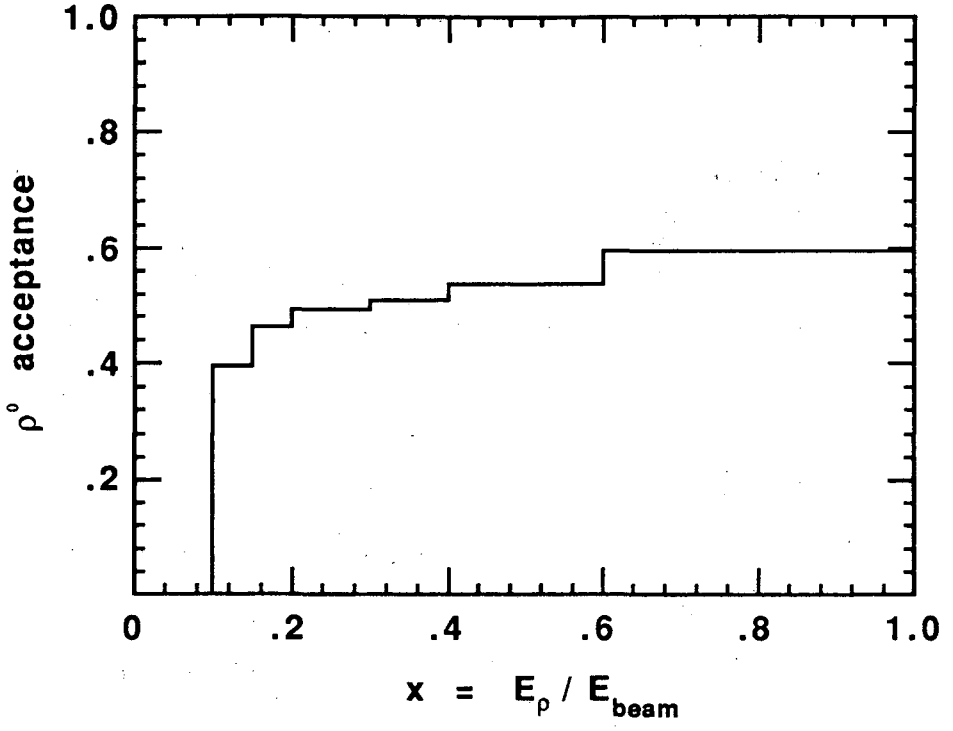

Figure 5.5: ρ^0 acceptance in each x bin.

as a π^+; this is reconstructed as a broad peak lying slightly below the ρ^0, and is the only significant resonant background structure remaining in the relevant mass region after the subtraction of the spectra.) I then perform a least-squares fit to the data summing three contributions: a curve fixed in shape and magnitude to account for the K^{*0}, a P-wave Breit-Wigner line (PWBW) fixed in shape but free to float in magnitude to account for the ρ^0, and the aforementioned Monte Carlo histogram floating in magnitude to account for everything else but the ρ^0 and the K^{*0}. There are thus two free parameters in this fit: the normalizations of the background and the ρ^0.

The K^{*0} shape and magnitude are fixed from Monte Carlo predictions; the exact line shape is hard to predict analytically, for the curve that appears as a pure PWBW in the $K^{\pm}\pi^{\mp}$ spectrum gets distorted under the misassignment of the pion mass to the kaon. Empirically, an S-wave Breit-Wigner (SWBW) with

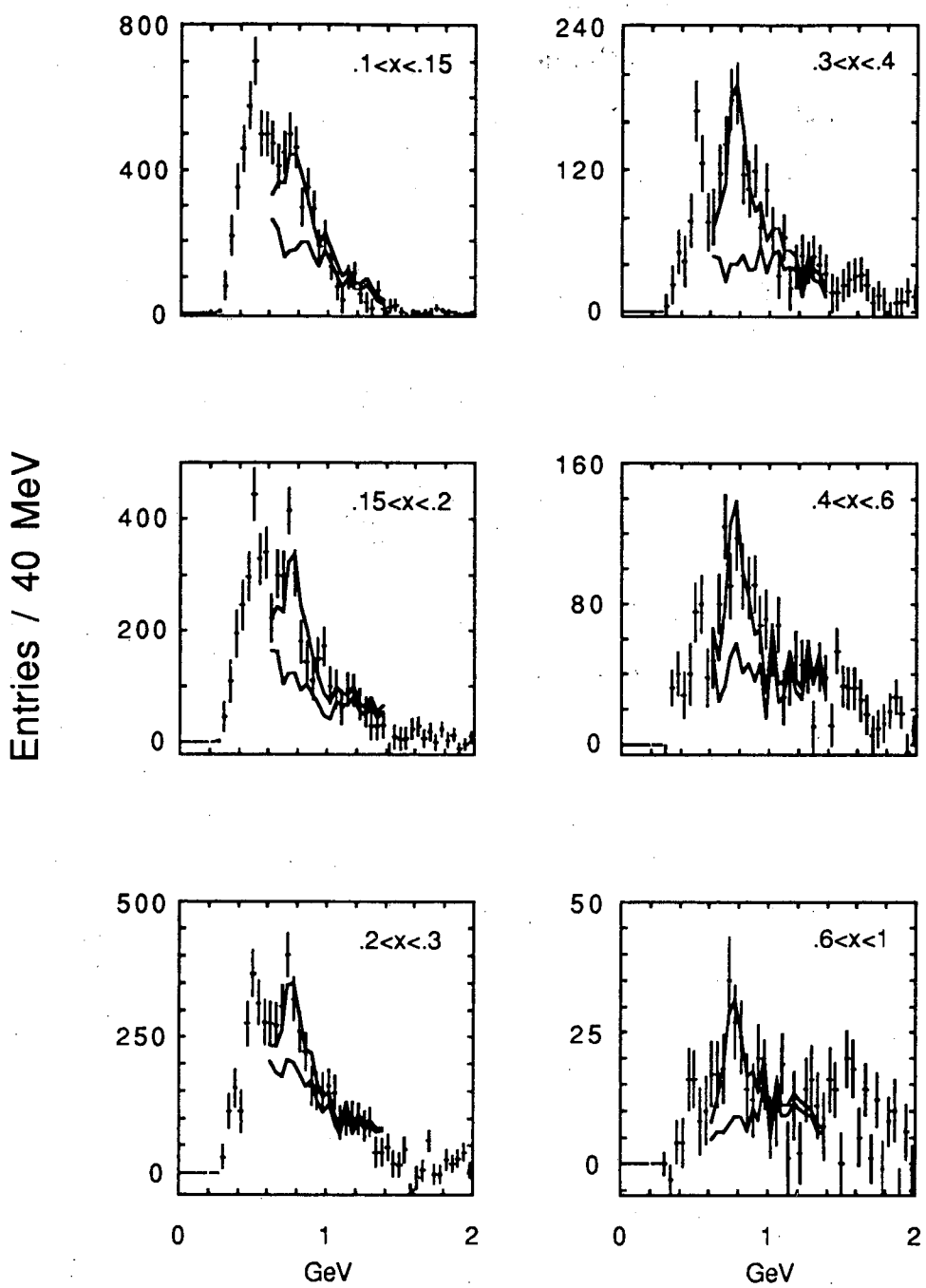

Figure 5.6: Unlike-sign dipion mass spectra in the data with like-sign mass spectra subtracted, divided into x bins. Also shown are the results of a fit (as described in the text) using the Lund Monte Carlo for background: the upper curve gives the total fit, the lower curve is the Monte Carlo background contribution. While the backgrounds look jagged to the eye, statistically they are smooth compared to the data because the Monte Carlo sample size is four times larger.

mass and width in each x bin suitably chosen was found to fit the Monte Carlo K^{*0} contributions to the detected spectra with good χ^2s. I used this SWBW with magnitude fixed from the Monte Carlo prediction. The systematic error from the K^{*0} contribution proves to be small, so the details of the K^{*0} treatment are not important.

The PWBW used for the ρ^0 is given by

$$N(m)dm = \mathrm{N}_\rho \left(\frac{2}{\pi}\right) \frac{mM_0\Gamma}{(m^2 - {M_0}^2)^2 + {M_0}^2\Gamma^2} dm \tag{5.1}$$

with

$$\Gamma = \Gamma_0 \left(\frac{q}{q_0}\right)^3 \frac{M_0}{m}$$

as suggested by Jackson [45]. In these equations, $N(m)dm$ is the expected number of ρ^0s in a mass bin of width dm centered on mass m; M_0 and Γ_0 are the "table value" mass and width; q is the three-momentum magnitude of the decay products in the parent's rest frame; q_0 is the three-momentum magnitude of the decay products in the rest frame if the parent has $m = M_0$; and N_ρ is the overall normalization (that is, the number of ρ^0s present). Fixing $M_0 = 771$ MeV and $\Gamma_0 = 154$ MeV gives good fits to the Monte Carlo ρ^0 shape, including detector acceptance and resolution, for all $x \geq .10$. The normalization N_ρ is the only ρ^0 parameter allowed to vary when fitting the data.

When using the Lund package for the Monte Carlo, I perform the fits in the mass ranges .6–1.2 GeV and .6–1.4 GeV, and average the results. When using the Webber package for the Monte Carlo, I fit only in the mass range .6–1.2 GeV. This is because the Webber Monte Carlo includes the f tensor meson at 1270 MeV with the unphysical width $\Gamma = 0$; this unphysical feature in the simulated $\pi^+\pi^-$spectrum prohibits its use in the .6–1.4 GeV window. (I conclude later that the fits are insensitive to the fit range used, so this difference between the Lund and Webber fits is irrelevant.)

The second algorithm I use to fit the ρ^0 peak is quite similar to the first method. The only difference is that I scale up the like-sign spectrum before subtracting it from the unlike-sign spectrum. The scale factor used is different for each x bin. The motivation for this method is the observation in the Monte Carlo that the combinatoric contributions to the same-sign and opposite-sign spectra (that is, pairings not belonging to the same decay tree) are nearly identical in shape, differing only in magnitude. The difference in magnitude is simply because there are more unlike-sign pairings possible than like-sign; the difference is typically 10% over most x. This means that a straight subtraction of like-sign from unlike-sign spectra leaves on the order of 10% of the combinatoric background residual under the ρ^0; one might achieve better signal-to-noise by eliminating this background entirely. The scaling of the like-sign spectra is an attempt to eliminate this residual background by using the combinatoric portion of the like-sign spectra to cancel the combinatoric portion of the unlike-sign spectra.

To get the proper scale factor in a given x bin, an approximate solution is the ratio of the areas in the unlike- and like-sign spectra of the data in a control region away from the ρ^0 and other resonant structures. If the spectra were entirely combinatoric in origin in this control region, this approximate solution would be the *exact* solution for the scale factor; to the extent that the spectra are not entirely combinatoric in origin, the scale factor desired to cancel the combinatoric contributions will differ from this approximate solution. A correction to the approximate scale factor is determined from the Monte Carlo as that multiplicative constant needed to adjust the approximate solution to the desired scale factor in the Monte Carlo. I then multiply the data-determined approximate scale factor by this correction to arrive at the final factor used in scaling the like-sign spectrum. This technique keeps the Monte Carlo influence on the scale factor

as small as possible; this Monte Carlo correction factor differs from unity by typically 2%. When using the Lund (Webber) Monte Carlo for backgrounds and acceptances, I use the correction factor as determined using the Lund (Webber) package.

The final differential cross-sections are computed using the fits from both methods, each using both Monte Carlos in turn, for a total of four different measurements in each x bin. The results of the four methods are reasonably consistent, although the straight-subtraction technique gives cross-sections systematically slightly lower than those computed from the scaled-subtraction technique, and use of the Webber Monte Carlo gives cross-sections systematically slightly lower than those computed using the Lund Monte Carlo. Not having any compelling reason to trust any of the four methods over the others, I take as my final answer the average of the four measurements, weighted by the inverse square of the statistical errors. As the measurements are all performed on the same data set, the statistical errors are mutually comparable and the results are not independent; I therefore quote a statistical error that is simply an average of the four individual errors. The results of the four individual fits are given in Table 5.2.

The goodness of these fits is reasonable. When fitting in the mass range .6–1.2 GeV, for example, the average χ^2 per degree of freedom over all x bins and all four fitting methods is 1.3 for 13 degrees of freedom. I can assign the role of "data" to a Monte Carlo and use my analysis technique to measure N_ρ for this Monte Carlo; comparing this measured N_ρ to its known value, I saw no obvious correlation between goodness-of-fit and the accuracy of the ρ^0 measurement. I therefore accept all the fits regardless of χ^2, even though the goodness-of-fit overall is slightly worse than one expects when modeling backgrounds perfectly.

In calculating $\frac{1}{\beta\sigma_H}\frac{d\sigma}{dx}$ from the observed number of ρ^0s, I follow the prescrip-

tion of Equation 1.2. To get the total statistical error on the cross-section I add in quadrature the statistical errors of the ρ^0 fit in the data, the statistical error of the ρ^0s accepted into the Monte Carlo $\pi^+\pi^-$spectrum, and the statistical error of the ρ^0s generated in events without initial state radiation; this resulting statistical error is dominated by the error in the fit to the data. (Statistical errors in this thesis are always standard deviations.) I choose β evaluated from the Monte Carlos, as described in detail later. The final results for $\frac{1}{\beta\sigma_H}\frac{d\sigma}{dx}$ are given in Table 5.3.

The Webber Monte Carlo introduces a complication to this analysis all its own. Webber clusters decaying directly into $\pi^+\pi^-$ introduce a feature at the cluster mass into the unlike-sign dipion spectra: the cluster is effectively a broad "resonance." As it happens, the Webber version used in this analysis yields this cluster peak with a mass and width comparable to the ρ^0. Luckily, this effect is small except at high x; to the extent it contributes, however, it is a dangerous background that might or might not be present in the data. And if a cluster-like feature is present, it might or might not have the shape and magnitude predicted by Webber: the shape depends on details of the event generation, and the magnitude depends on Webber's particular choice of decay *Ansatz*.

I handle this uncertainty in the background in the following manner. Every fit to the data using the Webber Monte Carlo for the background is actually performed twice. I measure the ρ^0 first using the Webber spectrum "as is." I then remove the $\pi^+\pi^-$ pairs stemming directly from cluster decay, scale the remaining Webber spectrum up to have the same total number of entries, and then refit. I average the two fits to arrive at the number of ρ^0s I quote as having fit in that bin; I use this single number as "the" Webber measurement in the subsequent analysis. In the estimation of systematic errors I include an error for the uncertainty of this cluster effect. The philosophy here is that Webber "as is" probably overestimates

the cluster feature (since the feature is enhanced by artificial thresholds in the generation); to remove the feature entirely underestimates it (if it exists). Thus an average of these two extremes is as reasonable a guess as to its effect as any; the quoted systematic error quantifies the degree of guesswork.

In any procedure involving as many fits as mine, there are bound to be a few special cases to be dealt with; this analysis has two instances to mention, each involving a best-fit N_ρ converging to an (unphysical) negative value. The first case involves $N_\rho<0$ for $.2 < x < .3$ using the Lund Monte Carlo and the scaled-up like-sign spectrum technique. I include this measurement in the average quoted for that bin, ignoring the fact that it represents a measurement of a physically impossible value. As it turns out, due to the large statistical error of the negative best-fit, the final average and final statistical error in this bin is quite insensitive to whether or not this negative value is included. The second special case to mention is $N_\rho<0$ for $.6 < x < 1$ using the Webber spectrum modified by removing direct cluster decays, fitting using the scaled-up like-sign spectrum technique. For the method using this modified Webber spectrum to make sense, it must fit a larger N_ρ than when using the unmodified spectrum. I therefore ignore the fit to the modified spectrum where $N_\rho<0$, and instead simply take the N_ρ measured using the unmodified spectrum and scale it up by 20%: this 20% increase is predicted by a Monte Carlo study, and is within the systematic error relevant to this effect that I quote in this bin. Since this effect turns out to be small compared to the total systematic error of this bin anyway, the details of this adjustment are not significant.

Merits of the Basic Method

Having explained my analysis method and presented the results, I now turn to the question of why I favor my approach over alternative methods, and tests I've

x bin	Fitting Algorithm			
	Unscaled like-sign subtraction technique		Scaled-up like-sign subtraction technique	
	Lund Monte Carlo	Webber Monte Carlo	Lund Monte Carlo	Webber Monte Carlo
$.10 < x < .15$	1441 ± 370	648 ± 451	2056 ± 579	846 ± 830
$.15 < x < .20$	1166 ± 265	946 ± 288	1220 ± 455	1201 ± 330
$.20 < x < .30$	789 ± 318	300 ± 374	-1426 ± 1764	1601 ± 343
$.30 < x < .40$	943 ± 131	651 ± 178	913 ± 91	698 ± 174
$.40 < x < .60$	450 ± 114	234 ± 139	608 ± 92	524 ± 118
$.60 < x < 1.0$	135 ± 36	79 ± 56	149 ± 30	134 ± 31

Table 5.2: Number of ρ^0s fit in the data by each of the four fit procedures.

x bin	β	$\frac{1}{\beta\sigma_H}\frac{d\sigma}{dx}$	statistical error
$.10 < x < .15$	.766	3.86	1.42
$.15 < x < .20$	.910	2.55	0.71
$.20 < x < .30$	.960	0.91	0.36
$.30 < x < .40$	.981	0.87	0.13
$.40 < x < .60$	.991	.240	.055
$.60 < x < 1.0$	.994	.037	.010

Table 5.3: ρ^0 differential cross-section with statistical errors.

made to verify the validity of my technique.

Preparation of the Spectra

To test if my sphericity requirements in event selection introduced a bias, I remeasured the differential cross-section using only the good multihadron events which failed the sphericity-dip cut. I used the unscaled like-sign subtraction technique, taking both Monte Carlos in turn, for a total of two measurements of $\frac{1}{\beta\sigma_H}\frac{d\sigma}{dx}$. These measurements were consistent within errors of the same measurements performed using good events, with no systematic trend of deviations observed (although the errors are large due to the small sample size).

The single-track cuts are straightforward, and as can be seen from Figure 5.2, details of the cut thresholds are unlikely to affect the analysis. At low momentum, however, the 1 cm vertex cuts potentially remove too many pions or cut in a rapidly changing distribution. To test the sensitivity of the analysis to this cut, I remeasured $\frac{1}{\beta\sigma_H}\frac{d\sigma}{dx}$ using a 2 cm vertex cut in both the bending plane and in z. Comparing the cross-sections (as measured using the unscaled like-sign subtraction algorithm and Lund as the Monte Carlo) revealed negligible differences between the results of the two sets of vertex cuts.

I did a similar test of the track-pair cut requiring both pions to be in the same event hemisphere. I reran the analysis (unscaled like-sign subtraction, Lund Monte Carlo) eliminating this requirement. The cross-sections measured under both sets of cuts were consistent to well within errors.

To test the sensitivity of the measurement to particle identification criteria, I reran the analysis accepting a track regardless of how few wires or pads were used for the dE/dx information. The cross-sections measured under both sets of cuts were consistent to within errors.

In addition to the track-pair cuts that I made, there were a number that I

considered and rejected: Monte Carlo studies showed them to be of little assistance in this analysis. For completeness, I list these rejected trial cuts: (a) cut on θ^*, the angle between the pion momentum and the reconstructed ρ^0 momentum in the ρ^0 rest frame; (b) require each pion to be in the same hemisphere defined by the direction of travel of the ρ^0; (c) cut on the minimum ρ^0 momentum; and (d) cut on the momentum transverse to the jet direction of one or both pions.

Fitting the ρ^0

The technique I use of subtracting the like-sign dipion spectrum (scaled or unscaled) from the unlike-sign spectrum, and taking the background from the Monte Carlo histograms, has numerous merits:

- The large combinatoric background beneath the ρ^0 is reduced without diluting the ρ^0 itself, reducing systematic errors from uncertainty in the background shape.
- Certain resonance contributions (e.g. $K^{*\pm} \rightarrow \pi^{\pm}K_s$, $K_s \rightarrow \pi^+\pi^-$) appear equally in both like- and unlike-sign spectra and so cancel in the subtraction; other resonant contributions at least partially cancel.
- The imperfect reproduction of the data dipion spectra in the Monte Carlo, appearing roughly equally in both like- and unlike-sign spectra, is mostly cancelled.
- There is no need to involve the mass region <600 MeV in the fit—a mass region rich in resonant structure (and subject to Bose-Einstein effects in the like-sign case) and therefore prone to introducing systematic errors if used.
- Certain systematic errors (such as mismodeling of pion identification or trackfinding efficiency) cancel in the subtraction.

- Details of structure in the mass spectra are preserved (instead of being obliterated in a smooth analytic fit).
- The procedure is simple, allowing for efficient exploration of systematic errors.

The primary demerit of this analysis technique is the increase of statistical errors inherent in the operation of subtracting histograms.

I tried and rejected a variety of other techniques to fit the ρ^0, aiming at reducing the statistical errors of the fits. One can *a priori* reject fitting the unlike-sign data with a background taken directly from the Monte Carlo due to the obvious discrepancy between the two. One may also reject *a priori* any technique using a smooth analytic curve fit to the Monte Carlo for the background: the reduction in statistical errors is minimal, for the Monte Carlo sample is almost four times the size of the data set. I attempted to fit the unlike-sign spectra (both with and without subtraction of the like-sign spectra) with a smooth analytic background plus ρ^0 line shape independently in the data (for N_ρ) and Monte Carlo (for acceptance correction); these fits proved to be unstable, however, without benefit of a mass sideband below the ρ^0 to control the background curve. I also attempted subtracting from the unlike-sign spectra a smooth analytic fit to the like-sign spectra (instead of subtracting the like-sign histograms themselves), using backgrounds taken from similarly-prepared Monte Carlo spectra. While this last method did reduce the statistical errors of the fits, it proved to be subject to systematic errors larger than those of my chosen method, as revealed by running the analysis on a Monte Carlo (treating it as if it were data) and comparing the best-fit N_ρ to the true N_ρ. I conclude that reduction of the statistical errors of the fits can only be accomplished by increasing the systematic errors, so I am satisfied with my nominal method.

My method leaves two parameters free in the fit to the data: the PWBW magnitude to account for the cases where both pions from a ρ^0 decay are paired, and the background magnitude to account for all other pairings. This approach makes the tacit assumption that pairings of one pion from a ρ^0 decay and one unrelated pion have a mass structure similar to that of pairings of pions neither of which came from ρ^0 decay. Only in this case is the magnitude that I call "background" correctly accounting for all the pairs not stemming from the same ρ^0. Using the Monte Carlo to test this assumption, I compared spectra consisting of pairs of pions exactly one of which came from a ρ^0, to spectra consisting of pairs of pions neither of which came from a ρ^0. The agreement is good: fitting one set of spectra by the other set in .6–1.2 GeV gives an average χ^2/d.o.f. of 1.2 for 14 degrees of freedom for $x < .6$. (The fit was bad for $x > .6$, where systematic errors are large anyway.) Especially since the extracted spectra represent only 20–25% of the total, I conclude that they are sufficiently similar to verify the tacit assumption of similarity.

5.3 Estimation of Systematic Errors

Sources of systematic error are considered below. The quantified errors are listed in Table 5.4. These errors are combined in quadrature to arrive at an overall systematic error in each bin.

Background

By far the dominant systematic error is the uncertainty in the background underneath the ρ^0. I estimate this uncertainty as follows. In a given Monte Carlo (either Lund or Webber) I measure N_ρ by applying my analysis technique, using the other Monte Carlo for backgrounds. The N_ρ that I fit in the analysis can be compared to the number actually present to arrive at a figure of mismeasurement.

If I use the true background, I will measure (within statistical errors) the true number of ρ^0s, $N_\rho{}^{true}$, present in the spectrum. Thus, if one ignores statistical scatter, the deviation of the measured number, $N_\rho{}^{meas}$, from $N_\rho{}^{true}$ is attributable to the background being different from the true background. (Ignoring statistical variation must result in a somewhat conservative estimate of the background systematic.) I assume that the two Monte Carlos reasonably reproduce the data, and hence comparing one to another (where the errors are known) to estimate the systematic error is a reasonable approximation of the systematic error when fitting data by the Monte Carlo (where the errors are unknown).

Both Monte Carlos can be fit by my analysis method (taking backgrounds from the other Monte Carlo), each undergoing the two ρ^0-fitting techniques, for a total of four such comparisons. For each comparison, I compute the percentage mismeasurement:

$$\left| \frac{N_\rho{}^{meas} - N_\rho{}^{true}}{N_\rho{}^{true}} \right| \text{ x } 100 .$$

I average these four numbers, weighting by the inverse square of the statistical error of the fit, to arrive at a final estimate for the percentage of mismeasurement in each x bin. Not having a particular model of how this systematic error should depend on x, I attempt no smoothing or neighboring-bin averaging: instead, I simply compute the errors independently in each x bin.

To test the effect of statistical fluctuations in the Monte Carlo backgrounds, I re-measured $\frac{1}{\beta\sigma_H}\frac{d\sigma}{dx}$ using the differences of smooth analytic fits to the Monte Carlo $M(\pi^+\pi^-)$ and $M(\pi^\pm\pi^\pm)$ histograms (instead of subtracting the histograms themselves). Except for $.10 < x < .15$, these fits were consistent with my nominal method to within systematic errors. For $.10 < x < .15$ these fits were 30% higher than the nominal fits.

To test the effect of the discrepancy between Monte Carlo and data subtracted spectra, I re-measured $\frac{1}{\beta\sigma_H}\frac{d\sigma}{dx}$ using a free five-parameter analytic background fit

instead of taking backgrounds from the Monte Carlos. This free fit background is pulled up in the data by the excess of entries below the ρ^0 mass, thus yielding a smaller ρ^0 area. Except for $.10 < x < .15$, these fits were consistent with my nominal method to within systematic errors. For $.10 < x < .15$, where the discrepancy is most apparent, these fits were 30% lower than the nominal fits.

I conclude from these checks that my systematic errors as determined above are reasonable except for $.10 < x < .15$. In this bin I increase the systematic error to 30% to account for its special sensitivity to background assumptions and to the discrepancy between data and Monte Carlo at low x in the mass region below the ρ^0.

ρ^0 shape

There is some *a priori* uncertainty in what to use for the P-wave Breit-Wigner (PWBW) functional form for the ρ^0 [45]. More important still are effects predicted by the details of various hadronization schemes: some perhaps artifacts, some perhaps physically expected.

The most important of these considerations is an effect predicted by the Lund hadronization scheme. The LSFF (Equation 2.5) favors higher-momentum decays for more massive particles. Because the ρ^0 is so broad, a given ρ^0 can assume a wide range of actual masses; and a more massive ρ^0, on average, will have a stiffer spectrum than a less massive ρ^0 under the influence of the LSFF. In the cross-section measurement, the act of segregating ρ^0s according to x therefore groups stiff ρ^0s (soft ρ^0s) together which should have higher (lower) mass, on average. The upshot is that Lund predicts a ρ^0 line shape distorted toward higher masses at high x: for $.6 < x < 1$, for example, the best-fit M_0 and Γ_0 in the Lund Monte Carlo are found to be $\sim$ 11 MeV and $\sim$ 14 MeV larger than the generator values, respectively. (Observation of this effect would be very

interesting evidence for the physical reality of the string decay model. I looked at the data, and found it impossible to get reliable fits when floating M_0 and/or Γ_0 due to the low statistics. This bears further investigation should significantly more data become available.)

There are other generator-dependent distortions of the PWBW. For example, toward the end of the Lund iterative decay scheme, particles are produced at low x with insufficient energy to form a high-mass ρ^0—this results in a ρ^0 line shape distorted toward low mass at low x.

To somewhat counterbalance these ambiguities about the correct ρ^0 line shape to use—which stem essentially from its broad width—is the fact that detector resolution broadening of the signal is negligible compared to its intrinsic width. This means detailed understanding of the detector resolution is unnecessary for the determination of the proper resonance shape.

To estimate the potential systematic error from using the wrong line shape when fitting to the data, I fit the area of a histogram generated from a ρ^0 PWBW, the fit using a PWBW shape with a variety of fixed M_0 and Γ_0. I fixed M_0 and Γ_0 at several values extending from 760 MeV to 783 MeV for M_0, and from 140 MeV to 170 MeV for Γ_0; I performed the fits in two different mass windows (.6–1.2 GeV and .6–1.8 GeV). In these fits the fit area deviated from the true area by typically less than 1–2% (4% in the worst case). As these values for M_0 and Γ_0 cover the full range expected from the discussed effects, I conclude that for any reasonably expected mass and width in the data at any $x \geq .10$, I incur <2% systematic error by fixing $M_0 = 771$ MeV and $\Gamma_0 = 154$ MeV.

I furthermore observe that the best-fit PWBW area typically deviates by ~1% from the true contents of the PWBW-prepared histogram; that the best-fit area changes by ~1% depending on the fit window; and that choosing an alternative form of the PWBW [45] changes the best-fit area by <2%. I lump all of these

systematic errors associated with the PWBW shape into a conservative estimate of 4% systematic error at all x.

Webber cluster

As detailed earlier, the Webber cluster$\rightarrow\pi^+\pi^-$ decay introduces a systematic uncertainty; I perform several fits to quantify this uncertainty. Fitting the data in turn by the previously-described two versions of the Webber spectra gives a measure of the effect. As equivalent tests, I fit both versions of Webber spectra as if they were data, using Lund as the Monte Carlo; and fit Lund as if it were data using both versions of Webber as Monte Carlo. I do these three tests for both scaled and unscaled like-sign analysis techniques, for a total of six estimations of the effect. For each of these six tests, I compute

$$\frac{\frac{1}{2}\left|\mathrm{N}_\rho - \hat{\mathrm{N}}_\rho\right|}{\frac{1}{2}\left(\mathrm{N}_\rho + \hat{\mathrm{N}}_\rho\right)} \quad ,$$

that is, half the fractional excursion between the fit number of ρ^0s using Webber as is (N_ρ) and using the modified Webber spectra ($\hat{\mathrm{N}}_\rho$). I then average these six numbers to arrive at a quantification of this uncertainty, listed in Table 5.4.

Beta

The β occurring in $\frac{1}{\beta\sigma_H}\frac{d\sigma}{dx}$ refers to the β of ρ^0s at that x; when performing the analysis in discrete x bins, β must represent an appropriate average over the x bin in question.

Since the β of ρ^0s carries no necessary relation to the β computed from random pion pairings, I cannot determine it directly from the data (which is mostly combinatoric in origin). I can compute it from the measured differential cross-section, but this is liable to be subject to relatively large errors. Instead, I compute it directly from the Monte Carlo. Since the average β in a bin depends only on the shape of the differential cross-section, and since the shapes of the two

generators I use generally agree with each other and with the data (although the magnitudes differ), I assume that β is not strongly model-dependent, and hence it is safe to determine it from the Monte Carlos.

I compute β as follows. In each x bin, using the Lund and Webber Monte Carlos in turn, I compute $\left\langle \frac{1}{\beta} \right\rangle^{-1}$ for generated ρ^0s in events without initial state radiation. I take the average of $\left\langle \frac{1}{\beta} \right\rangle^{-1}$ as my final value for β. I take half the absolute difference of the two values as my estimate of the systematic error on β, expressed as a percentage. My values for β are listed in Table 5.3; the errors are listed in Table 5.4.

Nuclear interactions

Pions may undergo nuclear interactions in the material between their creation point and the fiducial volume of the TPC. These interactions can scatter pions, absorb pions, or produce more pions, so reproducing their effect in the detector simulation is important in getting the simulated backgrounds and acceptances right.

To estimate the error in ρ^0 acceptance from mismodeling the nuclear interactions, I consider pions in the Monte Carlo from ρ^0s deemed "findable." A findable ρ^0 is one in an event that passes the event selections criteria, whose daughter pions satisfy (before detector simulation) the track-pair cuts, and whose daughter pions each have momentum > 150 MeV/c pointed $> 30°$ away from the beam direction. Up to the track-quality cuts, these are the ρ^0s one would expect to find in the $\pi^+\pi^-$ spectrum if it were not for interactions in the material in front of the TPC. In each x bin I tabulate (a) the number of findable ρ^0s, and (b) of these, the number that have at least one daughter undergoing a nuclear interaction of any type.

In the worst-case bin ($.10 < x < .15$), 15% of findable ρ^0s have daughters

involved in nuclear interactions. Since the Monte Carlo interactions are estimated to be accurate to within 10% of reality [46], this 15% is accurate to within $\sim 2\%$. That is, one expects only $\sim 2\%$ of the ρ^0s to have nuclear interactions not correctly modeled in the detector simulation. Since not all nuclear interactions remove a $\pi^+\pi^-$ mass from the ρ^0 region, to quote a full 2% systematic uncertainty in the ρ^0 acceptance for this bin is a conservative choice, which I make. The errors for the other bins' acceptance are computed in the same manner.

A priori, the background is also subject to errors from mismodeling nuclear interactions; but since the background is composed of the difference between two dipion spectra, errors in the dipion acceptance should cancel. Since I have just shown that any such error is individually small to begin with, background errors from mismodeling nuclear interactions are negligible.

Pion decay

The decay $\pi \rightarrow \mu$ affects the Monte Carlo acceptances and backgrounds in the same way as nuclear interactions and are evaluated in the same manner. The background error is negligible for the same reasoning as in the case of nuclear interactions.

Track reconstruction efficiency

The track-finding efficiency in the TPC (excluding geometric losses) is estimated to be 97%±2% [28]. The 2% uncertainty of single-track efficiency means a 4% uncertainty in the two-track—hence ρ^0—acceptance.

Pion identification

I find 97% pion acceptance (flat in x) for my particle identification cuts, judged to be accurate to within 2%. As with the track reconstruction efficiency uncertainty, this leads to a 4% systematic error in ρ^0 acceptance.

To verify this systematic error, I perform the following test. The establishment of the identity χ^2 for a given species hypothesis depends on three things: 1) the assumed dE/dx curve, 2) the dE/dx resolution, and 3) the momentum resolution. Of these, (1) is known by far the best, (2) is known to within about 8% of itself, and (3) is known to within about 10% of itself. I assume (1) is correct, and test the sensitivity of my analysis to (2) and (3) by refitting N_ρ in the data after reprocessing all tracks with the resolutions altered up and down by their uncertainty. The uncertainty in (2) dominates the uncertainty in (3); the average absolute percent shift in N_ρ under raising and lowering (2) is 2%, indicating that a 4% systematic is, if anything, conservative.

Errors in the background are negligible from track reconstruction and pion identification systematics for the same reasoning as in the case of nuclear interactions.

Fitting window

The analysis technique to fit N_ρ should not depend on the mass window used in performing the fits. To test this, I fit N_ρ in the data (using the Lund backgrounds) using several different mass windows: .6–1.0 GeV, .6–1.2 GeV, .6–1.4 GeV, and .6–1.6 GeV. I found that fits using different windows were consistent to well within errors, and that the fits showed no systematic trend (except that N_ρ was occasionally a little low when fit in .6–1.0 GeV). This indicates that the analysis is insensitive to the fit window, as long as it extends to 1.2 GeV or beyond.

As a high-statistics test of this claim, I lumped all the data for $x > .10$ together and measured the ρ^0 multiplicity by fitting in the mass windows .6–1.2 GeV, .6–1.4 GeV, and .6–1.8 GeV. I used only Lund backgrounds, but used both unscaled and scaled subtraction algorithms. The rms deviation of these six measurements was 7%. This is not quite a true test of my nominal method, since it

does not allow for independent background subtraction as x varies (and is therefore unduly weighted by the many entries at low x where systematic background errors are known to be large); moreover, the 7% variation may be partly statistical in origin. I believe this makes a 7% systematic error a conservative estimate, but one I choose to quote.

K^{*0} area

Because kaons are misidentified as pions most often near the K/π crossover, the contribution of the K^{*0} to the $\pi^+\pi^-$ spectrum is significant only in one x bin, $.10 < x < .15$. In this bin its area is about a fourth as large as the ρ^0 area. Taking the K^{*0} contribution from the upper and lower extremes of measured values and Lund and Webber predictions (see Section 7.4) makes the measured N_ρ in the data vary by 5% for $.10 < x < .15$. I am therefore unlikely to be more than 5% in error in my final measurement of N_ρ and hence $\frac{1}{\beta\sigma_H}\frac{d\sigma}{dx}$; 5% is the error I assign in this bin. The errors in the other bins were estimated in the same manner and found to be $\sim 1\%$.

Attempts to Diagnose the Mass Discrepancy

For completeness, I list here the attempts I made to diagnose the low x, low mass discrepancy between Monte Carlo and data in the $M(\pi^+\pi^-)$ - $M(\pi^\pm\pi^\pm)$ subtracted spectra. The discrepancy persisted for extensive variation of track and particle identification cuts, so I believe it's not an artifact of my particular set of cuts. I examined the predicted contribution to the mass spectra from all likely 0^-, 1^-, 1^+, and 2^+ mesons to see if a reasonable shift in Monte Carlo assumptions (production rates, decay branching fractions, detector acceptance) could explain the excess seen in the data, but none had the necessary combination of spectrum shape and magnitude.

The discrepancy remained when requiring all tracks to lie $> 50°$ away from the

Source of Error	x bin					
	.10–.15	.15–.20	.20–.30	.30–.40	.40–.60	.60–1.0
Background	30	10	25	45	35	75
ρ^0 shape	4	4	4	4	4	4
Webber cluster	2	2	2	2	5	20
β	4	1	0	0	0	0
Nuclear interactions	2	2	1	1	1	1
Pion decay	2	2	1	1	1	1
Tracking efficiency	4	4	4	4	4	4
Identification efficiency	4	4	4	4	4	4
Fitting window	7	7	7	7	7	7
K^{*0}area	5	1	1	1	1	1
Quadrature Total Systematic Error	32	15	27	46	37	78
Statistical Error	38	28	40	15	23	26

Table 5.4: Systematic and statistical errors. All figures expressed in %.

beam direction, regardless of whether track pairs were required to be in the same sphericity hemisphere or not, so I do not suspect mismodeling of interactions in the beampipe as the culprit. Further tests of the TPCLUND detector simulation were made by dividing track pairs into several momentum and polar angle bins and observing that the discrepancy was present in all bins, whereas it's unlikely that TPCLUND — abundantly checked in other people's analyses — is wrong across the board. Moreover, the discrepancy existed in data collected in an earlier configuration of the detector for which a different version of TPCLUND was used, so an element of the current version of TPCLUND wrong in detail is unlikely to be the source of the problem.

The excess in the data cannot be due to Bose-Einstein enhancement, for (a) it appears in the unlike-sign spectra, and (b) it extends to masses too high to be subject to this effect. To investigate the ability of a tune of Monte Carlo parameters to eliminate the discrepancy, I generated detector-simulated events

for four different tunes of the Lund v5.3 Monte Carlo; all continued to exhibit the effect. To test the role of the hard QCD generation scheme, I generated detector-simulated events using the parton shower algorithm of Lund v6.3; the discrepancy was not reduced. (And it is present in the Webber prediction as well, also a parton shower scheme.) I explored several different cutoffs to the hadronization process in both Lund and Webber to see if the effect was sensitive to the essentially *ad hoc* termination of the fragmentation schemes, all to no avail.

In short, the mass discrepancy between data and Monte Carlo at low x in the subtracted spectra was stable against all my attempts to explain and eliminate it. There may be interesting hadronization physics implicit in this effect, but further investigation of this possibility is outside the scope of this thesis.

5.4 Results

The ρ^0 differential cross-section measured in this study (with radiative corrections applied following the prescription of Equation 1.2) is plotted in Figure 5.7, along with the results from several other experiments [47,48,49,50]. (The JADE, TASSO, and HRS measured quantities are $\frac{s}{\beta}\frac{d\sigma}{dx}$. To convert to $\frac{1}{\beta\sigma_H}\frac{d\sigma}{dx}$, I divide by $\sigma_H s = \frac{4\pi\alpha^2}{3}\cdot R$, assuming $R = 3\sum_{i=1}^{5} q_i^2(1+\frac{\alpha_s}{\pi}) = 3.84$ using $\alpha_s = 0.15$.) Comparison to the two Monte Carlo generators is made in Figure 5.8. Forming a χ^2 from my measured contributions in each x bin and the Monte Carlo predictions quantifies the agreement between the generators and this experiment. This χ^2 for six degrees of freedom is 8.2 for Lund and 7.6 for Webber, indicating that both models do equally well in predicting the ρ^0 differential cross-section. The points plotted for all experiments (including this one) indicate statistical error bars only, except for the HRS measurement which shows their systematics-dominated total error bars. The horizontal bars on my measured points simply represent the extent of the x bins. The points are located in x at the average x of the bin,

computed from an exponential fit to the cross-section.

To get the total measured ρ^0 multiplicity, I sum the contributions to the multiplicity from each x bin as measured in this analysis for radiationless initial state events. This gives 0.50 ± 0.07 ρ^0/event measured in $x > .10$ taking statistical errors only. Combining all mass pairs for $x > .10$ and then fitting with my analysis technique yields a ρ^0 multiplicity of 0.39 ± 0.09 for $x > .10$. Since this latter technique does not allow for independent background subtraction as x varies, I am not surprised by the discrepancy with the sum of the individual fits. Combining the systematic errors from each bin quadratically yields an uncertainty on this multiplicity of 11%. Combining them linearly yields an uncertainty of 27%. As there are certainly some, but not perfect, correlations of the systematic errors among the bins, these two figures bracket the sensible range of systematic errors. A hybrid approach to combining systematic errors, wherein a 15% error is assumed to be correlated and the rest is uncorrelated, finds a reasonable 20% systematic uncertainty; I use this value in the remaining discussion.

An auxiliary exercise in calculating the total ρ^0 multiplicity involves fitting a smooth curve to the measured $\frac{1}{\beta\sigma_H}\frac{d\sigma}{dx}$; a single exponential does well. I take the abscissa of the cross-section points to be the $\langle x \rangle$ in each bin computed from the previous fit; the fit converges in two iterations. This fit has a χ^2 of 4.7 for four degrees of freedom.

The Lund Monte Carlo, Webber Monte Carlo, and exponential fit predict 34%, 28%, and 30% of all ρ^0s generated in events without initial state radiation to have $x < .10$, respectively. Using these figures to extrapolate the sum of individual x bin measurements to the full x range, I find 0.76 ± 0.11, 0.69 ± 0.10, and 0.71 ± 0.10 ρ^0/event produced in radiationless initial state events assuming the Lund, Webber and exponential correction, respectively.

An alternative method to calculate the total ρ^0 multiplicity is to fit a fixed

Source	ρ^0/event
TPC (this study)	$.77 \pm .17$
TASSO	$.72 \pm .15$
JADE	$.98 \pm .17$
HRS	$.95 \pm .09$
MARK II	$.67 \pm .11$
Lund Generator	.84
Webber Generator	.62

Table 5.5: ρ^0 multiplicity in this and other experiments, and as predicted by the Monte Carlos. Errors are quadrature sums of statistical and systematic errors.

shape to the differential cross-section and integrate the multiplicity under the curve (correctly accounting for $\frac{1}{\beta}$). This tends to reduce statistical errors at the cost of introducing systematic error from the assumed fixed shape. I use three shapes for this approach: the Lund predicted shape, the Webber shape, and the exponential shape. The fits to the Monte Carlos are a one parameter fit, floating the normalization of the generator curves; the exponential is a two parameter fit. The results of these fits for Lund, Webber, and exponential, respectively, are 0.80 ± 0.08 ($\chi^2 = 8.0$ for 5 d.o.f.), 0.76 ± 0.07 ($\chi^2 = 4.1$ for 5 d.o.f.), and 0.74 ± 0.10 ($\chi^2 = 4.7$ for 4 d.o.f.). Since these fits cluster closely, I judge that the systematic error from dependence on assumed cross-section shape is sufficiently small to be neglected in comparison to the other errors in this analysis. I choose to average the results of these fits to arrive at my final result. Including the 20% systematic error, this yields $0.77 \pm 0.08(stat) \pm 0.15(syst)$ ρ^0/event as my measure of total ρ^0 multiplicity. This multiplicity is compared to the determinations of other experiments and the predictions of the Monte Carlos in Table 5.5. (No correction is made for the differing $\sqrt{s}$ of the various experiments. The Monte Carlo predictions are for $\sqrt{s} = 29$ GeV.)

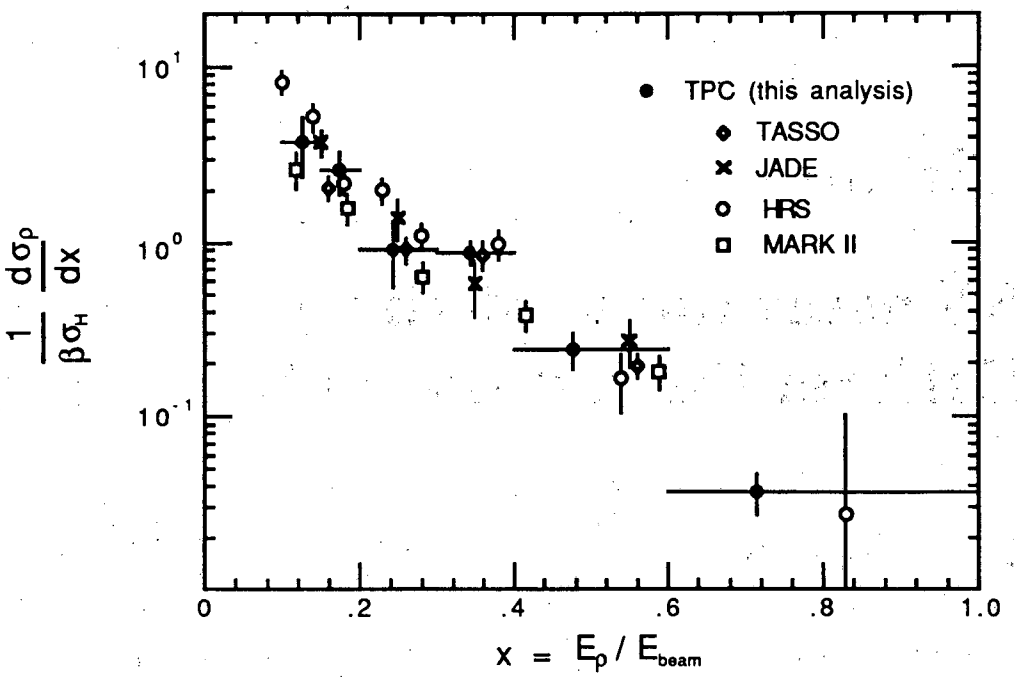

Figure 5.7: ρ^0 differential cross-section in this and other experiments. Errors (except for HRS) are statistical only.

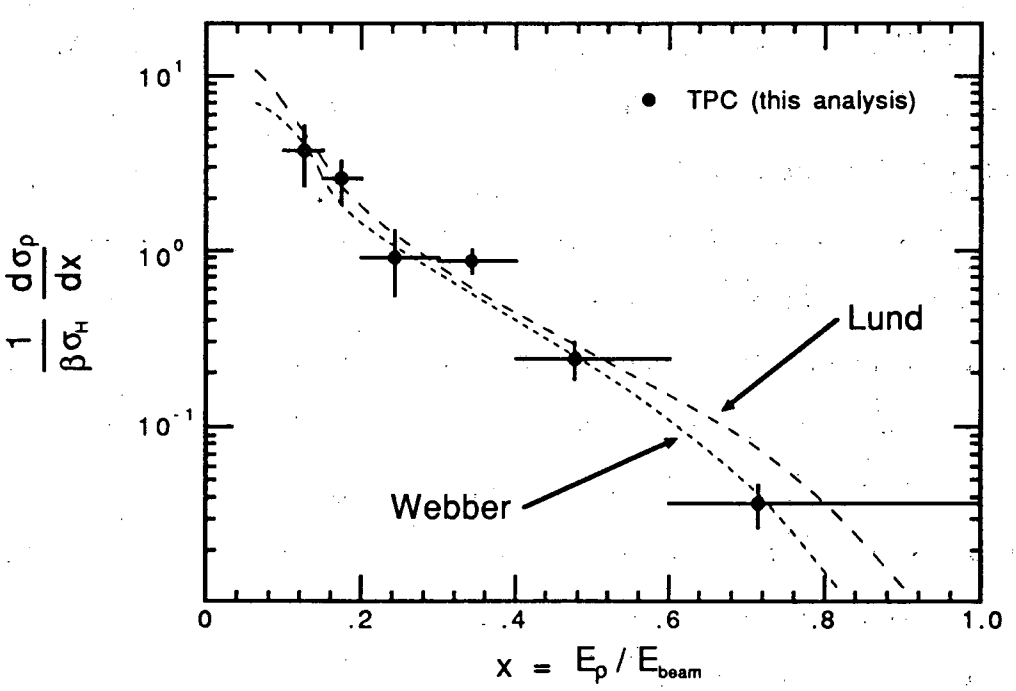

Figure 5.8: ρ^0 differential cross-section measured in this experiment, along with the predictions of Monte Carlo generators. Errors are statistical only.

Chapter 6

Measurement of the ϕ Differential Cross-section

6.1 Overview

The ϕ is a narrow resonance (Γ = 4.2 MeV, M = 1019.5 MeV) which decays frequently to K^+K^- (49.5% branching fraction), the decay mode studied in this analysis. Implicit in these characteristics are the salient features of the ϕ analysis.

Because the decay mode is to charged kaons, the TPC's particle identification ability greatly reduces the background under the ϕ peak. The remaining background is virtually entirely combinatoric and smooth; resonant structure in this K^+K^- background is negligible.

Because the daughters' masses sum to nearly the mass of the ϕ, the decay products have little momentum in the ϕ rest frame. This means the daughters have similar momenta when boosted to the lab frame, which in turn means a) the tracks are close in space and the detectors' ability to resolve them must be well understood, and b) that in momentum regions of low kaon acceptance — in particular the K/π crossover region — the ϕ acceptance shows a pronounced hole if both kaons are subject to stringent identification criteria.

Lastly, the narrow width of the ϕ is comparable to the detector resolution, so that understanding the correct line shape to use for the ϕ peak in the data

and the Monte Carlo — and thereby estimating the acceptance correctly — is not trivial.

Because my ϕ analysis measures the ϕ independently in the data and the Monte Carlo (as opposed to the ρ^0 analysis, where Monte Carlo backgrounds were used when measuring the data), the Monte Carlo measurement serves only as an acceptance correction (and a tool for probing systematic errors). This is essentially a question of detector simulation, insensitive to the particular physics generator used, as long as the generator gets the gross features of the multihadron event environment close to reality. There is therefore no need to duplicate this analysis using different Monte Carlo generators; for the ϕ study I use only the Lund generator, and in this chapter "Monte Carlo" is always taken to mean the Lund Monte Carlo package.

I have previewed some features of the ϕ analysis in this section. In Section 6.2 I explain the method I've chosen for the ϕ analysis and present the cross-section results (with statistical errors only). In Section 6.3 I estimate systematic errors, with final results and errors described in Section 6.4.

6.2 Basic Method

In order to measure $\frac{1}{\beta\sigma_H}\frac{d\sigma}{dx}$, I divide the data and Monte Carlo mass spectra into five x bins for $.1 < x < .8$, and measure the area in the ϕ peak independently in each bin. The x bins are chosen to be wide compared to the x resolution of the detector and to have reasonable numbers of ϕs in each bin. The specific x bins I use are given in Table 6.1.

6.2.1 Formation of the Mass Spectra

To be used in this analysis, an event must first pass the multihadronic event selection and sphericity requirements described in Section 4.2. For a track to

be used as a kaon candidate in forming the mass spectra, it must pass — apart from identity cuts — nearly the same track cuts as in the ρ^0 analysis. The only differences from that analysis are: cut (2) is relaxed to $dp_\perp/p_\perp < .10$ (if $p_\perp < 1$ GeV/c) or $dp_\perp/p_\perp^2 < .10$ (if $p_\perp > 1$ GeV/c), where $p_\perp$ is the momentum transverse to the beam axis and $dp_\perp$ is its error; and cut (3) is tightened to require momentum (extrapolated to the event vertex) > 350 MeV/c, since kaons range out in material before the TPC at higher momentum than pions. These cuts may be inspected from Figure 5.2.

The freedom in choosing the kaon identification cuts leads to important decisions. To begin with, I require no minimum number of wires for the dE/dx information, thus utilizing tracks that have dE/dx determined from pad signals. This is because the daughters of the ϕ, often close in space, will often lose wire dE/dx assignments due to ambiguity of the assignments of wire hits to tracks; the slight cost of worsened dE/dx resolution when using pads for the dE/dx measurements is worth the gain of higher acceptance and lessened systematic uncertainty of the acceptance.

Even more important is the choice of the particle identity selection. If no identification is used at all, ϕ acceptance is high but so is the background; this is similar to the procedure used by HRS [51]. If tight identification criteria are used on both kaons, the ϕ acceptance drops but so does the background; this is the procedure used by a previous measurement using the TPC [52]. (Under this algorithm, no measurement can be made in $.15 < x < .25$, the bin affected by the K/π crossover kaon acceptance hole, due to the miniscule ϕ acceptance.) For this analysis, I choose a middle ground: I require at least one kaon to satisfy a fairly tight identity cut, but the other kaon may satisfy a much looser identity cut. The increased ϕ acceptance relative to the earlier TPC approach, which improves the statistical significance of the signal, competes with the increased

background, which reduces the significance: the result is that the "one tight + one loose" selection has about the same statistical significance as the "two tight" selection. Moreover, this approach allows a measurement in $.15 < x < .25$, as there is sufficient ϕ acceptance after the cut for a meaningful result.

The ϕ acceptance (estimated from the Monte Carlo) for several approaches to kaon identification are shown in Figure 6.2. Acceptance here means the number of ϕs entering the mass plot after all cuts divided by the number of ϕs generated, both from Monte Carlo good events. I define the loose kaon identity selection to be $\chi^2_K < 9$, where χ^2_K is the particle-id χ^2 for the kaon hypothesis; this represents consistency of the track with the kaon identity. The tight kaon selection for my analysis I define to be $\chi^2_K < 9$, $\chi^2_e > 4$, and the probability (see Section 4.1.2) for being a kaon > 0.3; this represents a reasonably solidly identified kaon inconsistent with the electron hypothesis. (In studies requiring both kaons solidly identified, I strengthen the minimum probability requirement for the tight selection to 0.5.) The χ^2_K cut rejects 50.7% of tracks surviving previous cuts; of those tracks surviving the χ^2_K cut, 28.1% have a probability for being a kaon $>$ 0.3. These identity cuts are illustrated in Figure 6.1. The electron discrimination only matters for the lowest x bin, where the K/e dE/dx crossover at 600 MeV/c would otherwise admit conversion electron pairs which peak in mass near threshold, complicating the smooth background fit.

The kaon purity and acceptance as estimated from the Monte Carlo for the loose and tight identification cuts are shown in Figure 6.3. Integrated over all momentum, the purity is 26% (68%) [13%] and the acceptance is 77% (52%) [79%] for the loose (tight) [no] kaon selection. The purity is the fraction of good tracks (under the relevant identification scheme) that are actually kaons; the acceptance is the fraction of kaons generated in good events that are called good tracks (under the relevant identification scheme).

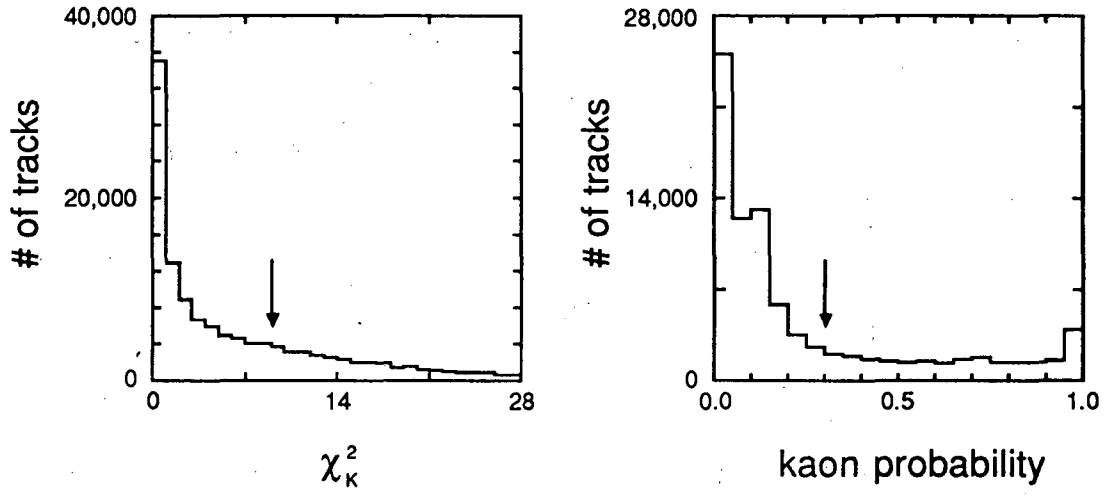

Figure 6.1: Kaon identity cuts for those tracks surviving previous cuts. The probability plot only contains entries for tracks passing the χ^2_K selection. The arrows indicate the cuts used in this analysis.

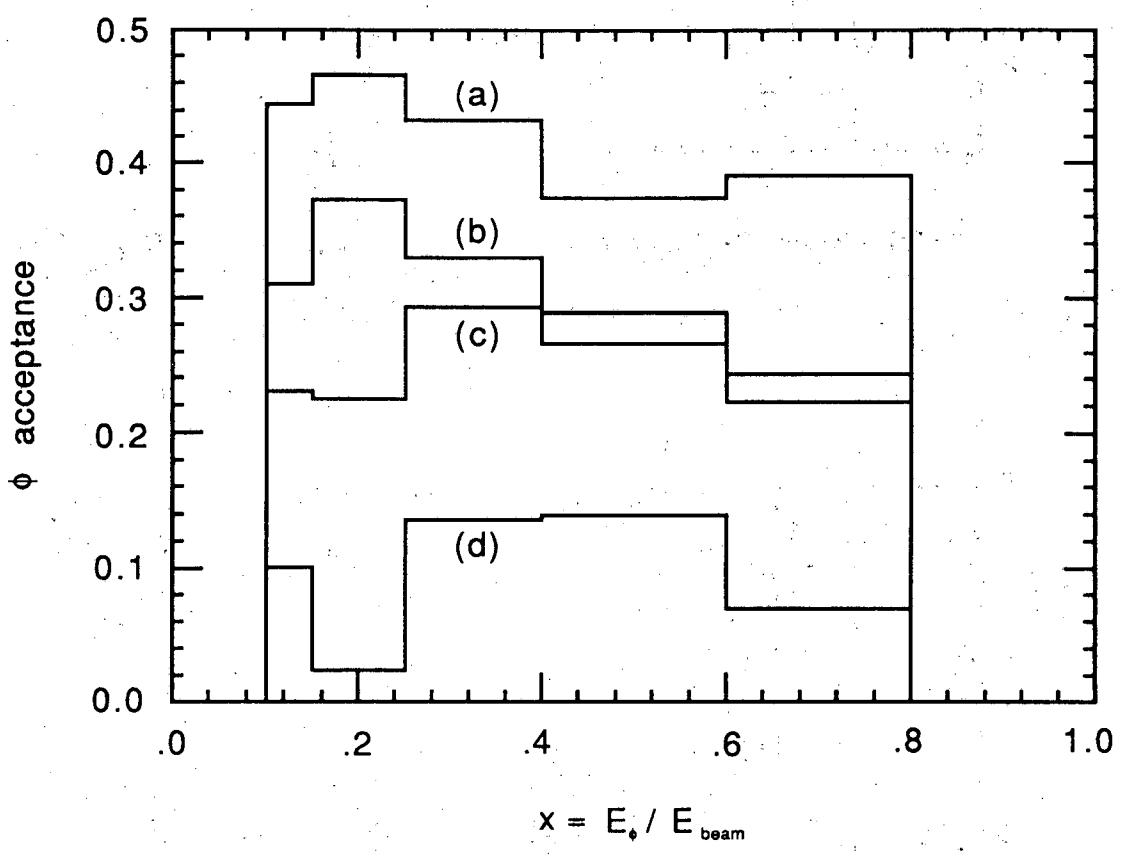

Figure 6.2: ϕ acceptance under various kaon selection schemes: a) no particle identification; b) require at least two loosely identified kaons; c) require at least one tightly identified kaon with one loosely identified kaon; d) require two tightly identified kaons. The definitions of tight and loose identification criteria are in the text.

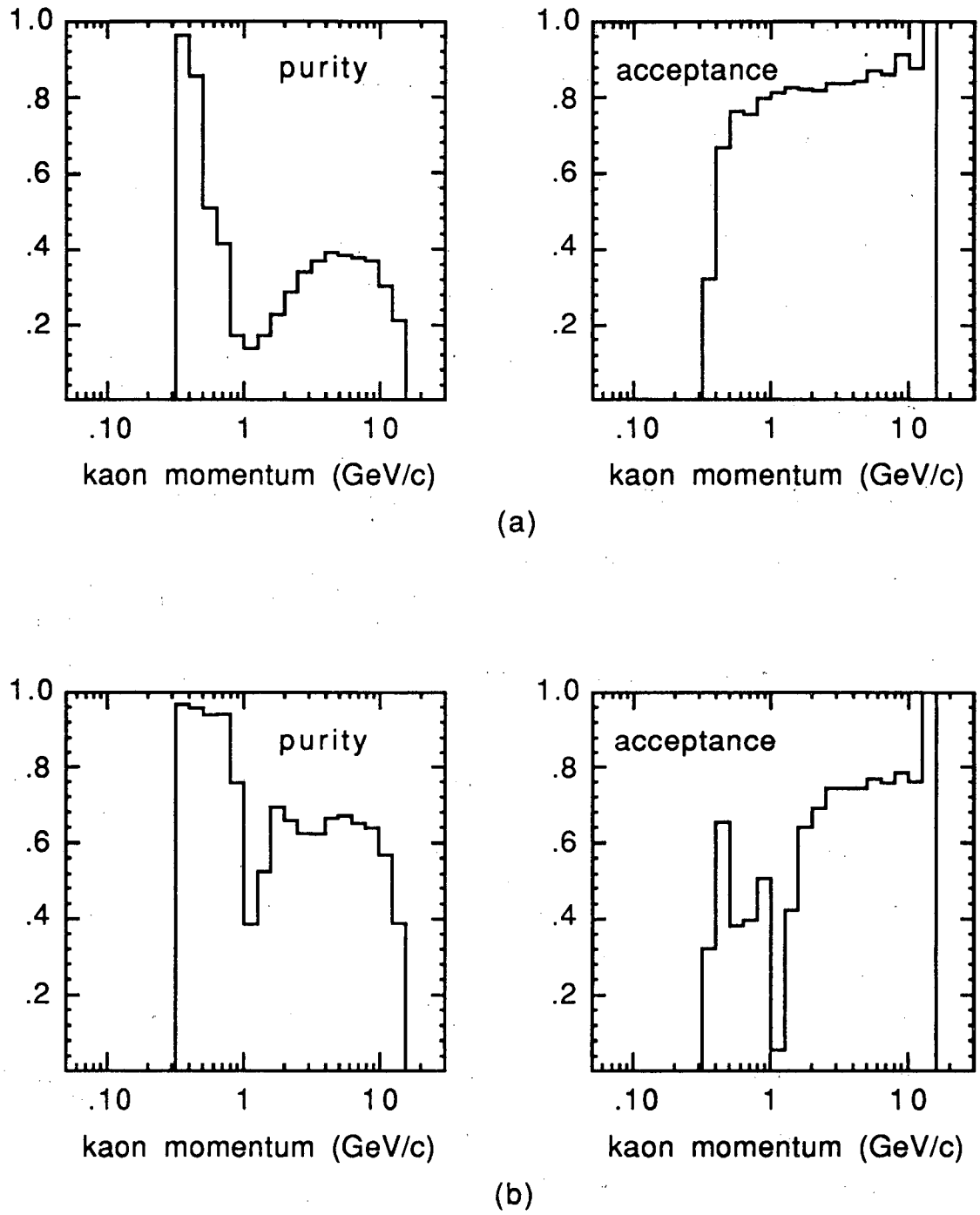

Figure 6.3: Kaon purity and acceptance under (a) loose ($\chi^2_K < 9$), and (b) tight ($\chi^2_K < 9$, $\chi^2_e > 4$, and kaon probability > 0.3) identification criteria. The dips around 1 GeV/c in purity (plots (a) and (b)) and acceptance (plot (b)) are due to the K/π crossover.

The invariant masses of track pairs surviving all the above selection passes, under the at least one tight kaon identification procedure, form the mass spectra from which I will extract the ϕ signal. No additional cuts at the track-pair level are made. These spectra from the data, divided into x bins, are histogrammed in 4 MeV bins in Figure 6.4 for both unlike-sign and like-sign combinations. The ϕ feature is prominent in all unlike-sign bins (at a mass and width consistent with the ϕ) and is absent in all like-sign bins, indicating that the observed peak is truly the ϕ and not an artifact of the selection.

6.2.2 Extracting the Cross-section

To extract the number of ϕs observed in a given mass plot, N_ϕ, I perform a maximum-likelihood fit to the spectrum using a smooth background function plus a resonance curve fixed in shape but floating in magnitude. The background curve is

$$c_1 m^{c_2}(c_3 - m)^{20}(1 + c_4 m + c_5 m^2) \tag{6.1}$$

where the c_i are the floating parameters of the fit. (The exponent fixed at 20 could in principle be a free parameter, but it proves to be highly correlated with c_3 when free, so it is sensible to fix it.)

The resonance curve for the ϕ is the convolution of the P-wave Breit-Wigner (PWBW) of Equation 5.1 and a fixed gaussian detector resolution. The Breit-Wigner parameters used are $\Gamma_0 = 4.0$ MeV and $M_0 = 1020$ MeV. The analysis is done twice, once using a detector resolution fixed at 2.5 MeV and once using a 3.5 MeV resolution; the results are averaged for the final N_ϕ.

The spectra are fit in the mass range from threshold to 1.28 GeV. The six-parameter (five background and one signal) fit to these 74 bins has 68 degrees of freedom. The fits are fair: the average χ^2 over all x bins for these 68 degrees of freedom for $x < .6$ is 84 (99) for the data (Monte Carlo). (An alternative

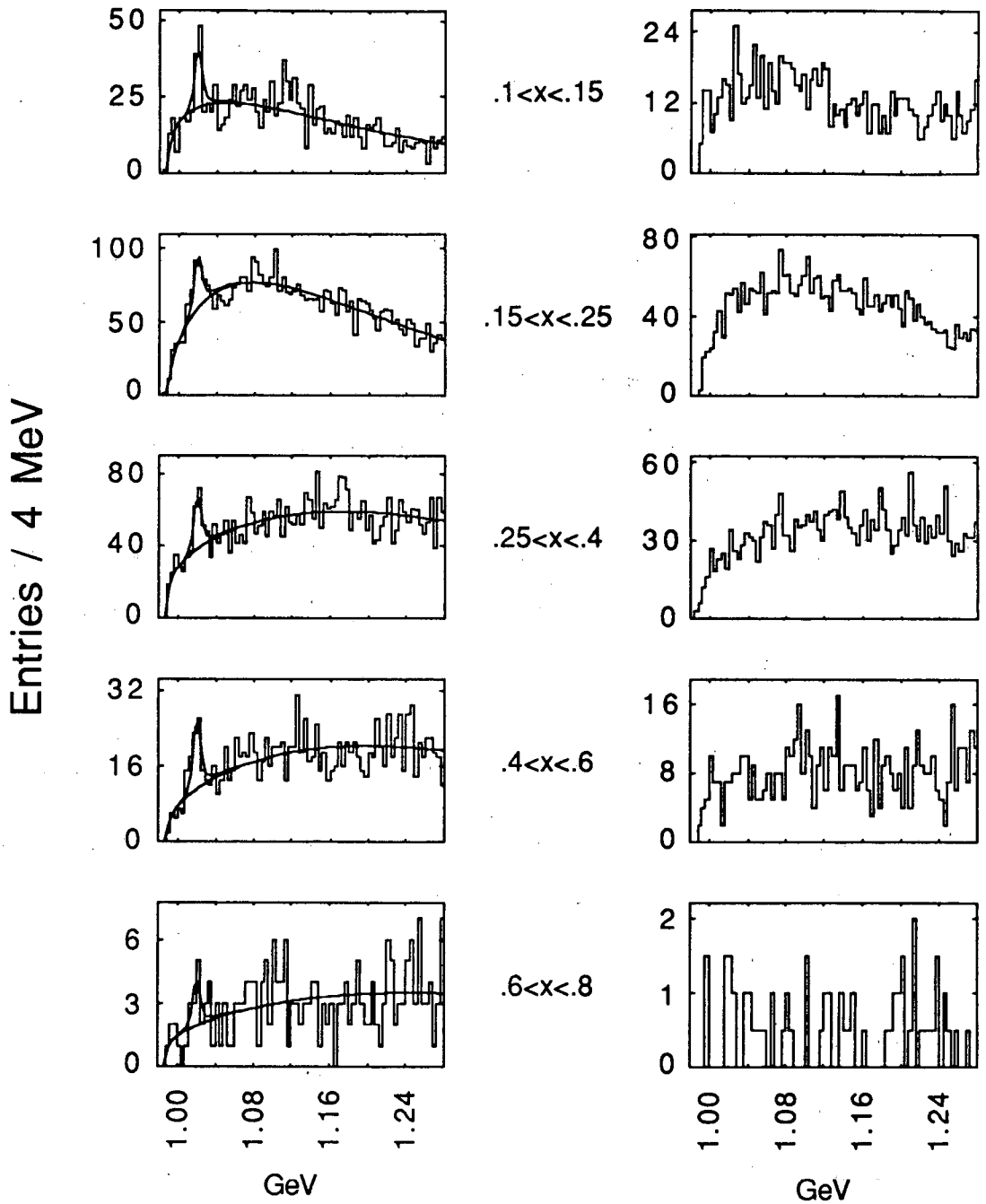

Figure 6.4: Dikaon invariant mass spectra from the data. Unlike-sign pairings are in the left column, like-sign pairings are in the right column. The curves show the results of the fitting procedure described in the text. The total fit (using a 2.5 MeV detector resolution for the ϕ) and the smooth background component are superposed.

x bin	β	N_ϕ	$\frac{1}{\beta\sigma_H}\frac{d\sigma}{dx}$
.10< x <.15	.807	55 ± 15	0.335 ± 0.097
.15< x <.25	.926	107 ± 24	0.311 ± 0.079
.25< x <.40	.974	89 ± 19	0.114 ± 0.026
.40< x <.60	.989	49 ± 11	0.051 ± 0.013
.60< x <.80	.995	6.1 ± 4.5	0.010 ± 0.007

Table 6.1: N_ϕ fit to the data and the derived ϕ differential cross-section; errors are statistical.

method, wherein I fix the four background shape parameters from a fit to the like-sign spectra before fitting for the ϕ, I reject because the χ^2s of the fits are markedly worse.)

The systematic errors incurred by this method of measuring N_ϕ are discussed in the next section. The results for $\frac{1}{\beta\sigma_H}\frac{d\sigma}{dx}$, derived from N_ϕ by the prescription of Equation 1.2, are presented with statistical errors in Table 6.1.

6.3 Estimation of Systematic Errors

Sources of systematic error are considered below. The quantified errors are listed in Table 6.2. These errors are combined in quadrature to arrive at an overall systematic error in each bin.

ϕ shape

If the spectra are fit with the wrong ϕ shape, a systematic error in N_ϕ will result. If the Monte Carlo mass resolution matches that of the data, this systematic error cancels out in the final cross-section by virtue of the acceptance correction; so the relevant information is how closely the Monte Carlo and data resolutions agree. I estimate the mass resolutions for the data and the Monte Carlo by a number of methods, described below.

A simple calculation sets the scale of the expected resolution. Assuming a

symmetric decay geometry and including multiple scattering and measurement error contributions to both the momentum and angular track resolution, this calculation predicts a mass resolution of 2.6 MeV at its optimum around $x = .2$, worsening to 3.3 MeV at $x = .1$ and 3.9 MeV at $x = .8$. This is in rough agreement with the resolution found by propagating quoted track errors for track pairs in the ϕ mass band 1.012<m(GeV)<1.028 (using the "two tight" kaon selection to maximize signal-to-noise): this exercise yields mass resolutions of 1.8 MeV to 2.6 MeV (2.3 MeV to 3.1 MeV) for the data (Monte Carlo) over the observed x range $.1 < x < .8$. This is also roughly consistent with the resolution in the Monte Carlo determined by fitting just the spectrum of accepted ϕs (i.e. with background removed) with a floating line shape, then deconvolving the gaussian detector contribution to the fit width; this exercise gives best-fit resolutions from 2.1 MeV to 5.1 MeV in the observed x range, with errors marginally consistent with the simple calculation.

Deducing the detector resolution from fits to the full mass spectra (i.e. with background present) using a ϕ signal free to float in shape is complicated by two effects. First, the errors in the resolution are large after deconvolving from the observed width. Second, the Monte Carlo shows a tendency for the background curve and the ϕ curve to interact, giving a larger measured width (and larger N_ϕ) to the ϕ than when fitting the ϕ contribution to this spectrum by itself. With these warnings in mind, the general trend of this estimate of the resolution is that the data is marginally consistent with the simple calculation, but systematically better; the Monte Carlo is marginally consistent with the calculation but systematically worse.

Because of the errors observed in fitting N_ϕ in the Monte Carlo with a floating line shape, and because the predicted detector resolution has been reasonably verified for both data and Monte Carlo as just described, I choose to fix the

ϕ shape when fitting the spectra. The shape is fixed as the convolution of a PWBW and the "right" detector resolution. The resolution is sufficiently flat in x to use one resolution for all x. The best estimate of the resolution from tests in the data (Monte Carlo) is around 2.5 MeV (3.5 MeV), values which bracket the prediction. I use these two resolutions in turn to generate the fixed ϕ shape, as described in the previous section.

I claim that the above estimates of the mass resolution show that it is surely between 1 MeV and 5 MeV in both data and Monte Carlo, but that the relative agreement of Monte Carlo and data cannot be pinned down more precisely than that. In order to quantify the possible systematic error from ϕ shape disagreement between data and Monte Carlo, I refit the spectra using the unreasonably large and small resolutions of 5 and 1 MeV in the ϕ shape. Calling these refit values N_5 and N_1, I tabulate

$$\frac{\frac{1}{2}\,|N_5 - N_1|}{N_\phi} \;;$$

this represents half the extreme excursion in N_ϕ for these extreme resolutions, and is thus a conservative estimate of the systematic error. The errors so determined are flat in x and average to 10% in both the data and the Monte Carlo. I take 10% as my systematic error from uncertainty in the ϕ line shape.

Background

In the Monte Carlo, I establish the true background for each spectrum from the fit of the smooth background curve to the spectrum once mass pairs from the same ϕ have been removed. I then refit for N_ϕ using this fixed shape and normalization instead of allowing the background to float. Denoting this new N_ϕ by $N_{\rm fix}$, and the original measurement by $N_{\rm float}$, I find the worst-case deviation

$$\frac{|N_{\rm float} - N_{\rm fix}|}{N_{\rm fix}} \;,$$

where the worst case is selected from the two fits using reasonable detector resolutions of 2.5 and 3.5 MeV in the ϕ shape. This deviation expresses the error incurred when using the free background instead of the true background. It is flat in x and averages to 8%, which I take as my estimate of systematic error from uncertainty in the background shape. (Broadening this test to include 1 MeV and 5 MeV resolutions gives a 10% systematic error estimate.)

As a further test, I can compare N_ϕ as I fit it in the Monte Carlo to the actual number of ϕ entries present, N_{true}. This is problematical as a test of the background systematic, for statistical fluctuations and the ϕ shape uncertainty may also contribute to any deviation of N_ϕ from N_{true}. Nevertheless, this comparison shows average absolute deviations of N_ϕ from N_{true} to be 12% from this combination of systematic effects, indicating that my choice of an 8% error from background uncertainty alone is reasonable.

Two-track overlap

Since the daughter kaons of a ϕ decay tend to be close in space, especially at high x, the ability of the detector simulation to reproduce the actual two-track separation ability of the TPC is potentially important in getting the correct ϕ acceptance. Since the Monte Carlo estimates that only 10% of the ϕs are lost due to two-track overlap even at the extreme of $x = .8$, dropping sharply with lowering x, uncertainty in the accuracy of the overlap simulation is unlikely to be a problem: the Monte Carlo could be grossly in error and still not contribute significant errors. Nevertheless, I test to see that the Monte Carlo roughly reproduces the true loss of overlapping tracks.

To test the performance of the detector simulation, I prepare distributions that quantify the "closeness" of tracks. The expected acceptance loss for very close tracks is observed in these plots; comparing these distributions from the

data and Monte Carlo shows excellent agreement, even for the most sensitive case of tracks within 1° of each other in polar angle. Agreement of the plots away from the overlap region indicates that the Monte Carlo correctly reproduces the overall structure of the plot, and that the agreement in the overlap region is therefore evidence for the general correctness of the overlap simulation.

I conclude that, while there is some slight detector loss for close tracks, the Monte Carlo reproduces these losses adequately. To quantify the systematic error, I assume the detector simulation is correct to within a factor of two, and therefore I set the error equal to the predicted loss of ϕs from this effect.

Kaon identification

The systematic error from uncertainty in the particle identification acceptance I estimate by varying the momentum and dE/dx resolutions and refitting N_ϕ, in the same manner as in the ρ^0 analysis. The systematic error so determined is 8% over most of the x range (worsening as expected at high x where the dE/dx bands converge).

ϕ spin-alignment

The possibility of the ϕs having their spins preferentially aligned with some quantization axis is important for two reasons:

- knowledge of such would reveal new physics of the hadronization process, and
- such an alignment could cause the acceptance calculated from the Monte Carlo, wherein ϕs are decayed isotropically, to be in error.

I consider such an alignment along two different quantization axes: 1) the ϕ flight direction, and 2) the normal to the plane determined by the ϕ flight direction and the sphericity axis (representing the direction of flight of the initial

quarks). (Although it is not implemented in the Lund Monte Carlo program, some alignment along the latter axis, depending on p_t, is predicted in the string model.)

To test for spin alignment, I divide the mass spectra (all x combined) into five $\cos(\theta)$ bins and three p_t bins, where θ is the angle of the decay products in the ϕ rest frame relative to the quantization axis under consideration, and p_t is the transverse momentum of the ϕ with respect to the sphericity axis. I fit the number of ϕs, $N_\phi(\theta,p_t)$, in each bin as I do for my standard analysis. Dividing $N_\phi(\theta,p_t)$ as measured in the data by that as measured in the Monte Carlo provides acceptance-corrected plots showing the angular distribution of ϕs in the data. I fit these plots by a function of the form $R \cdot \left(\frac{3}{3+B}\right)(1 + B\cos^2\theta)$, where R is the relative ϕ production between data and Monte Carlo and B measures the degree of anisotropy by the amount it differs from zero. The factor of $\left(\frac{3}{3+B}\right)$ normalizes the distribution so that it integrates to R. I allow R to float in the fits, but the results for B are insensitive to whether I float R or fix it from the results of the next section.

For $p_t > 0.6$ GeV/c, $B = .19 \pm .85$ for axis (1) and $B = 0.2 \pm 1.0$ for axis (2). For all p_t combined, $B = .19 \pm .51$ for axis (1) and $B = -.09 \pm .41$ for axis (2). The other p_t bins have statistical errors so large that this exercise loses meaning. I conclude that ϕ spin alignment, if it occurs, is undetectable in this analysis, and that isotropy of the ϕ decay in the Monte Carlo introduces no systematic error.

Other sources

I deduce systematic errors from uncertainties in tracks lost from kaon decay, track-finding efficiency, nuclear interactions in material before the TPC, and determination of β in the same manner as for the ρ^0 analysis. The errors from

Source of Error	x bin				
	.10–.15	.15–.25	.25–.40	.40–.60	.60–.80
ϕ shape	10	10	10	10	10
Background	8	8	8	8	8
Two-track overlap	0	0	1	3	6
Identification efficiency	8	8	8	8	20
Kaon decay	3	1	0	0	0
Tracking efficiency	4	4	4	4	4
Branching fraction	3	3	3	3	3
Quadrature Total Systematic Error	16	16	16	16	25
Statistical Error	29	25	23	25	74

Table 6.2: Systematic and statistical errors. All figures expressed in %.

the latter two sources I find to be negligible. The former two sources have errors that are small but nonzero, and are entered into Table 6.2. I find that direct decay of the Webber cluster to good track pairs is expected to contribute negligibly to the mass spectra. The uncertainty in the 49.5% ϕ branching fraction to K^+K^- is $\pm 1.5\%$, contributing a 3% relative error to the acceptance correction.

6.4 Results

The ϕ differential cross-section measured in this study (with radiative corrections applied according to Equation 1.2) is plotted in Figure 6.5, along with the results from earlier experiments [51,52]. (The HRS measured quantities are converted to $\frac{1}{\beta\sigma_H}\frac{d\sigma}{dx}$ in the same manner as for the ρ^0 measurement.) Comparison to the Lund and Webber Monte Carlo generators is made in Figure 6.6. The χ^2 formed from my measured points and the Monte Carlo predictions is 13 for Lund and 3.9 for Webber for five degrees of freedom, indicating that Webber does much better than Lund in predicting this cross-section. The points plotted for all experiments

(including this one) indicate statistical error bars only. The horizontal bars on my measured points simply represent the extent of the x bins. The points are located in x at the average x of the bin, computed from an exponential fit to the cross-section. (The points from other experiments are plotted at the centers of their bins.)

To get the total measured ϕ multiplicity, I sum the contributions from each x bin as measured in this analysis for radiationless initial state events. This gives 0.071 ± 0.010 ϕ/event measured in $.1 < x < .8$ (taking statistical errors only). I fit an exponential to the differential cross-section as in the ρ^0 analysis; this fit has a χ^2 of 1.4 for three degrees of freedom. The Lund Monte Carlo, Webber Monte Carlo, and exponential fit predict 19%, 14%, and 11%, respectively, of all ϕs generated in events without initial state radiation to have $x < .1$ or $x > .8$. Using these figures to extrapolate the sum of individual x bin measurements to the full x range, I find 0.088 ± 0.011, 0.083 ± 0.012, and 0.080 ± 0.011 ϕ/event produced in radiationless initial state events assuming the Lund, Webber, and exponential correction, respectively. Combining all mass pairs (for all x) and then fitting with my analysis technique yields a total ϕ multiplicity of 0.081 ± 0.010.

As in the ρ^0 analysis, an alternative method to calculate the total ϕ multiplicity is to fit the measured $\frac{1}{\beta\sigma_H}\frac{d\sigma}{dx}$ by the Lund and Webber shapes and by the exponential, and then integrate the contents under the curve (taking into account the $\frac{1}{\beta}$ factor). The results of these fits for Lund, Webber, and exponential, respectively, are 0.080 ± 0.010 ($\chi^2 = 2.8$ for four d.o.f.), 0.073 ± 0.010 ($\chi^2 = 3.5$ for four d.o.f.), and 0.074 ± 0.009 ($\chi^2 = 1.4$ for three d.o.f.).

Since all these determinations of multiplicity cluster within the other errors in this analysis, I assign no additional systematic error for the multiplicity determination. The systematic error determined in the previous section is 16% in all bins except the highest, where the contribution to the multiplicity is small; it

Source	ϕ/event
TPC (this study)	$.076 \pm .016$
TPC 1984	$.077 \pm .020$
HRS	$.101 \pm .015$
Lund Generator	.112
Webber Generator	.079

Table 6.3: ϕ multiplicity in this and other experiments, and as predicted by two Monte Carlos. Errors are quadrature sums of statistical and systematic errors.

is thus fair to take an overall 16% systematic error on the ϕ multiplicity. To be consistent with the ρ^0 analysis, I average the results of the fits to $\frac{1}{\beta\sigma_H}\frac{d\sigma}{dx}$ as my quoted result; this gives $0.076 \pm 0.010(stat) \pm 0.012(syst)$ ϕ/event as my measured total ϕ multiplicity. This multiplicity is compared to the determinations of other experiments and the predictions of the Monte Carlos in Table 6.3. (All measurements and Monte Carlo predictions are for $\sqrt{s} = 29$ GeV.)

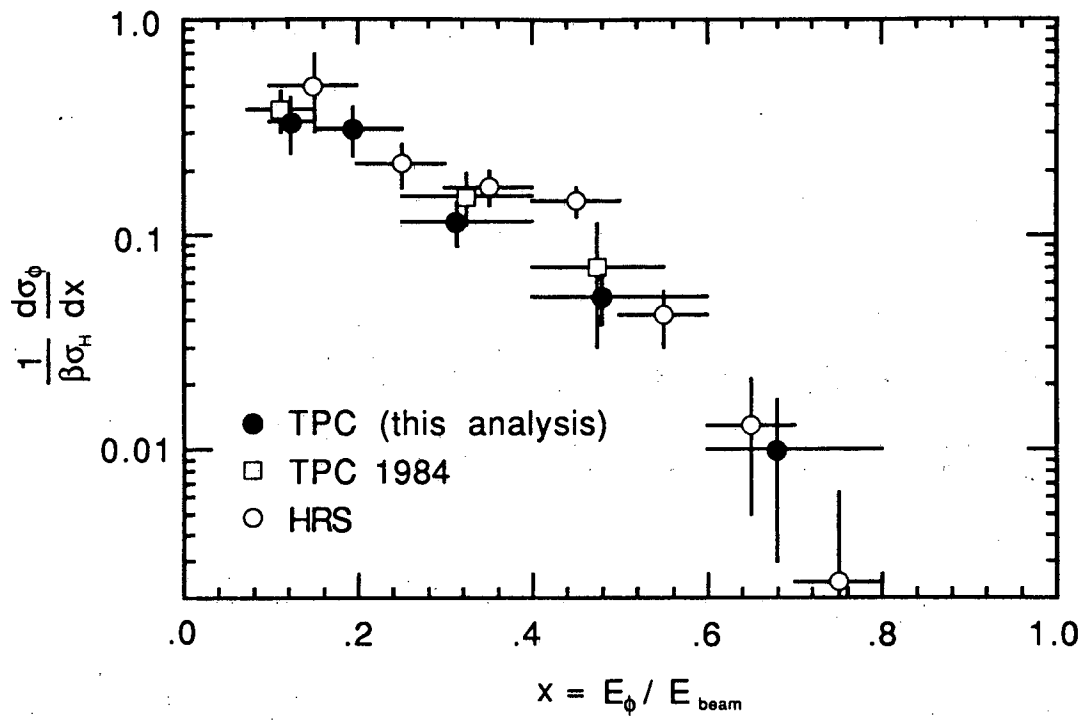

Figure 6.5: ϕ differential cross-section in this and other experiments. Errors are statistical only.

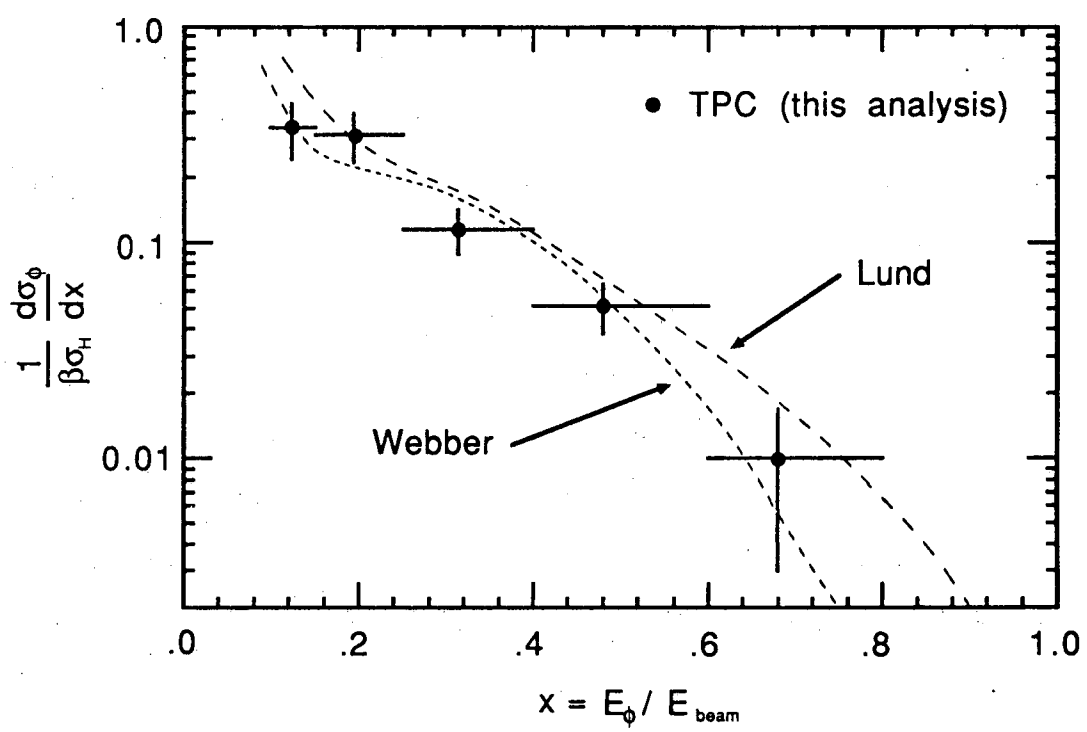

Figure 6.6: ϕ differential cross-section measured in this experiment, along with the predictions of two Monte Carlo generators. Errors are statistical only.

Chapter 7

Measurement of the K^{*0} Differential Cross-section

7.1 Overview

The K^{*0} resonance ($\Gamma = 51$ MeV, M = 897 MeV) is broad enough that the considerations relevant to this analysis are similar to those of the ρ^0, but somewhat less prone to errors. (In this thesis, "K^{*0}" and its decays are understood to stand for the charge-conjugated states as well.) The fact that it decays to $K^+\pi^-$ (67% branching fraction), the decay mode studied in this chapter, makes the combinatoric background under the K^{*0} smaller than the $\pi^+\pi^-$ background beneath the ρ^0. Along with the comparable production rate (despite the loss of observed rate from the smaller branching fraction) and the smaller intrinsic width of the K^{*0}, this reduces the statistical error of the fits relative to the ρ^0 analysis. These same facts, aided by the relative lack of structure in the $K^+\pi^-$ spectrum from resonance decays, mean also that the analysis is less prone to systematic error from uncertainty in the background shape.

As in the ρ^0 analysis, the background uncertainty will dominate the systematic error. The K^{*0} is broad enough that precise knowledge of detector resolution is relatively unimportant. There is no serious momentum-dependent gap in the acceptance, as the large Q value of the decay spreads the momenta of daughter

kaons sufficiently that the kaon acceptance loss at π/K crossover is washed-out over many x bins.

As with the ϕ analysis, my K^{*0} analysis measures the K^{*0} independently in the data and the Monte Carlo, using the Monte Carlo measurement only for the acceptance correction. Hence it suffices to use only the Lund Monte Carlo in this analysis, and unless otherwise stated, "Monte Carlo" in this chapter refers to the Lund Monte Carlo package. (I use the Webber Monte Carlo only to investigate certain systematic errors.)

I have previewed some features of the K^{*0} analysis in this section. In Section 7.2 I explain the method I've chosen for the K^{*0} analysis and present the cross-section results (with statistical errors only). In Section 7.3 I estimate systematic errors, with final results and errors described in Section 7.4.

7.2 Basic Method

In order to measure $\frac{1}{\beta\sigma_H}\frac{d\sigma}{dx}$, I divide the data and Monte Carlo mass spectra into seven x bins for $x > .075$, and measure the area in the K^{*0} peak independently in each bin. The x bins are chosen to be wide compared to the x resolution of the detector and to have reasonable numbers of K^{*0}s in each bin. The specific x bins I use are given in Table 7.1.

7.2.1 Formation of the Mass Spectra

To be used in this analysis, an event must first pass the multihadronic event selection and sphericity requirements described in Section 4.2. For a track to be used as a kaon (pion) candidate in forming the mass spectra, it must pass — apart from identity cuts — the same kaon (pion) candidate track cuts as in the ϕ (ρ^0) analysis.

I make the following choices for the particle identification cuts. I require no

minimum number of wires or pads (to maximize acceptance), accepting the slight cost in purity of the identified tracks. For a track to be used as a kaon candidate, I demand consistency with the kaon hypothesis by requiring $\chi^2_K < 9$; and I require it to have a probability (see Section 4.1.2) for being a kaon > 0.3. These are fairly loose identification criteria, designed to maximize acceptance. For a track to be used as a pion candidate, I demand consistency with the pion hypothesis by requiring $\chi^2_\pi < 9$; and I require it to have a probability for being a pion > 0.7. This cut does not overly restrict acceptance, for the pion probability is strongly peaked above 0.7 anyway; by requiring the kaon and pion probabilities to sum to one or more, I eliminate the possibility of the same pair of tracks entering the mass plots more than once. The track cuts are either identical to, or trivially inspected from, those illustrated in Figures 5.2 and 6.1. I consider the systematic error from this choice of identification criteria later.

The purity and acceptance of the kaon and pion candidates, as computed from the Monte Carlo, are plotted in Figure 7.1. The purity is the fraction of candidates of a given species that are identified correctly; the acceptance is the fraction of a given species generated in good events that are correctly identified candidates. Integrated over all momentum, the kaon (pion) purity is 66% (93%) and the kaon (pion) acceptance is 56% (65%).

In addition to comprising one kaon and one pion candidate, for a track pair to enter into the mass spectrum both tracks must lie on the same side of the event midplane as defined by the sphericity axis. This is to reduce the combinatoric background underlying the K^{*0}.

The invariant masses of track pairs surviving all the above selection passes form the spectra from which I will extract the K^{*0} signal. These spectra from the data, divided into x bins, are histogrammed in 20 MeV bins; unlike-sign combinations in Figure 7.2, like-sign in Figure 7.3. The K^{*0} peak is evident in

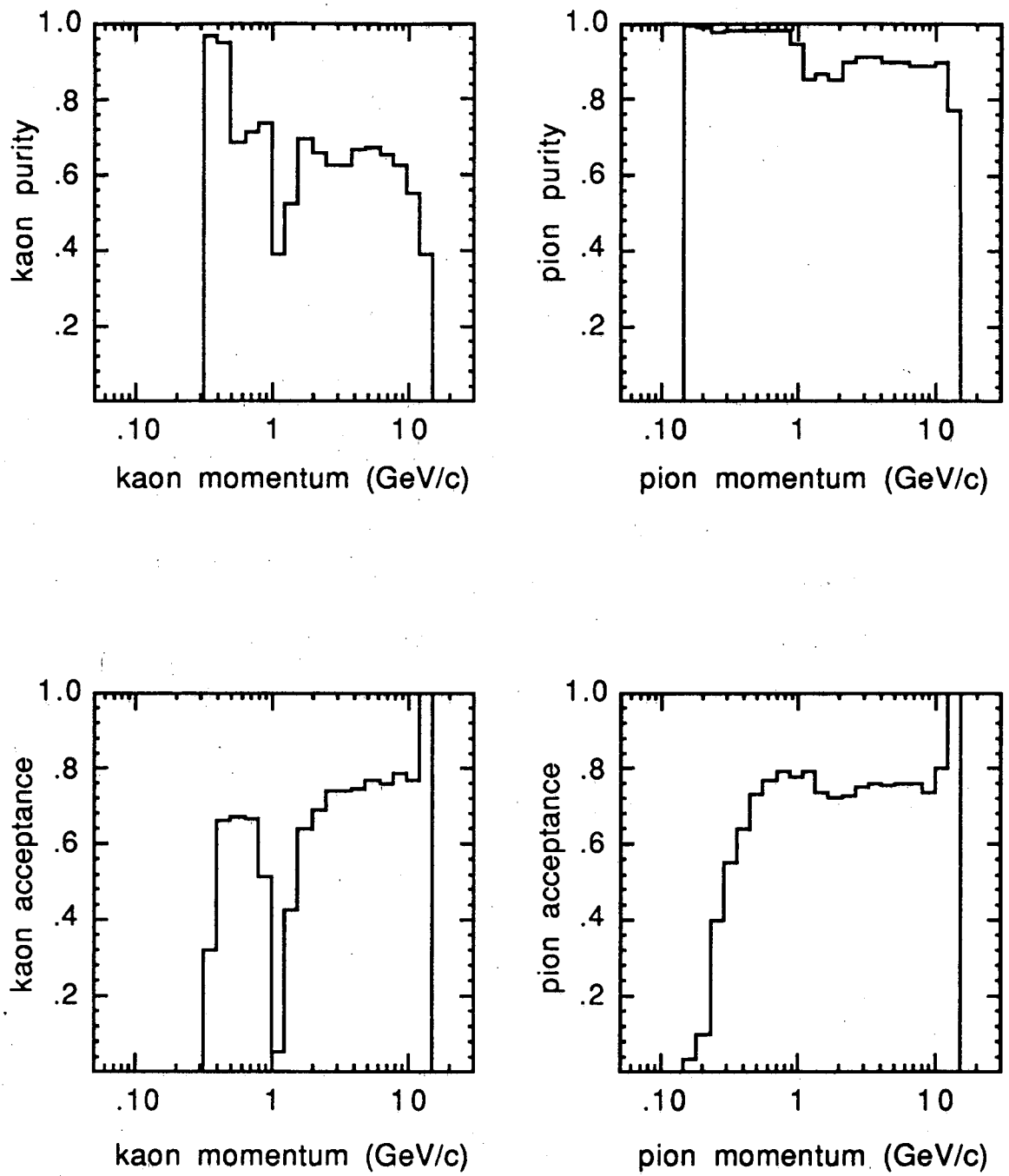

Figure 7.1: Kaon and pion purity and acceptance. The dips in purity and acceptance around 1 GeV/c are due to the K/π crossover.

the unlike-sign spectra at the correct mass and width (within statistical errors) and absent in the like-sign spectra, indicating that the feature is truly from the K^{*0}, and is not an artifact of the selection procedure.

The K^{*0} acceptance, defined as the number of K^{*0}s entering the mass plots divided by the number generated in good events (both estimated from the Monte Carlo) is plotted in Figure 7.4. Integrating over the measured x range yields an overall acceptance of 24%.

7.2.2 Extracting the Cross-section

As a preliminary observation, the Monte Carlo indicates that the unlike-sign spectra are composed almost entirely of two peaks riding atop a combinatoric background. One of these features is the K^{*0} itself. The other is from the decay $D^{*+} \rightarrow \pi^+ D^0$ (and its charge-conjugate) with the ensuing decay $D^0 \rightarrow K^- +$ anything: The π^+ is soft in the D^{*+} frame and to lesser extents in the D^0 and K^- frames, so mass combinations of it with the K^- yield masses peaking near threshold. Another relevant observation from the Monte Carlo is that the like-sign spectra are expected to closely resemble, in both shape and magnitude, the combinatoric portion of the unlike-sign spectra.

I fit the K^{*0} area independently in data and Monte Carlo by the following procedure. To extract the K^{*0} signal from the mass plots, I exploit the similarity of the like-sign spectra to the background beneath the K^{*0}. Rather than using some smooth analytic curve fit to the like-sign spectra directly as background for the unlike-sign spectra, which would make an assumption about the functional form, I take the more assumption-free step of subtracting the like-sign histograms from the unlike-sign plots in each x bin. Monte Carlo studies indicate that this procedure yields results somewhat less prone to systematic error than fitting the unlike-sign spectra directly; the cost of increased statistical errors is justified

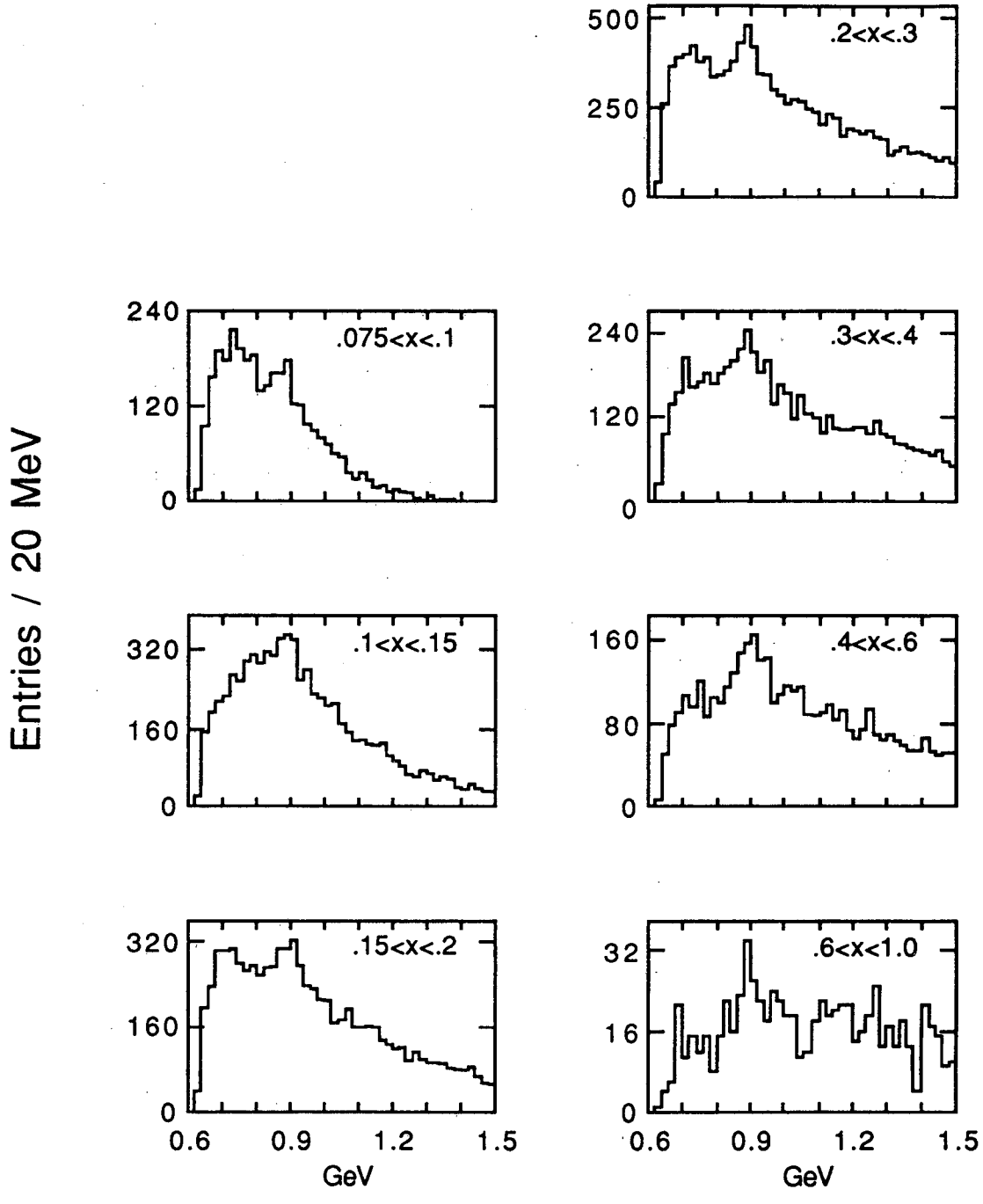

Figure 7.2: Unlike-sign Kπ mass spectra in x bins.

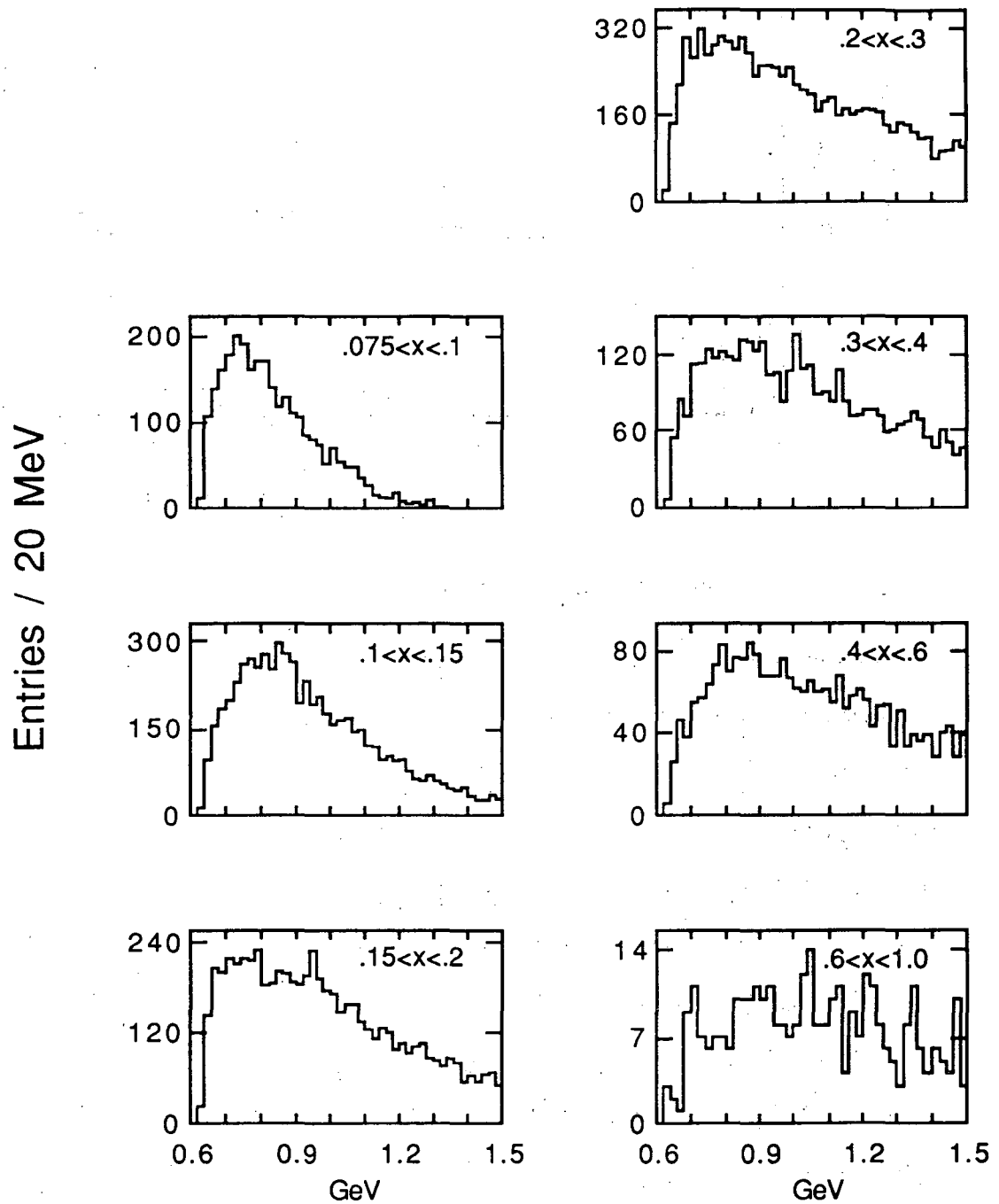

Figure 7.3: Like-sign Kπ mass spectra in x bins.

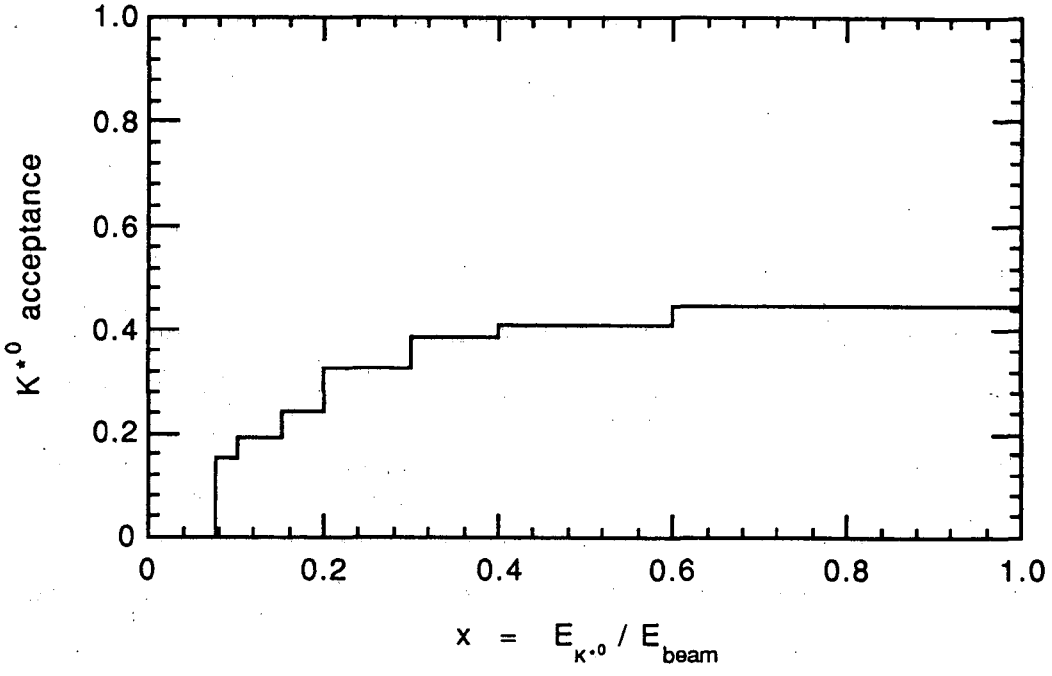

Figure 7.4: K^{*0} acceptance as a function of x.

since systematic errors will prove to dominate the multiplicity determination.

Having thus greatly reduced the combinatoric background beneath the K^{*0} by this subtraction, I account for residual background by using the analytic form of Equation 6.1; all parameters except the overall normalization are fixed in each x bin by a fit to the like-sign spectrum for that bin. The normalization is left free in the fits to the subtracted spectra. This is not necessarily the correct shape to use to estimate the background to the K^{*0} in the subtracted spectra; but aside from having a certain *a priori* appeal, it works well in the Monte Carlo, it certainly has the right limiting behavior (it vanishes) at threshold and at high mass, and it yields χ^2s of the fits as good as those of fits using different background assumptions, and hence is as reasonable as anything else. The systematic uncertainty in the cross-section from background shape is estimated in the next section.

To account for the K^{*0} contribution, I use a curve fixed in shape at the convolution of the P-wave Breit-Wigner (PWBW) of Equation 5.1 and a fixed gaussian detector resolution. Only the normalization is left free in the fit. The PWBW parameters are $\Gamma_0 = 52$ MeV and $M_0 = 898$ MeV. The detector resolution used is 10 MeV for $x < .3$ and 15 MeV for $x > .3$. These values for the resolution are not critical as long as the detector simulation closely reproduces the true resolution, for the acceptance correction cancels errors in the fit area to better than a few percent. A systematic error can enter only if the simulation fails to reproduce the true situation, a source of error I consider in the next section.

To account for the contribution from the $D^{*\pm}$ decay chain, I use the Monte Carlo prediction for both shape and magnitude. This contribution is therefore totally fixed in the fit; the systematic error from this will prove to be minor.

The two-parameter fit (background and K^{*0} normalizations) is performed as a least-squares fit to the subtracted spectra from threshold to 1.35 GeV. The upper mass cutoff is to avoid the feature from $K^{*0}(1430) \rightarrow K^+\pi^-$ decay. These fits and the subtracted spectra are plotted in Figure 7.5. The χ^2s of the fits seem only fair on the surface: they average to 43 for the data, 51 for the Lund Monte Carlo, and 62 for the Webber Monte Carlo, for the 35 d.o.f. Some of this χ^2 comes from the $D^{*\pm}$ feature region, however, where the final fit can be obviously wrong without affecting the measured K^{*0} area. (Floating the $D^{*\pm}$ area in the fit, in an effort to account for wrong branching ratios in the Monte Carlo, does not significantly improve the χ^2s.) A more meaningful measure of goodness of fit is to consider only the contribution to the χ^2 from above 800 MeV (thus avoiding the $D^{*\pm}$ contribution): here the χ^2s average 30 (data), 28 (Lund Monte Carlo), and 37 (Webber Monte Carlo) for 26 d.o.f., indicating that the fits are good in the K^{*0} region and above.

The results for $\frac{1}{\beta\sigma_H}\frac{d\sigma}{dx}$ are derived from the fit K^{*0} areas, N_{K^*}, in the standard

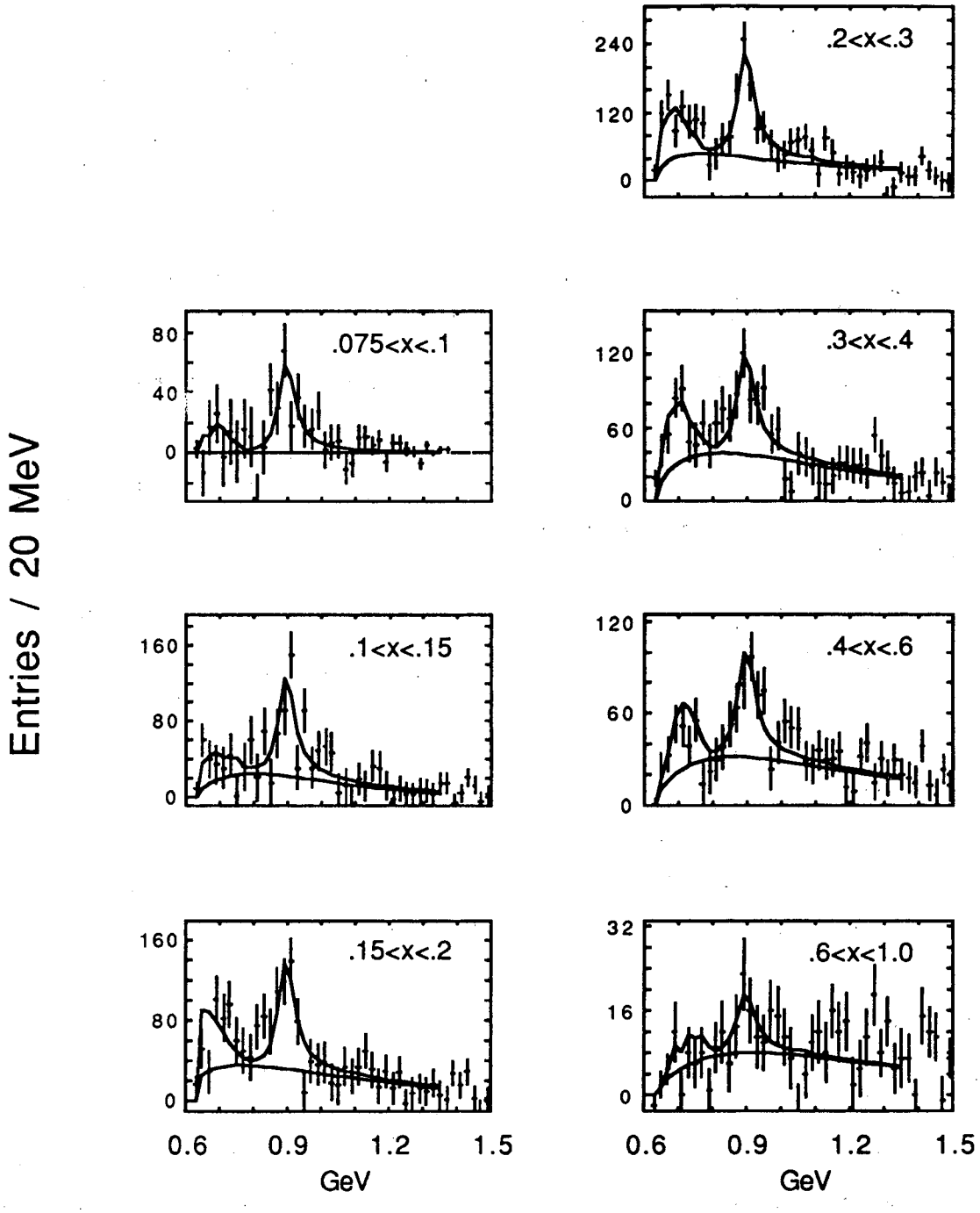

Figure 7.5: Like-sign from unlike-sign subtracted Kπ spectra in x bins, and the fits described in the text. The upper curve represents the total fit, the lower curve represents only the smooth background component.

x bin	β	N_{K^*}	$\frac{1}{\beta\sigma_H}\frac{d\sigma}{dx}$
.075< x <.10	.625	267 ± 54	6.18 ± 1.42
.10< x <.15	.820	468 ± 86	2.82 ± 0.58
.15< x <.20	.923	480 ± 78	1.87 ± 0.35
.20< x <.30	.962	825 ± 92	1.49 ± 0.21
.30< x <.40	.981	390 ± 69	0.53 ± 0.11
.40< x <.60	.992	331 ± 56	0.29 ± 0.06
.60< x <1.0	.997	54 ± 23	.026 ± .012

Table 7.1: N_{K^*} fit to the data and the derived K^{*0} differential cross-section; errors are statistical.

manner. The fit N_{K^*} and the derived cross-section are presented, with statistical errors, in Table 7.1.

7.3 Estimation of Systematic Errors

Sources of systematic error are considered below. The quantified errors are listed in Table 7.2. These errors are combined in quadrature to arrive at an overall systematic error in each bin.

Background

In order to estimate the systematic error from uncertainty in the background, I focus attention on (N_{fit}/N_{true}), the ratio of the fit number (using my nominal procedure) of K^{*0}s in a Monte Carlo spectrum to the actual number present. While a fitting method needn't necessarily have this ratio close to unity to be reliable — as long as the corresponding ratio in the data is the same, the acceptance correction cancels the potential error — it is certainly reassuring to find this ratio close to unity, and seems as reasonable a measure of the reliability of the method as any.

I average the absolute deviation from unity of this ratio (N_{fit}/N_{true}) over the seven x bins using the Lund and Webber Monte Carlos. This average is 11%

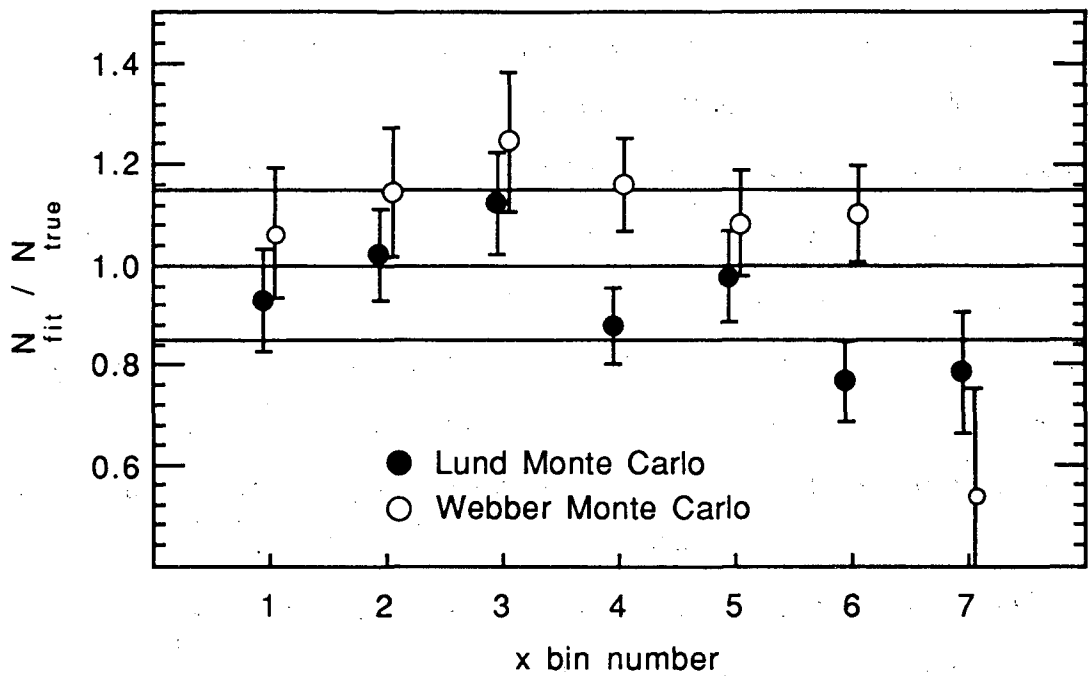

Figure 7.6: The ratios (N_{fit}/N_{true}), as described in the text. The horizontal lines indicate unity and the ±15% error band.

for Lund and 21% for Webber. The signed average deviation from unity is -7% in Lund and +1% in Webber, indicating that the procedure introduces no gross systematic shift of (N_{fit}/N_{true}). This ratio is plotted for each x bin and both Monte Carlos in Figure 7.6.

I choose to claim a 15% systematic error due to background uncertainty from this study. This is a happy medium between the Lund and Webber estimates of error (with the assumption that such errors in the data are partially correlated with those in the Monte Carlos so that I need not increase them by $\sqrt{2}$). At least it's a conservative estimate in that I'm attributing all the scatter to systematic error, while some is statistical in origin.

This method of estimating the systematic error also attributes all systematics to background uncertainty, while some could be due to using the wrong K^{*0} signal shape or $D^{*\pm}$ contribution. I show presently that these effects are expected to

be small compared to the observed errors, however, and so do not affect this estimate. As a check, I measured (N_{fit}/N_{true}) using slightly different techniques designed to eliminate the K^{*0} shape and $D^{*\pm}$ systematics, and found essentially the same background systematic error.

As a further check of this 15% background systematic, I remeasured $\frac{1}{\beta\sigma_H}\frac{d\sigma}{dx}$ using different background assumptions. These included: floating the background parameters c_2 and c_3 in the fits, using a free linear background, using a free linear background but fitting only above 800 MeV, and even the (extreme) choice of no background at all. I also tried fitting the unlike-sign (i.e. unsubtracted) spectra, taking as background both the shapes used in my nominal method, and starting at these shapes but letting all five parameters float. The ratio of these results to my nominal $\frac{1}{\beta\sigma_H}\frac{d\sigma}{dx}$ are plotted in Figure 7.7. The vast majority lie within $\pm 15\%$ of my nominal results, indicating that my results are stable against differing background assumptions to within my quoted systematic error.

K^{*0} shape

There are two leading uncertainties in the line shape of the K^{*0}. The dominant systematic is from uncertainty in the detector mass resolution, σ_m. The lesser effect is from the perturbation of the pure PWBW resonance shape, in the context of Lund string fragmentation, as explained in the case of the ρ^0.

I treat the dominant systematic first. A calculation for the case of a decay transverse (in the K^{*0} frame) to the K^{*0} flight direction indicates expected detector resolution of $\sim$8 MeV at $x \sim 0.1$, worsening to $\sim$17 MeV at $x \sim 1$. The resolutions determined from Monte Carlo studies agrees with this calculation, as does the resolution observed in the data by deconvolving the intrinsic line shape. I only get a systematic error in the cross-section if the Monte Carlo fails to re-

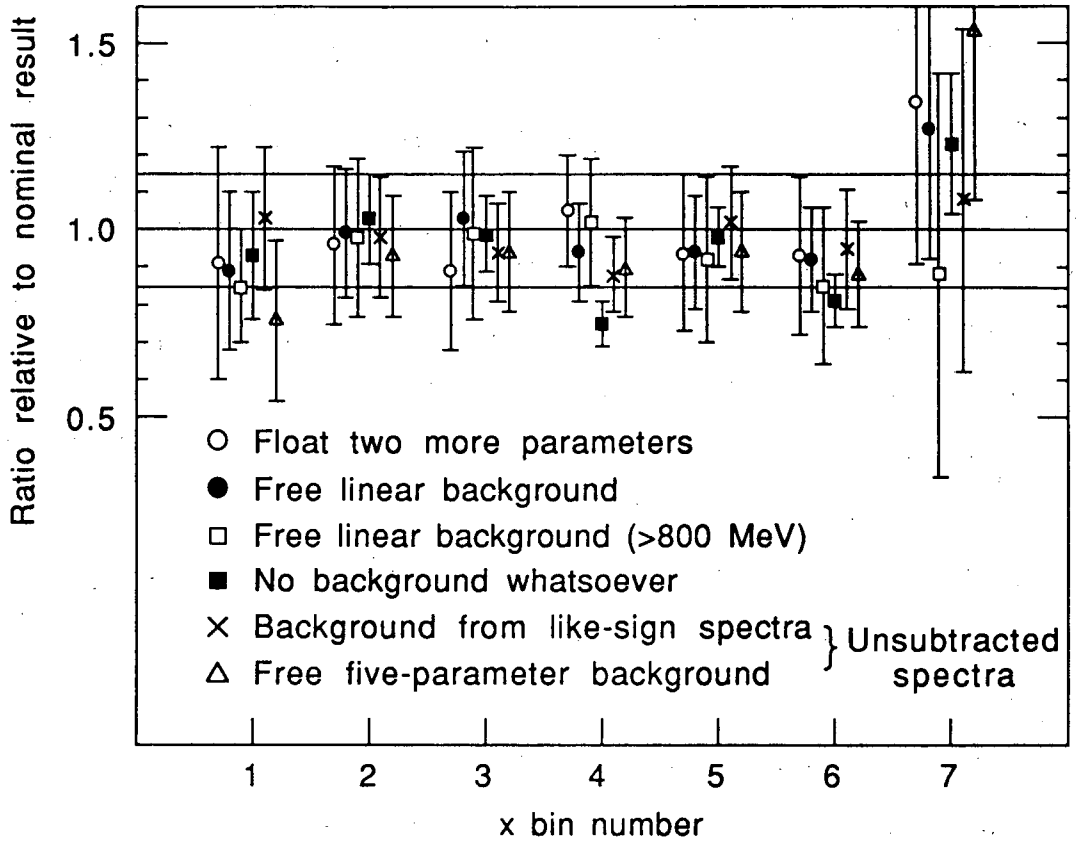

Figure 7.7: Cross-sections (normalized to nominal $\frac{1}{\beta\sigma_H}\frac{d\sigma}{dx}$) under various background assumptions. The horizontal lines indicate unity and the $\pm 15\%$ error band.

produce the resolution of the data; it would be nice to compare the resolutions directly to see how dissimilar they could be. The statistical errors, unfortunately, are too large to do this meaningfully.

To estimate this systematic, I instead consider the basic error propagation formula,

$$\sigma_m = \left[\left(\frac{\partial \mathrm{M}}{\partial \mathrm{p_K}}\right)^2 (\delta \mathrm{p_K})^2 + \left(\frac{\partial \mathrm{M}}{\partial \mathrm{p}_\pi}\right)^2 (\delta \mathrm{p}_\pi)^2 + \left(\frac{\partial \mathrm{M}}{\partial \alpha}\right)^2 (\delta\alpha)^2\right]^{\frac{1}{2}},$$

to evaluate how far off the Monte Carlo could be. Here, $\mathrm{p_K}$ and p_π are the magnitudes of the kaon and pion momenta, and α is the angle between the tracks. The potential error incurred in N_{K^*} is worst at high x, where σ_m is largest. In this regime, measurement errors in the TPC dominate $\delta\mathrm{p_K}$, $\delta\mathrm{p}_\pi$, and $\delta\alpha$, so they scale together. By examining $\delta\mathrm{p}$ for muons in $\mathrm{e^+e^-} \rightarrow \mu^+\mu^-$ events, Monte Carlo is seen to reproduce data to probably 20% of itself or better, and surely to better than 50% of itself [53]. A 50% shift in the σ_m used, from 15 MeV to 22 MeV, causes a 7% shift in N_{K^*}, which I take as my (conservative) estimate of high x error. The potential N_{K^*} error is less severe at lower x, dropping to 4% for $x < .4$.

The lesser effect of the Lund perturbation of the intrinsic line shape I treat as follows. For the worst-case bin $.6 < x < 1.0$, the Lund generator predicts a K^{*0} line shape well described by a PWBW with $\Gamma_0 = 59$ MeV (and $\mathrm{M}_0 = 898$ MeV). Fitting a PWBW generated using $\Gamma_0 = 52$ MeV by a PWBW with $\Gamma_0 = 59$ MeV shifts the fit area by less than 4%. I take this as my systematic error from uncertainty as to the presence or absence of this effect in the data. Repeating this exercise for the other bins gives a 3% error in $.4 < x < .6$, and negligible error otherwise. These errors are added in quadrature with the errors from σ_m uncertainty to arrive at the overall systematic errors from uncertainty in the K^{*0} line shape quoted in Table 7.2.

Particle identification

The systematic error from uncertainty in the particle identification acceptance I estimate in the same manner as in the ρ^0 and ϕ analyses. I find an 8% systematic error for all x.

As a further test that this analysis is insensitive to the details of particle identification, I remeasure $\frac{1}{\beta\sigma_H}\frac{d\sigma}{dx}$ using two different particle identification cuts: probability cuts for the kaon (pion) of 0.5 (0.5), and of 0.7 (0.5). These cross-sections agree with my nominal results within statistical errors.

$D^{*\pm}$ contribution

I attack the question of the systematic error incurred by uncertainty in the $D^{*\pm}$ contribution in two ways. First, I repeat the fits to the data handling the $D^{*\pm}$ feature in manners different from my nominal method: a) instead of fixing the feature area I leave it free, and b) I restrict the fit to masses > 800 MeV to eliminate the feature from consideration. The resulting fits are in all cases within statistical errors of the nominal fits; and with one exception they are all within the $\pm 15\%$ systematic error from background subtraction. (Performing the same fits (a) and (b) to the Lund spectra shifts the fit N_{K^*} negligibly. The $N_{\rm fit}/N_{\rm true}$ criterion thus fails to single out one method of accounting for the $D^{*\pm}$ feature over the others.) I do not attribute a value to this systematic error, but simply declare it to be small compared to the background systematic.

As a check, I can remeasure $\frac{1}{\beta\sigma_H}\frac{d\sigma}{dx}$ using a cut to greatly reduce the $D^{*\pm}$ feature. Since the feature arises from $D^{*+} \rightarrow \pi^+ D^0$ (and its charge-conjugate) and $D^0 \rightarrow K^- X$, with X often including a π^+, there is a low mass enhancement in the $\pi^\pm\pi^\pm$ spectrum just as there is in the $K^\mp\pi^\pm$ spectrum. Rejecting any pion that enters into a like-sign dipion mass pair lighter than 600 MeV therefore results in an 80% reduction of the $D^{*\pm}$ feature in the $K^\mp\pi^\pm$ spectra. The cross-

section measured using this cut agrees with my nominal method within statistical errors.

Other sources

I estimate systematic errors from uncertainties in particle decay reconstruction, track reconstruction efficiency, nuclear interactions, and determination of β in the same manner as for the ρ^0 and ϕ analyses. While these expected errors are small, I include them in Table 7.2 for completeness. The expected contribution to the mass plots from ρ^0 decay (entering via misidentification of one of the daughter pions) is broad, removed from the K^{*0} mass, presumably reasonably well reproduced in the Monte Carlo, and small (comparable to the fluctuations in each mass bin), so should influence the measured cross-section negligibly. The predicted spectrum (from the Webber Monte Carlo) of clusters decaying directly to accepted track pairs is likewise lost in the noise and smooth over the mass range used in this analysis, and so its presence or lack in the data should not appreciably affect the results.

7.4 Results

The K^{*0} differential cross-section measured in this study (with radiative corrections applied) is plotted in Figure 7.8, along with the results from earlier experiments [50,54]. (The HRS measured quantities are converted to $\frac{1}{\beta\sigma_H}\frac{d\sigma}{dx}$ in the same manner as for the ρ^0 and ϕ measurements.) Comparison to the Lund and Webber Monte Carlo generators is made in Figure 7.9. The χ^2 formed from my measured points and the Monte Carlo predictions is 8.2 for Lund and 21 for Webber for seven degrees of freedom, indicating that Lund does well in predicting this differential cross-section, while Webber does poorly. The points are plotted with statistical error bars only, except that the HRS results are plotted with

Source of Error	x bin .075 –.10	.10– .15	.15– .20	.20– .30	.30– .40	.40– .60	.60– 1.0
Background	15	15	15	15	15	15	15
K^{*0} shape	4	4	4	4	4	8	8
Identification efficiency	8	8	8	8	8	8	8
K/π decay	4	2	1	1	0	0	0
Tracking efficiency	4	4	4	4	4	4	4
Nuclear interactions	1	1	1	1	1	1	1
β	4	1	1	1	0	0	0
Quadrature Total Systematic Error	19	18	18	18	18	19	19
Statistical Error	23	20	19	14	20	20	45

Table 7.2: Systematic and statistical errors. All figures expressed in %.

their systematic error bars. The horizontal bars on my measured points simply represent the extent of the x bins. The points are located in x at the average x of the bin, computed from an exponential fit to the cross-section. (The points from other experiments are plotted at the centers of their bins.)

To get the total measured K^{*0} multiplicity, I sum the contributions from each x bin as measured in this analysis for radiationless initial state events. This gives 0.56 ± 0.04 K^{*0}/event measured in $x > .075$ (statistical errors only). I fit an exponential to the differential cross-section as in the ρ^0 and ϕ analyses; this fit has a χ^2 of 6.6 for five degrees of freedom. The Lund Monte Carlo, Webber Monte Carlo, and exponential fit predict 8%, 8%, and 5%, of all K^{*0}s generated in events without initial state radiation to have $x < .075$, respectively. Using these figures to extrapolate the sum of individual x bin measurements to the full x range, I find 0.61 ± 0.05, 0.61 ± 0.05, and 0.59 ± 0.05 K^{*0}/event produced in radiationless initial state events assuming the Lund, Webber, and exponential correction, respectively. Combining all mass pairs (for all x) and then fitting

Source	K^{*0}/event
TPC (this study)	$.58 \pm .12$
TPC 1984	$.49 \pm .08$
MARK II	$.62 \pm .13$
HRS	$.63 \pm .10$
Lund Generator	.58
Webber Generator	.41

Table 7.3: K^{*0} multiplicity in this and other experiments, and as predicted by two Monte Carlos. Errors are quadrature sums of statistical and systematic errors.

with my analysis technique yields a total K^{*0} multiplicity of 0.57 ± 0.04.

As in the ρ^0 and ϕ cases, an alternative method to calculate the total K^{*0} multiplicity is to fit the measured $\frac{1}{\beta\sigma_H}\frac{d\sigma}{dx}$ by the Lund and Webber shapes and by the exponential, and then integrate the contents under the curve (taking into account the $\frac{1}{\beta}$ factor). The results of these fits for Lund, Webber, and exponential, respectively, are 0.61 ± 0.05 ($\chi^2 = 7.9$ for six d.o.f.), 0.58 ± 0.05 ($\chi^2 = 7.2$ for six d.o.f.), and 0.56 ± 0.05 ($\chi^2 = 6.6$ for five d.o.f.).

Since all these determinations of multiplicity cluster well within the other errors in this analysis, I assign no additional systematic error for the multiplicity determination. The systematic error determined in the previous section is close to 19% in all bins; it is thus fair to take an overall 19% systematic error on the K^{*0} multiplicity. As for the ρ^0 and the ϕ, I average the results of the fits to $\frac{1}{\beta\sigma_H}\frac{d\sigma}{dx}$ as my quoted result; this gives $0.58 \pm 0.05(stat) \pm 0.11(syst)$ K^{*0}/event as my measured total K^{*0} multiplicity. This multiplicity is compared to the determinations of other experiments and the predictions of the Monte Carlos in Table 7.3. (All measurements and Monte Carlo predictions are for $\sqrt{s} = 29$ GeV.)

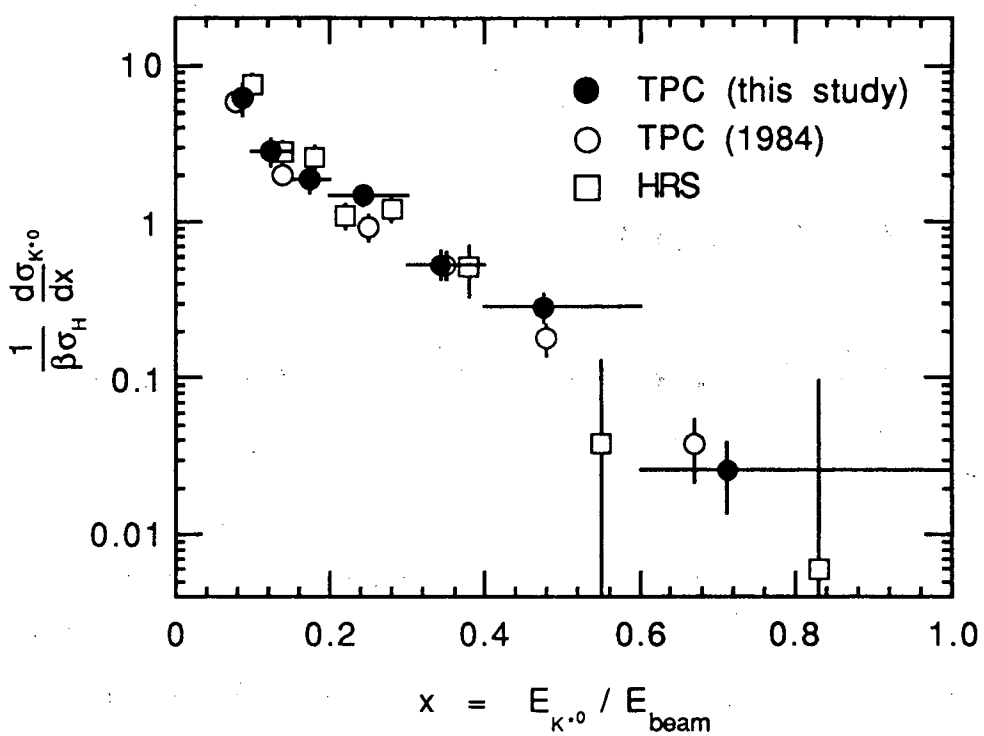

Figure 7.8: K^{*0} differential cross-section in this and other experiments. Errors are statistical only (except for HRS).

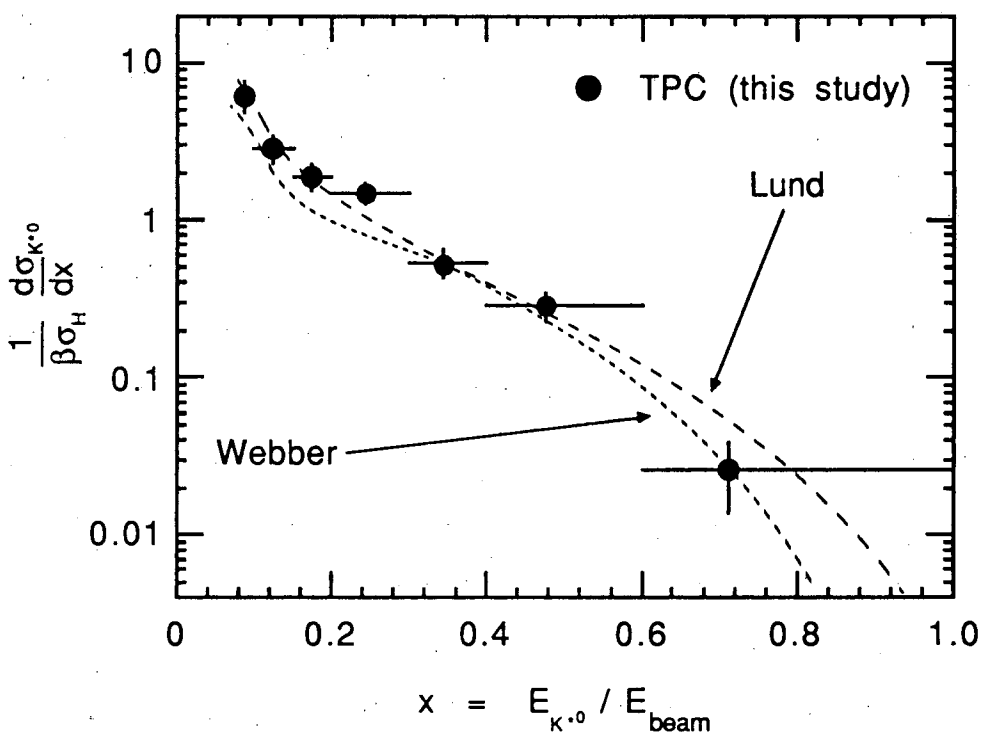

Figure 7.9: K^{*0} differential cross-section measured in this experiment, along with the predictions of two Monte Carlo generators. Errors are statistical only.

Chapter 8

Determination of s/u and V/(V+P)

The foregoing measurements of $\frac{1}{\beta\sigma_H}\frac{d\sigma}{dx}$ and overall multiplicities for the ρ^0, K^{*0}, and ϕ vector mesons stand on their own as additions to the world body of knowledge of the behavior of e^+e^- annihilation at $\sqrt{s} = 29$ GeV. In addition, they can be used to probe the underlying nature of the hadronization process; in this chapter I use them to deduce values for the strange quark to nonstrange light quark (u or d) production ratio in hadronization — the "s/u" ratio — and for the fraction of all light mesons (those containing only u, d, or s quarks) produced in fragmentation that are vector mesons — the "V/(V+P)" ratio.

The determination of s/u and V/(V+P) can be approached in model dependent and (reasonably) model independent fashions. In the model independent approach (Section 8.1), I consider only the multiplicities $N^{primary}$ stemming from the hadronization process, i.e. the measured multiplicities once contributions from decay of higher-mass states have been subtracted, and N^{frag}, which is $N^{primary}$ with contributions from leading quarks removed. Making the assumption that, apart from particles containing the QED-produced leading quarks, relative production rates of particles that differ only by the substitution of s quarks for u or d quarks depend only on a single s/u suppression factor, the three ratios $(\frac{1}{2}N^{frag}_{K^{*0}}/N^{frag}_{\rho^0})$, $(N^{frag}_{\phi}/\frac{1}{2}N^{frag}_{K^{*0}})$, and $\sqrt{N^{frag}_{\phi}/N^{frag}_{\rho^0}}$ represent two independent measurements of s/u.

(In this chapter, all multiplicities are understood to include antiparticles as well; hence the factor of $\frac{1}{2}$ accompanying $N^{frag}_{K^{*0}}$ in these ratios.) Making the assumption that relative production rates of vector and pseudoscalar mesons that have identical quark content are governed only by a single vector to pseudoscalar production ratio, the fractions $N^{primary}_{\rho^0}/(N^{primary}_{\rho^0} + N^{primary}_{\pi^0})$ and $N^{primary}_{K^{*0}}/(N^{primary}_{K^{*0}} + N^{primary}_{K^0})$ represent two independent measurements of V/(V+P). These assumptions are important (and in themselves form a sort of a toy model) and must be kept in mind when interpreting these results; but they must be made to gain any insight into the fragmentation process independent of detailed hadronization models.

For a model dependent understanding of s/u and V/(V+P) (Section 8.2), I consider the Lund Monte Carlo, which contains s/u and V/(V+P) as explicit parameters. Tuning these parameters to reproduce the measured fragmentation multiplicities at the least investigates the model's ability to self-consistently reproduce this aspect of the data. Assuming that such a tune of Lund is reasonable (i.e. yields all multiplicities satisfactorily close to those observed), the resulting s/u and V/(V+P) values will automatically include detailed effects inherent to the hadronization process: for example, threshold effects from the finite $\sqrt{s}$ available that slightly favor lighter particles beyond any intrinsic s/u or V/(V+P) ratios. Even if s/u and V/(V+P) are considered simply as parameters of the model, devoid of physical content, tuning them in the Lund context is a way of characterizing my results that allows comparison with other determinations of s/u and V/(V+P) in the Lund context.

8.1 Multiplicity Ratio Method

In general, observed particles come from three sources: decay products of higher mass particles, particles produced in the hadronization process that contain one of the original two leading quarks from the QED annihilation, and particles pro-

duced in the hadronization process that do not contain a leading quark. Breaking the total observed multiplicity N into the individual contributions from the three processes and calling them N^{decay}, $N^{leading}$, and N^{frag}, respectively, one can write

$$N = N^{decay} + N^{leading} + N^{frag}. \tag{8.1}$$

The total hadronization contribution, $N^{primary}$, is given by

$$N^{primary} = N^{leading} + N^{frag}. \tag{8.2}$$

The definition of N^{decay} involves some subtlety, in that one must carefully define just what particles one considers decay products *from*. As Hofmann [55] points out, the boundary where "hadronization" ends and "decays" begin is largely a matter of definition: does it make sense to treat a tensor particle, say, on a different footing than a piece of Lund string or a Webber QCD cluster which can have the same quark content and comparable mass? Indeed, if one accounts for decays from tensor, axial vector, and scalar mesons as well as those from pseudoscalar and vector mesons, the resulting rates of "primary" light pseudoscalars are consistent with zero [55]. Following Hofmann's lead, I will only consider decays from pseudoscalar and vector mesons (and octet and decuplet baryons, although these should contribute negligibly to the vector meson multiplicities); this is also the approach of the Lund model.

In this section, I will first estimate $N^{leading}$, then N^{decay}. With this information, I compute values for s/u and V/(V+P). I then consider systematic errors of this computation to arrive at final values and errors for s/u and V/(V+P).

Estimation of $N^{leading}$

I will estimate leading quark contributions to multiplicities, $N^{leading}$, not only for the ρ^0, K^{*0}, and ϕ; but also for the heavy pseudoscalars (D and B mesons) and heavy vector mesons (D^* and B^* mesons), as these rates will be needed for the feed-down contributions N^{decay}.

symbol	default value	meaning
f_m	0.90	Probability of a leading quark forming a meson instead of a baryon.
p_s	0.13	Probability of a non-leading quark to be strange. (Equivalent to s/u = 0.30.)
p_u	0.43	Probability of a non-leading quark to be up.
p_d	0.43	Probability of a non-leading quark to be down.
p_v	0.50	Probability of a light meson to be a vector.
p_v^h	0.75	Probability of a heavy meson (i.e. one containing charm or bottom) to be a vector.

Table 8.1: Nomenclature and default values for calculation of multiplicities from leading quarks.

I assume leading quarks are produced in the QED ratio of u : d : c : s : b = $\frac{8}{11}$: $\frac{2}{11}$: $\frac{8}{11}$: $\frac{2}{11}$: $\frac{2}{11}$. (These are the average multiplicities per event, with antiquarks included.) I further assume, as in Lund, that each leading quark will mate with a quark from the vacuum to form a meson a fraction f_m of the time, the flavor of this quark selected at random in the ratio u : d : s : c : b = $p_u : p_d : p_s : 0 : 0$. This meson will be a vector a fraction p_v of the time (p_v^h, if the leading quark is c or b); else it will be a pseudoscalar. For the ρ^0, a factor of $\frac{1}{2}$ enters from the Clebsch-Gordan decomposition of $u\bar{u}$ or $d\bar{d}$ quark pairs: these could equally well produce an ω. The notation and default numerical values are summarized in Table 8.1. The multiplicities are computed in Table 8.2.

Estimation of N^{decay} for ρ^0, K^{*0}, and ϕ

There is no baryon significantly produced at PEP that decays to ρ^0, K^{*0}, or ϕ, so in computing the decay feed-down into these three states I may restrict attention

Species (includes antiparticles)	Formula	default value
ρ^0	$\left[\frac{8}{11}p_u p_v \frac{1}{2} + \frac{2}{11}p_d p_v \frac{1}{2}\right] f_m$	.089
K^{*0}	$\left[\frac{2}{11}p_s p_v + \frac{2}{11}p_d p_v\right] f_m$	.046
ϕ	$\frac{2}{11}p_s p_v f_m$	.011
D^0	$\frac{8}{11}p_u(1-p_v^h)f_m$	.071
D^+	$\frac{8}{11}p_d(1-p_v^h)f_m$	.071
D_s^+	$\frac{8}{11}p_s(1-p_v^h)f_m$	.021
D^{*0}	$\frac{8}{11}p_u p_v^h f_m$	.213
D^{*+}	$\frac{8}{11}p_d p_v^h f_m$	.213
D_s^{*+}	$\frac{8}{11}p_s p_v^h f_m$	.064
B^0	$\frac{2}{11}p_d(1-p_v^h)f_m$	.018
B^+	$\frac{2}{11}p_u(1-p_v^h)f_m$	.018
B_s^0	$\frac{2}{11}p_s(1-p_v^h)f_m$	.005
B^{*0}	$\frac{2}{11}p_d p_v^h f_m$	.053
B^{*+}	$\frac{2}{11}p_u p_v^h f_m$	.053
B_s^{*0}	$\frac{2}{11}p_s p_v^h f_m$	.016

Table 8.2: Calculation of expected multiplicities from leading quarks.

to pseudoscalar and vector mesons. Of these, the only state not containing a charm or a bottom quark that contributes to the feed-down is the $\eta\prime$, which decays to $\rho^0\gamma$ 30% of the time. Using the measured $\eta\prime$ multiplicity [56] of $.26 \pm .09 \pm .05$, I find $.08 \pm .03$ ρ^0/event expected from $\eta\prime$ decay (taking the quoted errors in quadrature).

The remaining states to consider for contributions to $N_{\rho^0}^{decay}$, $N_{K^{*0}}^{decay}$, and N_{ϕ}^{decay} are B, D, B*, and D* mesons. Except for the D^{*+}, I assume the B* and D* mesons always decay to their pseudoscalar partners plus an irrelevant pion or photon. I assume the D^{*+} decays to D^0 50% of the time and to D^+ the rest of the time (again along with the emission of a pion or photon). With these assumptions and the leading multiplicities just calculated, I can estimate the multiplicities of D and B mesons, which constitute the remaining sources of the decay contributions to vector mesons. All I need to complete the feed-down calculation are the 18 branching fractions of the six D and B states into the three vector mesons states.

Unfortunately, these branching fractions are not well-known; uncertainty in them is a source of systematic error. I will arrive at a set of nominal branching fractions that I think are reasonable, along with estimates of upper and lower limits to these branching fractions. Using the nominal branching fractions to complete the estimation of feed-down into the ρ^0, K^{*0}, and ϕ, I will proceed to compute values for s/u and V/(V+P), employing the branching fraction limits later on to estimate the systematic error of this computation.

For the D mesons, I estimate branching fractions using experimental measurements, usually from the Particle Data Group compilations. Setting a lower limit on a given branching fraction is straightforward: I take a one sigma excursion on the low side of the sum of explicitly measured exclusive decay channels. If no such measurements exist, then the lower limit is simply zero.

Setting an upper limit for a D meson branching fraction is more problematical. Decay modes that have been measured or had upper limits set contribute in the same straightforward manner as when setting lower limits. But many potential decay modes have not been measured, except perhaps as possible contributions to observed final states (where the vector meson has not been reconstructed). In this case, one may set limits on vector mesons by assuming that final states consistent with an unreconstructed vector meson do, in fact, come from a decay chain including that meson at an intermediate stage. (The known branching fraction of the vector meson to the final observed particles must be factored into this analysis.) This procedure for setting upper limits is complicated by the fact that these limits sometimes turn out to be so conservative as to be patently ridiculous; there are also more or less arbitrary decisions of which heavy meson decay channels to consider and which to neglect. (One might neglect Cabibbo suppressed channels, say, or massive final states expected to be phase-space suppressed. Since the uncertainty in the dominant modes is typically larger than the likely contribution from the less dominant modes, it should suffice to consider only the dominant modes.) The upper limits that I select are therefore subject to some guesswork. The systematic errors from the branching fraction uncertainties turn out to be modest, however; so mistakes in setting the upper limits should not be very important. (The Particle Data Group figures I use are preliminary values for the 1988 edition of its biannual review. Because the systematic dependence on the branching fractions is moderate, my analysis should not be affected by any disparities between these figures and the ultimately published values.)

When combining explicitly measured modes and limits on unmeasured modes to arrive at an overall branching fraction upper limit, I make the conservative assumption that observed final states consistent with the presence of a vector meson always include that meson; I treat measured upper limits as one-sigma

errors on a zero measurement. All contributions can thus be treated as measurements with errors added in quadrature to arrive at a plus one-sigma excursion, which I take as the overall upper limit.

The branching fractions I choose as nominal values to assume in performing the analysis are similarly subject to some guesswork. But again, since the systematic error from this guesswork does not dominate the final errors, errors in these guesses should not be important. The branching fractions I select are at least equal to the sum of explicitly measured channels, with occasional adjustment upward to fall somewhere near the center of the range bracketed by the maximum and minimum estimates.

Decay branching fractions for the B mesons are even more difficult to estimate from measured channels than for D mesons. For B mesons, therefore, I simply take the Lund model predictions for the fractions. This model treats B decay by first weakly decaying the bottom quark, then decaying the resulting partonic configuration by the usual string decay. Since the B decay results in a reasonably high energy (several GeV) string, this algorithm should roughly reproduce the true branching fraction. Because the multiplicity of B mesons is much smaller than that of D mesons, errors in the B branching fractions should not matter much. (For this reason, I need not set upper and lower limits for the B branching fractions.)

There are two places where I depart from the straight Lund predictions for B branching fractions. First, I use the measured B^+ and B^0 (unseparated) branching fraction to $\phi + X$ [57]. Second, I override the Lund D to vector meson branching fractions with my nominal fractions in decay sequences of the B mesons.

In Table 8.3 I present the elements of the estimation of the branching fractions for D mesons: the decay channels I consider and their numerical values. I present the corresponding information for B decays in Table 8.4. Using these ingredients,

I calculate the values I use for nominal, minimum, and maximum branching fractions, presented in Table 8.5. Using the nominal fractions, I can compute the estimated feed-down contributions to the ρ^0, K^{*0}, and ϕ multiplicities from heavy mesons; I list these contributions in Table 8.6.

Nominal s/u and V/(V+P)

Since the strange quark content of mesons containing leading quarks is presumably different from those produced in the fragmentation process, one must subtract $N^{leading}$ as well as N^{decay} from observed multiplicities when computing s/u. Since there is no reason to believe the spin of a particle depends on whether it contains a leading quark, only N^{decay} needs to be subtracted from observed multiplicities when computing V/(V+P). That is, s/u must be calculated from N^{frag}; V/(V+P) may be calculated from $N^{primary}$.

The necessary subtractions from the observed ρ^0, K^{*0}, and ϕ multiplicities are performed in Table 8.7. The ratios $(\frac{1}{2}N^{frag}_{K^{*0}}/N^{frag}_{\rho^0})$, $(N^{frag}_{\phi}/\frac{1}{2}N^{frag}_{K^{*0}})$, and $\sqrt{N^{frag}_{\phi}/N^{frag}_{\rho^0}}$ that characterize the s/u ratio are 0.44 ± 0.18, 0.20 ± 0.08, and 0.30 ± 0.07, respectively, where the errors come from the total error on my measured multiplicities. All three ratios are consistent with the generally accepted value of s/u ~ 0.3.

In order to determine the V/(V+P) ratios $N^{primary}_{\rho^0}/(N^{primary}_{\rho^0} + N^{primary}_{\pi^0})$ and $N^{primary}_{K^{*0}}/(N^{primary}_{K^{*0}} + N^{primary}_{K^0})$, I need figures for $N^{primary}_{\pi^0}$ and $N^{primary}_{K^0}$. Hofmann [55] computes these to be 0.87 ± 0.45 and 0.55 ± 0.11 respectively. This calculation uses world-average measured multiplicities minus feed-down expected from pseudoscalar and vector mesons and octet and decuplet baryons; the errors include systematic as well as statistical errors. These figures yield V/(V+P) ratios of 0.40 ± 0.13 (from ρ^0 and π^0) and 0.47 ± 0.08 (from K^{*0} and K^0), where the errors combine my measured multiplicity errors and the pseudoscalar multiplicity errors. The π^0 error dominates for the ρ^0/π^0 determination; the K^{*0} error

Branching Fraction	Channel	Value (%)
$D^+ \to \rho^0 + X$	$\overline{K}^0\pi^+(\pi^+\pi^-)$	$< (15^{+7}_{-6})$
	$\overline{K}^0(\pi^+\pi^-)e^+\nu$	$< (2.2^{+5.0}_{-0.7})$
	$\overline{K}^0(\pi^+\pi^-)\mu^+\nu$	$B(D^+ \to \overline{K}^0\pi^+\pi^-e^+\nu)$
$D^+ \to \overline{K}^{*0} + X$	$\overline{K}^{*0}\pi^+$	1.7 ± 0.8
	$\overline{K}^{*0}K^+$	0.4 ± 0.2
	$(K^-\pi^+)\pi^+\pi^0$	$< \frac{3}{2}(3.8^{+1.5}_{-0.8})$
	$(\overline{K}^0\pi^0)\pi^+\pi^+\pi^-$	$< 3(4.4^{+5.2}_{-1.5})$
	$(K^-\pi^+)\pi^+\pi^0\pi^0$	$< \frac{3}{2}(2.2^{+5.0}_{-0.9})$
	$(K^-\pi^+)\pi^0e^+\nu$	$< \frac{3}{2}(4.4^{+5.2}_{-1.5})$
	$(K^-\pi^+)\pi^0\mu^+\nu$	$B(D^+ \to K^-\pi^+\pi^0e^+\nu)$
$D^+ \to \phi + X$	$\phi\pi^+$	0.7 ± 0.2
	$\overline{K}^0\pi^+(\pi^+\pi^-\pi^0)$	$< 7(4.4^{+5.2}_{-1.5})$
$D^0 \to \rho^0 + X$	$\overline{K}^0\rho^0$	$0.5^{+0.3}_{-0.2}$
	$K^-\pi^+\rho^0$	$6.7^{+1.2}_{-1.9}$
	$\overline{K}^0\pi^0\rho^0$	$B(D^0 \to K^-\pi^+\rho^0)$
	$\pi^+\pi^-(\pi^+\pi^-)$	$< (1.0^{+0.7}_{-0.3})$
	$\pi^0(\pi^+\pi^-)$	$< (1.1 \pm 0.4)$
$D^0 \to \overline{K}^{*0} + X$	$\overline{K}^{*0}\pi^0$	2.1 ± 0.6
	$\overline{K}^{*0}\rho^0$	$0.8^{+0.9}_{-0.8}$
	$\overline{K}^{*0}\pi^+\pi^-$	< 2.9
	$\overline{K}^{*0}K^0$	< 0.7
	$\overline{K}^{*0}\pi^0\pi^0$	$B(D^0 \to \overline{K}^{*0}\pi^+\pi^-)$
$D^0 \to \phi + X$	$\overline{K}^0\phi$	0.8 ± 0.2
$D_s^+ \to \rho^0 + X$	$\rho^0\pi^+$	$< (0.2)B(D_s^+ \to \phi\pi^+)$
$D_s^+ \to \overline{K}^{*0} + X$	$\overline{K}^{*0}K^+$	$(1.4 \pm 0.4)B(D_s^+ \to \phi\pi^+)$
$D_s^+ \to \phi + X$	$\phi\pi^+$	4.4 ± 1.1 [58]
	$\phi\pi^+\pi^+\pi^-$	$(1.1 \pm 0.5)B(D_s^+ \to \phi\pi^+)$ [59]

Table 8.3: Contributions to branching fractions for D mesons decaying to ρ^0, K^{*0}, and ϕ. Channels wherein the vector meson has not been explicitly reconstructed are entered with parentheses around the putative vector meson contribution; the numerical value for these channels is weighted by the inverse of the branching fraction of the vector meson to the final state particles. Unless otherwise cited, all numerical values are taken from the Particle Data Group (1988 preliminary).

Branching Fraction	Value (%)
$B^+ \to \rho^0 + X$	17
$B^+ \to \overline{K}^{*0} + X$	9
$B^+ \to \phi + X$	2.3 ± 0.8 [57]
$B^0 \to \rho^0 + X$	19
$B^0 \to \overline{K}^{*0} + X$	21
$B^0 \to \phi + X$	2.3 ± 0.8 [57]
$B_s^0 \to \rho^0 + X$	27
$B_s^0 \to \overline{K}^{*0} + X$	26
$B_s^0 \to \phi + X$	9

Table 8.4: Branching fractions for B mesons decaying to ρ^0, K^{*0}, and ϕ. Unless otherwise cited, all numerical values are taken from the Lund model prediction.

Branching Fraction	Nominal Value (%)	Lower Limit (%)	Upper Limit (%)
$D^+ \to \rho^0 + X$	8	0	29
$D^+ \to \overline{K}^{*0} + X$	25	1.3	57
$D^+ \to \phi + X$	2	0.5	67
$D^0 \to \rho^0 + X$	14	5.3	18
$D^0 \to \overline{K}^{*0} + X$	5	1.9	7
$D^0 \to \phi + X$	0.8	0.6	1.0
$D_s^+ \to \rho^0 + X$	0	0	1
$D_s^+ \to \overline{K}^{*0} + X$	6	4	9
$D_s^+ \to \phi + X$	8	6	12
$B^+ \to \rho^0 + X$	17	—	—
$B^+ \to \overline{K}^{*0} + X$	9	—	—
$B^+ \to \phi + X$	2.3	1.5	3.1
$B^0 \to \rho^0 + X$	19	—	—
$B^0 \to \overline{K}^{*0} + X$	21	—	—
$B^0 \to \phi + X$	2.3	1.5	3.1
$B_s^0 \to \rho^0 + X$	27	—	—
$B_s^0 \to \overline{K}^{*0} + X$	26	—	—
$B_s^0 \to \phi + X$	9	—	—

Table 8.5: Nominal, minimum, and maximum branching fractions used in this analysis for D and B mesons decaying into ρ^0, K^{*0}, and ϕ.

Heavy Pseudoscalar	Multiplicity	Daughter Meson	Branching Fraction	N^{decay}
D^+	0.178	ρ^0	.08	.014
		K^{*0}	.25	.045
		ϕ	.02	.004
D^0	0.391	ρ^0	.14	.055
		K^{*0}	.05	.020
		ϕ	.01	.003
D_s^+	0.085	ρ^0	.00	.000
		K^{*0}	.06	.005
		ϕ	.08	.007
B^+	0.071	ρ^0	.17	.012
		K^{*0}	.09	.006
		ϕ	.02	.002
B^0	0.071	ρ^0	.19	.013
		K^{*0}	.21	.015
		ϕ	.02	.002
B_s^0	0.021	ρ^0	.27	.006
		K^{*0}	.26	.005
		ϕ	.09	.002

Table 8.6: Estimated feed-down contributions to ρ^0, K^{*0}, and ϕ from heavy pseudoscalars. This calculation uses the nominal branching fractions listed in Table 8.5. The heavy pseudoscalar multiplicities include the effects of heavy vector meson decay, as explained in the text.

Vector Meson:	ρ^0	K^{*0}	ϕ
Measured multiplicity (this thesis)	0.77 ± 0.17	0.58 ± 0.12	0.076 ± 0.016
$N^{leading}$	0.089	0.046	0.011
N^{decay}(from B, D mesons)	0.100	0.096	0.020
N^{decay}(from η')	0.08 ± 0.03	0	0
N^{frag}	0.50 ± 0.17	0.44 ± 0.12	0.045 ± 0.016
$N^{primary}$	0.59 ± 0.17	0.48 ± 0.12	0.056 ± 0.016

Table 8.7: Estimation of N^{frag} and $N^{primary}$ for ρ^0, K^{*0}, and ϕ. The errors are the total errors on the measured multiplicity.

dominates for the K^{*0}/K^0 determination. Both ratios are consistent with the generally accepted value of V/(V+P) $\sim$ 0.4–0.5.

Systematic Errors

I consider the following sources of systematic error:

- The $D^{*+} \rightarrow D^0 + X$ branching fraction,
- p_v^h,
- f_m,
- the effect of the assumed s/u and V/(V+P) (i.e. p_u, p_d, p_s, and p_v) on N^{leading},
- the heavy pseudoscalar decay branching fractions, and
- D multiplicities.

The first four of these prove to be quite small, so I'll treat them briefly.

Varying the $D^{*+} \rightarrow D^0 + X$ branching fraction from 0.4 to 0.6 (roughly a $\pm 1\sigma$ swing) causes no more than a 4% relative shift in s/u and no more than a 2% relative shift in V/(V+P). Altering p_v^h to the extreme values of 0.5 and 1.0 produces less than a 4% (2%) relative shift in s/u (V/(V+P)). Varying f_m to the extreme values of 0.8 and 1.0 creates a 2% change in both s/u and V/(V+P). Changing f_m for heavy mesons only to 0.7 (as suggested by measurements of Λ_c [55]) also changes s/u and V/(V+P) by $\sim$ 2% of themselves. Setting s/u to 0.25 and 0.35 causes N_ϕ^{frag} (N_ϕ^{primary}) to vary from nominal by 4% (2%) of itself, with much less variation in the ρ^0 and K^{*0}; I therefore take 4% (2%) as a sensible systematic error on s/u (V/(V+P)). The only effect of changes in p_v is to change N^{frag} in a correlated fashion for ρ^0, K^{*0}, and ϕ, and not to change N^{primary} at all; so no significant systematic error in s/u or V/(V+P) results from an error in p_v.

Adding these minor systematics (all conservative) in quadrature results in a 7% error on s/u and a 4% error on V/(V+P), quite negligible compared to the ~20–40% relative errors found previously.

To estimate the systematic error from uncertainty in the heavy meson branching fractions to ρ^0, K^{*0}, and ϕ, I recompute the N^{decay} contributions using the lower and upper limits for these fractions tabulated in Table 8.5. Using all of the lower limit branching fractions (which corresponds to correlated branching fraction errors and hence is a conservative choice), N^{frag} and $N^{primary}$ increase by 0.048, 0.058, and 0.008 for the ρ^0, K^{*0}, and ϕ, respectively. Using all of the upper limit branching fractions (again a conservative choice) results in a decrease in N^{frag} and $N^{primary}$ of 0.054 and 0.067 for the ρ^0 and K^{*0}, respectively. This exercise unfortunately forces N^{frag} and $N^{primary}$ for the ϕ to be negative, an aberration that can be traced back to the absurdly high upper limit set on $B(D^+ \to \phi + X)$ from the $\overline{K}^0\pi^+(\pi^+\pi^-\pi^0)$ channel. I choose to assume the limits of $B(D^+ \to \phi + X)$ are symmetric about the nominal value in this channel; this choice gives a decrease in N_ϕ^{frag} and $N_\phi^{primary}$ of 0.008.

These systematic shifts in N^{frag} and $N^{primary}$ are roughly symmetric about the nominal values, so I take symmetric systematic errors on N^{frag} and $N^{primary}$ of 0.06, 0.07, and 0.008 for the ρ^0, K^{*0}, and ϕ, respectively. This branching fraction systematic is much larger than the other systematic errors put together, so the other systematics can be safely ignored.

Since the branching fraction systematics are largely independent for the ρ^0, K^{*0}, and ϕ and independent of the measurements, and since the measurements each have different dominant systematic errors which are independent, to an excellent approximation all systematic errors are independent and may be added in quadrature. This results in the final estimates of N^{frag} and $N^{primary}$ listed in Table 8.8, and final calculations of s/u and V/(V+P), systematic errors included,

Vector meson:	ρ^0	K^{*0}	ϕ
N^{frag}	$0.50 \pm 0.17 \pm 0.06$ $= 0.50 \pm 0.18$	$0.44 \pm 0.12 \pm 0.07$ $= 0.44 \pm 0.14$	$0.045 \pm 0.016 \pm 0.008$ $= 0.045 \pm 0.018$
$N^{primary}$	$0.59 \pm 0.17 \pm 0.06$ $= 0.59 \pm 0.18$	$0.48 \pm 0.12 \pm 0.07$ $= 0.48 \pm 0.14$	$0.056 \pm 0.016 \pm 0.008$ $= 0.056 \pm 0.018$

Table 8.8: Estimation of N^{frag} and $N^{primary}$ for ρ^0, K^{*0}, and ϕ. The first error is the total error on the measured multiplicity (statistical and systematic); the second error is the systematic error of the subtraction of N^{decay} and $N^{leading}$. These errors are added in quadrature for a total error.

Quantity	Value
s/u	0.44 ± 0.21 (from ρ^0 and K^{*0}) 0.20 ± 0.10 (from K^{*0} and ϕ) 0.30 ± 0.08 (from ρ^0 and ϕ) average: 0.30 ± 0.07
V/(V+P)	0.40 ± 0.14 (from ρ^0 and π^0) 0.47 ± 0.09 (from K^{*0} and K^0) average: 0.45 ± 0.08

Table 8.9: Calculated s/u and V/(V+P). The errors include the total error of the measured multiplicities (statistical and systematic) and the systematic error of the subtraction of N^{decay} and $N^{leading}$. The averages are weighted averages; in the case of s/u, correlations in the definitions of the individual s/u ratios are taken into account.

listed in Table 8.9. The weighted averages of these estimates of s/u and V/(V+P) represent my end results for this section, and are also entered into Table 8.9. Taking into account the correlations in the definitions of the s/u ratios, these averages are s/u $= 0.30 \pm 0.07$ and V/(V+P) $= 0.45 \pm 0.08$.

Finally, one may use the measured D^0 and D^+ multiplicities 0.45 ± 0.07 and 0.17 ± 0.03, respectively [60] instead of my calculated multiplicities. To do this, I retain the calculated feed-down from channels not involving D^0 and D^+. This includes all D_s^+ decays and the fraction of B decays coming from Lund string

fragmentation. I add to this the contribution from the measured D mesons multiplicities, using my nominal branching fractions. This calculation yields the new values $N_{\rho^0}^{decay} = 0.106$, $N_{K^{*0}}^{decay} = 0.079$, and $N_{\phi}^{decay} = 0.021$. Using these values to recompute s/u and V/(V+P) gives s/u = 0.47 (from ρ^0 and K^{*0}), s/u = 0.19 (from K^{*0} and ϕ), s/u = 0.30 (from ρ^0 and ϕ), V/(V+P) = 0.40 (from ρ^0 and π^0), and V/(V+P) = 0.48 (from K^{*0} and K^0). The shifts from the calculated values in Table 8.9 are small compared to the errors, so using measured D multiplicities in lieu of the predicted multiplicities makes no significant difference.

8.2 Lund-specific Method

As explained earlier, I can attempt to tune the Lund s/u and V/(V+P) parameters to achieve agreement of the Lund model predictions with my measurements. I use Lund v5.3 for this study. (Lund v5.3 allows the V/(V+P) ratio for strange mesons to be different from V/(V+P) for nonstrange light mesons; I set these to be equal so there is one overall V/(V+P) ratio for light mesons.)

I tune these parameters by minimizing a χ^2 formed from Lund model predictions and experimental measurements. One is therefore faced with a choice of just what quantities to include in forming this χ^2. The simplest χ^2 one could form from my measurements would include the ρ^0, K^{*0}, and ϕ multiplicities before feed-down, i.e. $N^{primary}$. One would then tune s/u and V/(V+P) to reproduce these rates. This could result in a contrived and useless configuration of the Lund parameters, however, if other predictions of the model fell into poor agreement with the data in the process of adjusting s/u and V/(V+P). In particular, adjusting s/u and V/(V+P) is certain to change the total and strange multiplicity predictions of the model, multiplicities which are well-measured in the form of charged pion and charged kaon multiplicities. To keep my tuning procedure from going too far afield in these well-measured quantities, I include

them in the χ^2 and allow the parameter a in the LSFF (Equation 2.5) to vary to help compensate for multiplicity changes when adjusting s/u and V/(V+P). Apart from a, s/u, and V/(V+P), all parameters are kept at the values used throughout this thesis, described in Section 2.3.2.

Thus, the χ^2 I choose to minimize is

$$\chi^2 = \left(\frac{N_{\rho^0}^{primary} - N_{\rho^0}^{Lund}}{\delta N_{\rho^0}^{primary}}\right)^2 + \left(\frac{N_{K^{*0}}^{primary} - N_{K^{*0}}^{Lund}}{\delta N_{K^{*0}}^{primary}}\right)^2 + \left(\frac{N_{\phi}^{primary} - N_{\phi}^{Lund}}{\delta N_{\phi}^{primary}}\right)^2 + \left(\frac{N_{\pi^+}^{total} - N_{\pi^+}^{Lund}}{\delta N_{\pi^+}^{total}}\right)^2 + \left(\frac{N_{K^+}^{total} - N_{K^+}^{Lund}}{\delta N_{K^+}^{total}}\right)^2 \tag{8.3}$$

where the indicated particles are understood to include antiparticles. The $N^{primary}$ and their errors $\delta N^{primary}$ for ρ^0, K^{*0}, and ϕ are taken from Table 8.8. The statistical errors of the Lund predictions are negligibly small, so no additional error is taken in $\delta N^{primary}$. For the pion and kaon charged multiplicities $N_{\pi^+}^{total}$ and $N_{K^+}^{total}$, I take the world-average values 10.3 ± 0.4 and 1.48 ± 0.09, respectively [55]. No error in addition to those just quoted are taken in $\delta N_{\pi^+}^{total}$ and $\delta N_{K^+}^{total}$. The quantities superscripted "Lund" are the Lund model predictions for the corresponding measured quantity. I vary three Lund parameters — a, s/u, and V/(V+P) — so there are two degrees of freedom in this fit to five measured quantities.

To minimize this χ^2, I generate 10,000 hadronic events (without initial state radiation) at each point of a lattice in the three-dimensional parameter space. The lattice sites are at all 45 combinations of a = 0.855, 0.955, and 1.055, s/u = 0.25, 0.30, and 0.35, and V/(V+P) = 0.40, 0.45, 0.50, 0.55, and 0.60. At each lattice site, tabulating the various multiplicities in the 10,000 events gives the Lund predictions from which I form the χ^2. I assume this χ^2 is sufficiently near minimum to be described by a three-dimensional parabola centered on the minimum. Assuming equal errors on the χ^2 at each lattice site, I fit a three-

dimensional parabola of the form

$$A(a-a_{min})^2 + B(s-s_{min})^2 + C(V-V_{min})^2$$

$$+D(a-a_{min})(s-s_{min}) + E(a-a_{min})(V-V_{min}) + F(s-s_{min})(V-V_{min})$$

$$+\chi^2_{min} \tag{8.4}$$

to this χ^2, where s is short for s/u and V is short for V/(V+P). The ten free parameters of this fit are A, B, C, D, E, F, a_{min}, s_{min}, V_{min}, and χ^2_{min}. The values a_{min}, s_{min}, and V_{min} represent the best tune of a, s/u, and V/(V+P); mapping out the $(\chi^2 - \chi^2_{min}) = 1$ locus in three dimensions yields the $\pm 1\sigma$ bounds on these parameters including correlations. Systematic errors are also included in these $\pm 1\sigma$ bounds, as systematic errors are included in the χ^2. I present these tuned parameters and their errors in Table 8.10. The tuned values for s/u and V/(V+P) are consistent with the generally accepted values s/u $\sim$ 0.3 and V/(V+P) $\sim$ 0.4–0.5. At minimum, $\chi^2 = 0.7$ for two degrees of freedom, indicating that the Lund model is capable of simultaneously reproducing all five experimental quantities that entered into the χ^2.

The errors quoted on the tuned values for a, s/u, and V/(V+P) are only sensible if the three-dimensional parabola is a good fit to the actual χ^2s at the lattice sites. The RMS deviation of the parabola from the actual values is 0.36 taken over all 45 lattice sites. Interpreted as the order of the χ^2 fitting error, perhaps I've found the $\Delta\chi^2 = 1.36$ or $\Delta\chi^2 = 0.64$ locus instead of the $\Delta\chi^2 = 1.0$ locus. This would mean my 1σ errors are wrong by $\sim$ 20% of themselves, a modest discrepancy. (In point of fact, the agreement between the three-dimensional parabola and the actual lattice values is better than an RMS deviation of 0.36 in the vicinity of the $\Delta\chi^2 = 1.0$ locus.) The parabolic fit is therefore sufficiently good to trust the errors I quote.

Lund parameter	tuned value
a	1.01 ± 0.29
s/u	0.30 ± 0.03
V/(V+P)	0.45 ± 0.11

Table 8.10: Result of tuning the Lund parameters a, s/u, and V/(V+P) to fit $N_{\rho^0}^{primary}$, $N_{K^{*0}}^{primary}$, $N_{\phi}^{primary}$, and charged pion and kaon multiplicities. The errors include correlations and systematic errors.

Chapter 9

Summary and Conclusions

In this thesis I have measured radiatively corrected differential cross-sections in $x = E_{meson}/E_{beam}$ for the vector mesons ρ^0, K^{*0}, and ϕ. The results of these measurements are plotted, along with previous measurements and the predictions of the Lund and Webber Monte Carlos, in Figures 5.7, 5.8, 7.8, 7.9, 6.5, and 6.6. Integrating the cross-sections and extrapolating to unmeasured x regions yields the particle multiplicities in Table 9.1. The agreement with the Lund and Webber Monte Carlos is quantified in terms of χ^2s both for the differential cross-sections and for the total multiplicities in Table 9.2.

Using these measured multiplicities, plus estimations of the leading quark and feed-down contribution to them, I computed the s/u and V/(V+P) ratios presented in Table 9.3. In the specific context of the Lund Monte Carlo, I tuned the s/u and V/(V+P) (and a) parameters of the model to minimize a χ^2 formed using these multiplicities. I list the results of this Lund-specific tune in Table 9.4.

These measurements in themselves do not clearly favor nor disfavor either the Lund or Webber Monte Carlos. The differential cross-sections, multiplicities, and s/u and V/(V+P) ratios measured in this thesis are consistent with previous measurements. While the results of this work provide no dramatic breakthroughs nor definitive tests of models, it is my hope that their contribution to the world body of knowledge brings us closer to finding an ultimate theory of hadronization.

meson	measured multiplicity
ρ^0	$0.77 \pm 0.08(stat) \pm 0.15(syst)$
K^{*0}	$0.58 \pm 0.05(stat) \pm 0.11(syst)$
ϕ	$0.076 \pm 0.010(stat) \pm 0.012(syst)$

Table 9.1: Vector meson multiplicities measured in this thesis. These results are extrapolated from measured x regions to cover all allowed x and are corrected for initial state radiation.

meson	$\frac{1}{\beta\sigma_H}\frac{d\sigma}{dx}$			multiplicity	
	Lund	Webber	d.o.f.	Lund	Webber
ρ^0	8.2	7.6	6	0.2	0.8
K^{*0}	8.2	21	7	0.0	2.0
ϕ	13	3.9	5	5.1	0.0

Table 9.2: Agreement of predictions of the Lund and Webber Monte Carlos with measured differential cross-sections and multiplicities, expressed as χ^2s. The degrees of freedom (d.o.f.), which are simply the number of x-bins, are indicated for the differential cross-sections; the d.o.f. is one for multiplicities. The specifics of the Lund and Webber Monte Carlos used for these comparisons are detailed in Section 2.3.

s/u	0.44 ± 0.21 (using ρ^0 and K^{*0}) 0.20 ± 0.10 (using K^{*0} and ϕ) 0.30 ± 0.08 (using ρ^0 and ϕ) average: 0.30 ± 0.07
V/(V+P)	0.40 ± 0.14 (using ρ^0 and π^0) 0.47 ± 0.09 (using K^{*0} and K^0) average: 0.45 ± 0.08

Table 9.3: The s/u and V/(V+P) ratios determined in Chapter 8. Errors are combined statistical and systematic errors.

s/u	0.30 ± 0.03
V/(V+P)	0.45 ± 0.11
a	1.01 ± 0.29

Table 9.4: The s/u, V/(V+P), and a parameters of Lund determined by the tuning procedure described in Chapter 8. The errors are combined statistical and systematic, and include correlations among the parameters.

Bibliography

[1] G. Altarelli and G. Parisi. *Nucl. Phys.* **B126**, 298 (1977).

[2] M. Bengtsson and T. Sjöstrand. *Nucl. Phys.* **B289**, 810 (1987).

[3] B. R. Webber. *Nucl. Phys.* **B238**, 492 (1984).

[4] R. D. Field and R. P. Feynman. *Nucl. Phys.* **B136**, 1 (1978).

[5] P. Hoyer, et al. *Nucl. Phys.* **B161**, 349 (1979).

[6] A. Ali, et al. *Phys. Lett.* **93B**, 155 (1980).

[7] T. Meyer. *Z. Phys.* **C12**, 77 (1982).

[8] J. Schwinger. *Phys. Rev.* **128**, 2425 (1962).

[9] J. Kogut and L. Susskind. *Phys. Rev.* **D9**, 3501 (1974).

[10] E. Eichten, et al. *Phys. Rev.* **D17**, 3090 (1978).

[11] D. H. Perkins. *Introduction to High Energy Physics*, pages 175–177. Addison-Wesley, 2nd (rev.) edition, 1982.

[12] B. Andersson, et al. *Nucl. Phys* **B135**, 273 (1978).

[13] B. Andersson and G. Gustafson. *Z. Phys.* **C3**, 223 (1980).

[14] B. Andersson, et al. *Phys. Rep.* **97**, 31 (1983).

[15] B. Andersson, et al. *Z. Phys.* **C20**, 317 (1983).

[16] J. W. Gary. *Tests of Models for Parton Fragmentation in e^+e^- Annihilation.* PhD thesis, University of California, Berkeley, November 1985. LBL-20638.

[17] D. Amati and G. Veneziano. *Phys. Lett.* **83B**, 87 (1979).

[18] S. Wolfram. Parton and hadron production in e^+e^- annihilation. In J. Tran Thanh Van, editor, *Proc. 15th Rencontre de Moriond*, page 549, 1980.

[19] C. D. Buchanan and S. B. Chun. *Phys. Rev. Lett.* **59**, 1997 (1987).

[20] H. Yamamoto. *Hadron Production at PEP/PETRA.* LBL Report LBL-20749, Lawrence Berkeley Laboratory, December 1985.

[21] G. D. Cowan. *Inclusive $\pi^\pm$, $K^\pm$, and p, $\overline{p}$ Production in e^+e^- Annihilation at $\sqrt{s}$ = 29 GeV.* PhD thesis, University of California, Berkeley, January 1988. LBL-24715.

[22] W. Bartel, et al. *Z. Phys.* **C21**, 37 (1983).

[23] H. Aihara, et al. *Phys. Rev. Lett.* **54**, 270 (1985).

[24] M. Derrick, et al. *Inclusive Charged Particle Production Near the Kinematic Limit in e^+e^- Annihilation at 29 GeV.* ANL-HEP-PR-85-77, Argonne National Laboratory, 1985.

[25] H. Aihara, et al. *Phys. Rev. Lett.* **55**, 1047 (1985).

[26] T. Takahashi. *Study of Higher Order QCD Effects in e^+e^- Hadronic Annihilations.* PhD thesis, University of Tokyo, December 1986. UT-HE-87/2.

[27] A. Petersen, et al. *Phys. Rev. Lett.* **55**, 1954 (1985).

[28] H. Aihara, et al. *Charged Hadron Production in e^+e^- Annihilation at $\sqrt{s}$ = 29 GeV.* LBL Report LBL-23737, Lawrence Berkeley Laboratory, March 1988.

[29] W. Gorn, et al. *IEEE Trans. Nucl. Sci.* **NS-26**, 68 (1979).

[30] W. Gorn, et al. *IEEE Trans. Nucl. Sci.* **NS-30**, 153 (1983).

[31] H. Aihara, et al. *IEEE Trans. Nucl. Sci.* **NS-30**, 117 (1983).

[32] H. Aihara, et al. *Nucl. Instr. Meth.* **217**, 259 (1983).

[33] W. W. Moses. *Measurement of the Inclusive Branching Fraction $\tau^- \rightarrow \nu_\tau \pi^- \pi^0$ + neutral meson(s).* PhD thesis, University of California, Berkeley, December 1986. LBL-22579.

[34] H. Aihara, et al. *IEEE Trans. Nucl. Sci.* **NS-30**, 67 (1983).

[35] R. I. Koda. *A Test of Quantum Electrodynamics at Small Angles Using the PEP-4 Facility.* PhD thesis, University of California, Los Angeles, 1985. UCLA-85-011.

[36] H. Aihara, et al. *IEEE Trans. Nucl. Sci.* **NS-30**, 63, 76, 162 (1983).

[37] H. Aihara, et al. *Nucl. Instr. Meth.* **223**, 40 (1984).

[38] T. K. Edberg. *A Neophyte's Guide to Track Fitting in the TPC.* TPC Note TPC-LBL-87-16, Lawrence Berkeley Laboratory, Feb 1987.

[39] R. L. Gluckstern. *Nucl. Instr. Meth.* **24**, 381 (1963).

[40] M. T. Ronan. *The PEP-4 (TPC) Trigger System.* TPC Note TPC-LBL-87-12, Lawrence Berkeley Laboratory, May 1987.

[41] L. G. Mathis. *A Search for New Leptons with Heavy Neutrinos in e^+e^- Annihilation at $\sqrt{s}$ = 29 GeV.* PhD thesis, University of California, Berkeley, May 1988. LBL-25261.

[42] H. S. Kaye. *PEP4 Offline Processing of Experiments 14–18.* TPC Note TPC-LBL-87-1, Lawrence Berkeley Laboratory, Jan 1987.

[43] K. A. Derby. *Integrated Luminosity for Experiments 14–18.* TPC Note TPC-LBL-87-17, Lawrence Berkeley Laboratory, May 1987.

[44] F. A. Berends and R. Kleiss. *Nucl. Phys.* **B178**, 141 (1981).

[45] J. D. Jackson. *Nuovo Cimento* **34**, 6692 (1964).

[46] Werner Hofmann, private communication.

[47] R. Brandelik, et al. *Phys. Lett.* **117B**, 135 (1982).

[48] W. Bartel, et al. *Phys. Lett.* **145B**, 441 (1984).

[49] H. M. Schellman. *Inclusive Production of Strange and Vector Mesons in e^+e^- Annihilation at 29 GeV.* PhD thesis, University of California, Berkeley, November 1984. LBL-18699.

[50] M. Derrick, et al. *Phys. Lett.* **158B**, 519 (1985).

[51] M. Derrick, et al. *Phys. Rev. Lett.* **54**, 2568 (1985).

[52] H. Aihara, et al. *Phys. Rev. Lett.* **52**, 2201 (1984).

[53] Gerry Lynch, private communication.

[54] H. Aihara, et al. *Phys. Rev. Lett.* **53**, 2378 (1984).

[55] W. Hofmann. *Particle Composition in Hadronic Jets in e^+e^- Annihilation.* LBL Report LBL-24897, Lawrence Berkeley Laboratory, March 1988. Submitted to *Annual Review of Nuclear and Particle Sciences.*

[56] G. Wormser, et al. *η and $\eta\prime$ Production in e^+e^- Annihilation at 29 GeV: Indications for the $D_s^\pm$ Decays Into $\eta\pi^\pm$ and $\eta\prime\pi^\pm$.* SLAC-PUB-4554, Stanford Linear Accelerator Center, March 1988. Submitted to *Phys. Rev. Lett.*

[57] D. Bortoletto, et al. *Phys. Rev. Lett.* **56**, 800 (1986).

[58] A. Chen, et al. *Phys. Lett. Lett.* **51**, 634 (1983).

[59] H. Albrecht, et al. *Phys. Lett.* **153B**, 343 (1985).

[60] P. Baringer, et al. *Production Cross Section and Electroweak Asymmetry Of D^* and D Mesons Produced in in e^+e^- Annihilation at 29 GeV.* ANL-HEP-PR-88-3, Argonne National Laboratory, 1988. Submitted to *Phys. Lett.*

LAWRENCE BERKELEY LABORATORY
TECHNICAL INFORMATION DEPARTMENT
UNIVERSITY OF CALIFORNIA
BERKELEY, CALIFORNIA 94720